

High-order accurate structure-preserving finite volume schemes on adaptive moving meshes for shallow water equations: well-balancedness and positivity

Zhihao Zhang^a, Huazhong Tang^{b,a}, Kailiang Wu^{c,d,*}

^a*Center for Applied Physics and Technology, HEDPS and LMAM, School of Mathematical Sciences, Peking University, Beijing, 100871, P.R. China*

^b*Nanchang Hangkong University, Nanchang, 330000, Jiangxi Province, P.R. China*

^c*Department of Mathematics & Shenzhen International Center for Mathematics, Southern University of Science and Technology, Shenzhen, Guangdong, 518055, P.R. China*

^d*Guangdong Provincial Key Laboratory of Computational Science and Material Design, Shenzhen 518055, China*

Abstract

This paper develops high-order accurate, well-balanced (WB), and positivity-preserving (PP) finite volume schemes for shallow water equations on adaptive moving structured meshes. The mesh movement poses new challenges in maintaining the WB property, which not only depends on the balance between flux gradients and source terms but is also affected by the mesh movement. To address these complexities, the WB property in curvilinear coordinates is decomposed into flux source balance and mesh movement balance. The flux source balance is achieved by suitable decomposition of the source terms, the numerical fluxes based on hydrostatic reconstruction, and appropriate discretization of the geometric conservation laws (GCLs). Concurrently, the mesh movement balance is maintained by integrating additional schemes to update the bottom topography during mesh adjustments. The proposed schemes are rigorously proven to maintain the WB property by using the discrete GCLs and these two balances. We provide rigorous analyses of the PP property under a sufficient condition enforced by a PP limiter. Due to the involvement of mesh metrics and movement, the analyses are nontrivial, while some standard techniques, such as splitting high-order schemes into convex combinations of formally first-order PP schemes, are not directly applicable. Various numerical examples validate the high-order accuracy, high efficiency, WB, and PP properties of the proposed schemes.

Keywords: Shallow water equations; adaptive moving structured mesh; finite volume; well-balanced; positivity-preserving

*Corresponding author.

e-mail: zhihaozhang@pku.edu.cn (Zhihao Zhang), hztang@math.pku.edu.cn (Huazhong Tang), wukl@sustech.edu.cn (Kailiang Wu)

1. Introduction

Shallow water equations (SWEs) describe the behavior of a shallow layer of flowing water influenced by gravity and bottom topology. They are widely applied in research related to atmospheric, river, and coastal dynamics, as well as in studies of phenomena such as tsunamis. The two-dimensional (2D) SWEs are defined within a time-space physical domain $(t, \mathbf{x}) \in \mathbb{R}^+ \times \Omega_p$, where $\Omega_p \subset \mathbb{R}^2$ and $\mathbf{x} = (x_1, x_2)$. With non-flat, time-independent bottom topography $b(\mathbf{x})$, the 2D SWEs can be expressed as the following hyperbolic balance laws

$$\begin{cases} \frac{\partial h}{\partial t} + \frac{\partial(hv_1)}{\partial x_1} + \frac{\partial(hv_2)}{\partial x_2} = 0, \\ \frac{\partial(hv_1)}{\partial t} + \frac{\partial(hv_1^2 + \frac{1}{2}gh^2)}{\partial x_1} + \frac{\partial(hv_1v_2)}{\partial x_2} = -gh \frac{\partial b}{\partial x_1}, \\ \frac{\partial(hv_2)}{\partial t} + \frac{\partial(hv_1v_2)}{\partial x_1} + \frac{\partial(hv_2^2 + \frac{1}{2}gh^2)}{\partial x_2} = -gh \frac{\partial b}{\partial x_2}, \end{cases} \quad (1)$$

where $h(t, \mathbf{x}) \geq 0$ represents the water depth, $v_\ell(t, \mathbf{x})$ denotes the x_ℓ -component of the fluid velocity for $\ell = 1, 2$, and g is the gravitational constant. Numerical simulation plays a crucial role in the applications of SWEs and has been extensively studied in the literature; see, for example, [1, 2, 22, 25, 33, 34, 49] and the references therein.

Due to the presence of the source terms, the SWEs (1) admit nontrivial steady states, where these source terms balance the flux gradients, e.g., the lake at rest solution

$$h + b = C, \quad v_1 = v_2 = 0. \quad (2)$$

Many physical phenomena, such as waves on a lake or tsunamis in the deep ocean, can be viewed as small perturbations of these steady states. Consequently, capturing these small perturbations in numerical simulations is very important. This need has led to the development of well-balanced (WB) schemes, which are designed to preserve steady states discretely, thus facilitating the capture of perturbations even on coarse meshes. Standard numerical methods often lack WB properties, necessitating the use of fine meshes to accurately capture perturbations, which can result in prohibitively high computational costs. The WB or the ‘‘C-property’’ was initially demonstrated in [2]. Since then, various types of WB numerical methods for the SWEs have been explored, including finite difference methods [18, 28, 34], finite volume methods [1, 17, 21, 22], and discontinuous Galerkin (DG) methods [32, 37, 41]. The readers are referred to the review article [14] and the references therein.

Another challenge in the numerical solution of the SWEs is to preserve the non-negativity of the water depth. In fact, negative water depths can destroy the essential hyperbolicity of the equations, leading to serious numerical issues due to numerical ill-posedness, such as non-physical solutions, instability, or simulation crashes. Over the past few decades, there has been

considerable interest in developing high-order positivity-preserving (PP) or bound-preserving schemes [31]. A general approach was proposed in [44, 45] for finite volume and DG schemes for scalar conservation laws and compressible Euler equations. The key step in this approach is to establish sufficient conditions to maintain the cell averages of the numerical solutions as PP and then apply a simple scaling limiter to enforce these conditions. This approach has been further extended to the SWEs, incorporating additional treatments to preserve both the PP and WB properties [38, 36]. More recently, a universal geometric quasilinearization (GQL) approach was proposed in [31] for bound-preserving problems with nonlinear constraints.

The resolution of localized structures in solutions to hyperbolic balance laws, such as shock waves and sharp transitions, often requires fine meshes. In these situations, adaptive moving mesh methods are highly effective in enhancing both the efficiency and quality of numerical solutions. These methods have played a crucial role in solving partial differential equations; see, for example, [4, 5, 6, 9, 10, 20, 23, 24, 26, 29, 30]. For SWEs specifically, an adaptive moving mesh kinetic flux-vector splitting method was introduced in [25]. In recent years, there has been growing interest in developing structure-preserving schemes on moving meshes. For instance, high-order adaptive moving mesh DG schemes were proposed in [41, 42], ensuring the preservation of non-negativity in water height and the lake at rest condition. In [40], a WB and PP finite volume weighted essentially non-oscillatory (WENO) arbitrary Lagrangian–Eulerian scheme was developed. More recently, high-order WB energy-stable adaptive moving mesh schemes for single- and multi-layer SWEs were proposed in [47, 48].

This paper aims to contribute to the development of high-order structure-preserving finite volume schemes for SWEs on adaptive moving structured meshes. These schemes maintain the WB property and ensure the non-negativity of water depth and preserve the positivity of the determinant of the Jacobi matrix of the coordinate transformation. The key elements of the proposed schemes include appropriate discretization of GCLs, numerical fluxes derived from hydrostatic reconstruction, special discretization of source terms to balance the flux gradient, and WENO reconstructions carefully designed in the computational domain. The primary efforts of this study include:

- We establish the WB property of our schemes in time-dependent curvilinear coordinates for the SWEs. The mesh movement poses new challenges, as it impacts the WB property. To address this, we achieve a balance through flux-source integration that incorporates surface conservation laws (SCLs) and mesh movement, aligned with volume conservation law (VCL) and bottom topography adjustments. The source terms are decomposed following the approach proposed in [35], numerical fluxes are designed through hydrostatic reconstruction, and the source term fluxes are meticulously crafted to balance these numerical fluxes. GCLs are discretized using linear interpolation coupled with PP limiter to also pre-

serve the free-stream property. Additional schemes for updating the bottom topography during mesh movement are integrated with the original SWEs to maintain mesh movement balance. The schemes are proven to be WB using the discrete GCLs and these two balances.

- We provide a rigorous analysis of the PP property for our proposed schemes. Due to the involvement of mesh metrics and movement, this analysis is complex, and standard techniques, such as splitting high-order schemes into convex combinations of formally first-order PP schemes, are not directly applicable. We prove that the proposed WB schemes are PP under a sufficient condition, enforced by a PP limiter. The PP property here refers to the non-negativity of the water depth and the positivity of the determinant of the Jacobi matrix of the coordinate transformation.
- We implement the proposed schemes on adaptive moving structured meshes. Mesh adaptation is achieved through iterative solutions of the Euler–Lagrange equations from a mesh adaptation functional, using a monitor function to focus mesh points around critical features. Various numerical experiments are conducted to validate the accuracy, robustness, and both WB and PP properties of the proposed schemes.

This paper is organized as follows. Section 2 introduces the SWEs with a technical decomposition of the source terms and the formulations in both Cartesian and curvilinear coordinates, along with a discussion of the WB property in curvilinear coordinates. Sections 3 and 4 present the high-order WB PP finite volume schemes on moving meshes for the one-dimensional (1D) and 2D SWEs, respectively. Section 5 details the adaptive moving mesh strategy. Section 6 conducts several numerical experiments to verify the high-order accuracy, structure-preserving properties, shock-capturing ability, and high efficiency of our schemes. Section 7 presents the conclusions of this paper.

2. Formulations of SWEs with technical decomposition of the source terms

This section introduces the SWEs with the decomposition of the source terms in both Cartesian and curvilinear coordinates.

2.1. Formulation of SWEs in Cartesian coordinates

The 2D SWEs (1) can be cast into the following form

$$\mathbf{U}_t + \nabla \cdot \mathbf{F}(\mathbf{U}) = \mathbf{S}(\mathbf{U}, \mathbf{x}), \quad (3)$$

where $\mathbf{F}(\mathbf{U}) = (\mathbf{F}_1(\mathbf{U}), \mathbf{F}_2(\mathbf{U}))$, and

$$\mathbf{U} = (h, hv_1, hv_2)^\top, \quad \mathbf{F}_1 = \left(hv_1, hv_1^2 + \frac{1}{2}gh^2, hv_1v_2 \right)^\top,$$

$$\mathbf{F}_2 = \left(hv_2, hv_1 v_2, hv_2^2 + \frac{1}{2}gh^2 \right)^\top, \quad \mathbf{S} = (0, -ghb_{x_1}, -ghb_{x_2})^\top,$$

represent the conservative variables, physical fluxes, and source terms, respectively. The steady-state solutions described in (2) and the source terms for the SWEs in (3) can be expressed using the formulations proposed in [35]. Specifically, the steady-state solutions (2) satisfy

$$\mathbf{U} + \mathbf{w}(\mathbf{x}) = C\mathbf{q}(\mathbf{x}), \quad (4)$$

where $\mathbf{w} = (b, 0, 0)^\top$ and $\mathbf{q} = (1, 0, 0)^\top$ are time-independent. The source terms $\mathbf{S}(\mathbf{U}, \mathbf{x})$ in (3) can be decomposed as

$$\mathbf{S}(\mathbf{U}, \mathbf{x}) = \sum_{m=1}^2 s_m(\mathbf{x}, t) ((\mathbf{r}_{m1})_{x_1}(\mathbf{x}) + (\mathbf{r}_{m2})_{x_2}(\mathbf{x})) = \sum_{m=1}^2 s_m(\mathbf{x}, t) \nabla_{\mathbf{x}} \cdot (\mathbf{r}_m(\mathbf{x})), \quad (5)$$

where $s_m(\mathbf{x}, t)$ and $\mathbf{r}_m(\mathbf{x}) = (\mathbf{r}_{m1}(\mathbf{x}), \mathbf{r}_{m2}(\mathbf{x}))$ are defined as

$$\begin{aligned} s_1 &= -g(h + b), \quad \mathbf{r}_{11} = (0, b, 0)^\top, \quad \mathbf{r}_{12} = (0, 0, b)^\top, \\ s_2 &= \frac{1}{2}g, \quad \mathbf{r}_{21} = (0, b^2, 0)^\top, \quad \mathbf{r}_{22} = (0, 0, b^2)^\top. \end{aligned}$$

In physics, the water depth should be nonnegative for the SWEs (3), meaning that the conservative vector \mathbf{U} should belong to the following admissible state set

$$\mathcal{G} = \left\{ \mathbf{U} = (h, hv_1, hv_2)^\top \in \mathbf{R}^3 : h \geq 0 \right\}.$$

The PP property of a numerical scheme for SWEs refers to maintaining the numerical solutions within the set \mathcal{G} .

2.2. Formulation of SWEs in curvilinear coordinates

This subsection will give the formulation of the SWEs in curvilinear coordinates. Denote Ω_c as the computational domain, and assume that there is a time-dependent, differentiable coordinate transformation $t = \tau, \mathbf{x} = \mathbf{x}(\tau, \xi)$ that maps from the computational domain Ω_c to the physical domain Ω_p . An adaptive mesh can be generated from the reference mesh in Ω_c based on such a transformation, as illustrated in [11, 12]. The determinant of the Jacobian matrix is $J = \det\left(\frac{\partial(t, \mathbf{x})}{\partial(\tau, \xi)}\right)$. The mesh metrics induced by this transformation satisfy the geometric conservation laws (GCLs), which include the volume conservation law (VCL) and the surface conservation laws (SCLs):

$$\begin{aligned} \text{VCL:} \quad & \frac{\partial J}{\partial \tau} + \sum_{\ell=1}^2 \frac{\partial}{\partial \xi_\ell} \left(J \frac{\partial \xi_\ell}{\partial t} \right) = 0, \\ \text{SCLs:} \quad & \sum_{\ell=1}^2 \frac{\partial}{\partial \xi_\ell} \left(J \frac{\partial \xi_\ell}{\partial x_k} \right) = 0, \quad k = 1, 2. \end{aligned} \quad (6)$$

Based on the GCLs and the decomposition (5), the 1D version of (3) in curvilinear coordinates can be written as

$$\frac{\partial JU}{\partial t} + \frac{\partial \mathcal{F}}{\partial \xi} = \sum_m s_m \frac{\partial \mathbf{r}_m}{\partial \xi}, \quad (7)$$

with

$$\mathcal{F} = J \frac{\partial \xi}{\partial t} U + F.$$

For the 2D case, (3) can be transformed into

$$\frac{\partial JU}{\partial t} + \sum_{\ell=1}^2 \frac{\partial \mathcal{F}_\ell}{\partial \xi_\ell} = \sum_{m=1}^2 s_m \sum_{\ell=1}^2 \frac{\partial \mathcal{R}_{m\ell}}{\partial \xi_\ell}, \quad (8)$$

and

$$\begin{aligned} \mathcal{F}_\ell &= J \frac{\partial \xi_\ell}{\partial t} U + \sum_{k=1}^2 J \frac{\partial \xi_\ell}{\partial x_k} \mathbf{F}_k = J \frac{\partial \xi_\ell}{\partial t} U + L_\ell \langle \mathbf{n}_\ell, \mathbf{F} \rangle = J \frac{\partial \xi_\ell}{\partial t} U + L_\ell \mathbf{F}_{n_\ell}, \\ \mathcal{R}_{m\ell} &= \sum_{k=1}^2 J \frac{\partial \xi_\ell}{\partial x_k} \mathbf{r}_{mk} = L_\ell \langle \mathbf{n}_\ell, \mathbf{r}_m \rangle = L_\ell (\mathbf{r}_m)_{n_\ell}, \end{aligned}$$

where

$$L_\ell = \sqrt{\sum_{k=1}^d \left(J \frac{\partial \xi_\ell}{\partial x_k} \right)^2}, \quad \mathbf{n}_\ell = \frac{1}{L_\ell} \left(J \frac{\partial \xi_\ell}{\partial x_1}, J \frac{\partial \xi_\ell}{\partial x_2} \right)^\top, \quad \langle \mathbf{n}_\ell, \mathbf{F} \rangle = (\mathbf{n}_\ell)_1 \mathbf{F}_1 + (\mathbf{n}_\ell)_2 \mathbf{F}_2. \quad (9)$$

Note that J should be positive to ensure valid interval length (1D) or cell area (2D) in the physical domain. The PP property of our adaptive moving mesh schemes aims to maintain $J > 0$ and ensure the numerical solutions within \mathcal{G} . Developing WB schemes in curvilinear coordinates for (8) is difficult, as the mesh movement also affects the WB property. Motivated by the previous work [47, 48], we separate the WB property in the time-dependent curvilinear coordinates into two parts.

- **Flux Source Balance:** This refers to the balance between the flux gradients and the source terms. Specifically, in curvilinear coordinates, the following equilibrium is required at the continuous case upon reaching a steady state:

$$\frac{\partial}{\partial \xi_\ell} \left(\sum_{k=1}^2 J \frac{\partial \xi_\ell}{\partial x_k} \mathbf{F}_k \right) = \sum_{m=1}^2 s_m \frac{\partial}{\partial \xi_\ell} \left(\sum_{k=1}^2 J \frac{\partial \xi_\ell}{\partial x_k} \mathbf{r}_{mk} \right).$$

- **Mesh Movement Balance:** This balance arises from mesh movement. Specifically, when the system reaches a steady state, the following equations associated with mesh movement must be satisfied:

$$\frac{\partial JU}{\partial t} + \sum_{\ell=1}^2 \frac{\partial}{\partial \xi_\ell} \left(J \frac{\partial \xi_\ell}{\partial t} U \right) = 0.$$

Furthermore, for the still water case of the SWEs, the conditions $h + b = C$ and $v_1 = v_2 = 0$ must be maintained, so that $\mathbf{U}(\mathbf{x}, t) + \mathbf{w}(\mathbf{x}) = C \mathbf{q}(\mathbf{x})$ remains preserved.

There are two approaches to computing \mathbf{w} and \mathbf{q} :

- \mathbf{w} and \mathbf{q} are obtained through their analytical expressions.
- \mathbf{w} and \mathbf{q} are treated as time-dependent variables, evolved concurrently with the original equations (3). This method includes the integration of an additional equation, $\partial b / \partial t = 0$, into the original equations.

While the first approach tends to be more accurate, especially in scenarios involving discontinuous bottom topography, it can compromise the WB property during mesh movement, as demonstrated in Theorems 3.1 and 4.1. Consequently, we opt for the second approach, which allows the numerical solutions to serve as high-order approximations of the analytical function b .

3. Structure-preserving schemes for 1D SWEs

For clarity, this section describes the high-order structure-preserving finite volume schemes for the 1D SWEs in curvilinear coordinates. In the 1D case, since $J \frac{\partial \xi}{\partial x} \equiv 1$, the SCL holds automatically. For the 1D SWEs, the conservative vector and flux are defined as

$$\mathbf{U} = (h, hv_1)^\top, \quad \mathbf{F} = \left(hv_1, hv_1^2 + \frac{1}{2}gh^2 \right)^\top, \quad s = (0, -ghb_{x_1})^\top,$$

where v_1 denotes the flow velocity. The steady state corresponding to still water is given by

$$h + b = C, \quad v_1 = 0,$$

which satisfy (4) with $\mathbf{w}(x) = (b, 0)^\top$ and $\mathbf{q}(x) = (1, 0)^\top$. The corresponding functions in the decomposition (5) become

$$s_1 = -g(h + b), \quad s_2 = \frac{1}{2}g, \quad \mathbf{r}_1 = (0, b)^\top, \quad \mathbf{r}_2 = (0, b^2)^\top.$$

The admissible state set is

$$\mathcal{G} = \left\{ \mathbf{U} = (h, hv_1)^\top \in \mathbf{R}^2 : h \geq 0 \right\}.$$

3.1. Outline of 1D structure-preserving finite volume schemes on moving meshes

Denote the computational domain as $[0, 1]$. Assume that a uniform computational mesh is used, given by $\xi_i = i\Delta\xi$, $i = 0, 1, \dots, N-1$, $\Delta\xi = 1/(N-1)$, and the cell $I_i = \left[\xi_{i-\frac{1}{2}}, \xi_{i+\frac{1}{2}} \right]$. The semi-discrete finite volume schemes for (7) can be expressed as

$$\frac{d(\overline{\mathbf{JU}})_i}{dt} = -\frac{1}{\Delta\xi} \left(\widetilde{\mathcal{F}}_{i+\frac{1}{2}} - \widetilde{\mathcal{F}}_{i-\frac{1}{2}} \right) + \frac{1}{\Delta\xi} \sum_{m=1}^2 (\bar{s}_m)_i \left((\widetilde{\mathcal{R}}_m)_{i+\frac{1}{2}} - (\widetilde{\mathcal{R}}_m)_{i-\frac{1}{2}} \right)$$

$$+ \frac{1}{\Delta\xi} \int_{I_i} \sum_{m=1}^2 (s_m - (\bar{s}_m)_i) \frac{\partial \mathcal{R}_m}{\partial \xi} d\xi, \quad (10)$$

$$\frac{d\bar{J}_i}{dt} = -\frac{1}{\Delta\xi} \left(\left(J \frac{\partial \xi}{\partial t} \right)_{i+\frac{1}{2}} - \left(J \frac{\partial \xi}{\partial t} \right)_{i-\frac{1}{2}} \right), \quad (11)$$

where

$$\widetilde{\mathcal{F}}_{i\pm\frac{1}{2}} = \left(J \frac{\partial \xi}{\partial t} \right)_{i\pm\frac{1}{2}} \{ \mathbf{U} \}_{i\pm\frac{1}{2}} - \frac{\alpha}{2} \{ \mathbf{U} \}_{i\pm\frac{1}{2}} + \widetilde{\mathbf{F}}_{i\pm\frac{1}{2}}, \quad \left(J \frac{\partial \xi}{\partial t} \right)_{i\pm\frac{1}{2}} = \left(\widehat{J \frac{\partial \xi}{\partial t}} \right)_{i\pm\frac{1}{2}} - \frac{\beta_J}{2} \{ J \}_{i\pm\frac{1}{2}}. \quad (12)$$

Here, $\left(\widehat{J \frac{\partial \xi}{\partial t}} \right)_{i\pm\frac{1}{2}} = -\dot{x}_{i\pm\frac{1}{2}}$, the notation \dot{x} represents the moving mesh velocity which will be defined in Section 5, and

$$\alpha = \max_i |\dot{x}_{i+\frac{1}{2}}|, \quad \beta_J = \max_i |\dot{x}_{i+\frac{1}{2}} / J_{i+\frac{1}{2}}|, \quad \{u\}_{i+\frac{1}{2}} = \frac{1}{2} (u_{i+\frac{1}{2}}^+ + u_{i+\frac{1}{2}}^-), \quad \{u\}_{i+\frac{1}{2}} = u_{i+\frac{1}{2}}^+ - u_{i+\frac{1}{2}}^-,$$

where the superscripts “+” and “−” indicate the right- and left-hand side limits at the cell interface. The procedure of obtaining $\mathbf{U}_{i\pm\frac{1}{2}}^\pm$ will be discussed in Subsections 3.2. The integral in equation (10) can be evaluated using numerical quadrature rules. Denote the quadrature points over cell I_i as $\{(\xi)_{i_\mu}\}$ with the corresponding weights $\{\omega_\mu\}$ and $\mu = 1, \dots, Q$. We use the notation $(\cdot)_{i_\mu}$ to represent the values at the quadrature points $\{(\xi)_{i_\mu}\}$ within cell I_i . Unless otherwise specified, the four-point ($Q = 4$) Gauss–Lobatto quadrature rule is adopted to achieve fifth-order accuracy. Then

$$\frac{1}{\Delta\xi} \int_{I_i} \sum_{m=1}^2 (s_m - (\bar{s}_m)_i) \frac{\partial \mathcal{R}_m}{\partial \xi} d\xi \approx \sum_{\mu=1}^Q \sum_{m=1}^2 \omega_\mu ((s_m)_{i_\mu} - (\bar{s}_m)_i) \left[\frac{\partial \mathcal{R}_m}{\partial \xi} \right]_{i_\mu}. \quad (13)$$

For WB considerations, the numerical fluxes in equation (10) are defined based on the hydrostatic reconstruction approach [1] as

$$\begin{aligned} \widetilde{\mathbf{F}}_{i+\frac{1}{2}} &= \widetilde{\mathbf{F}}_{i+\frac{1}{2}}^L = \widetilde{\mathbf{F}}_{i+\frac{1}{2}}(\mathbf{U}_{i+\frac{1}{2}}^{*,*}, \mathbf{U}_{i+\frac{1}{2}}^{+,*}) + \begin{pmatrix} 0 \\ \frac{g}{2} (h_{i+\frac{1}{2}}^-)^2 - \frac{g}{2} (h_{i+\frac{1}{2}}^{*,*})^2 \end{pmatrix}, \\ \widetilde{\mathbf{F}}_{i-\frac{1}{2}} &= \widetilde{\mathbf{F}}_{i-\frac{1}{2}}^R = \widetilde{\mathbf{F}}_{i-\frac{1}{2}}(\mathbf{U}_{i-\frac{1}{2}}^{*,*}, \mathbf{U}_{i-\frac{1}{2}}^{+,*}) + \begin{pmatrix} 0 \\ \frac{g}{2} (h_{i-\frac{1}{2}}^+)^2 - \frac{g}{2} (h_{i-\frac{1}{2}}^{+,*})^2 \end{pmatrix}, \\ (\widetilde{\mathcal{R}}_m)_{i+\frac{1}{2}} &= (\mathcal{R}_m)_{i+\frac{1}{2}}^-, \quad (\widetilde{\mathcal{R}}_m)_{i-\frac{1}{2}} = (\mathcal{R}_m)_{i-\frac{1}{2}}^+ \end{aligned} \quad (14)$$

with

$$\begin{aligned} \widetilde{\mathbf{F}}(\mathbf{U}_1, \mathbf{U}_2) &= \frac{1}{2} (\mathbf{F}(\mathbf{U}_1) + \mathbf{F}(\mathbf{U}_2)) - \frac{\beta}{2} (\mathbf{U}_2 - \mathbf{U}_1), \quad \beta = \max_i (|\bar{v}_1|_i + \sqrt{g\bar{h}_i}), \\ \mathbf{U}_{i\pm\frac{1}{2}}^{\pm,*} &= \begin{pmatrix} h_{i\pm\frac{1}{2}}^{\pm,*} \\ h_{i\pm\frac{1}{2}}^{\pm,*} (v_1)_{i\pm\frac{1}{2}}^\pm \end{pmatrix}, \quad h_{i\pm\frac{1}{2}}^{\pm,*} = \max \left(0, h_{i\pm\frac{1}{2}}^\pm + b_{i\pm\frac{1}{2}}^\pm - \max(b_{i\pm\frac{1}{2}}^+, b_{i\pm\frac{1}{2}}^-) \right). \end{aligned}$$

Similar to the findings in [35], when a steady state is reached, we have

$$\widetilde{\mathbf{F}}_{i\pm\frac{1}{2}} - \sum_{m=1}^2 (\bar{s}_m)_i (\widetilde{\mathbf{R}}_m)_{i\pm\frac{1}{2}} \equiv C. \quad (15)$$

As discussed in Section 2.2, the computations of \mathbf{w} and \mathbf{q} are crucial for maintaining well-balancedness. The governing equations for \mathbf{w} and \mathbf{q} in curvilinear coordinates are given by

$$\frac{\partial J\mathbf{w}}{\partial t} + \frac{\partial}{\partial \xi} \left(J \frac{\partial \xi}{\partial t} \mathbf{w} \right) = 0, \quad \frac{\partial J\mathbf{q}}{\partial t} + \frac{\partial}{\partial \xi} \left(J \frac{\partial \xi}{\partial t} \mathbf{q} \right) = 0.$$

From these equations, we devise the following semi-discrete scheme for \mathbf{w} and \mathbf{q} :

$$\frac{d(\overline{J\mathbf{w}})_i}{dt} = -\frac{1}{\Delta \xi} \left(\widetilde{\mathbf{w}}_{i+\frac{1}{2}} - \widetilde{\mathbf{w}}_{i-\frac{1}{2}} \right), \quad (16)$$

$$\frac{d(\overline{J\mathbf{q}})_i}{dt} = -\frac{1}{\Delta \xi} \left(\widetilde{\mathbf{q}}_{i+\frac{1}{2}} - \widetilde{\mathbf{q}}_{i-\frac{1}{2}} \right), \quad (17)$$

which updates the numerical values of \mathbf{w} and \mathbf{q} from the old mesh to the new mesh, with

$$\begin{aligned} \widetilde{\mathbf{w}}_{i\pm\frac{1}{2}} &= \left(J \frac{\partial \xi}{\partial t} \right)_{i\pm\frac{1}{2}} \llbracket \mathbf{w} \rrbracket_{i\pm\frac{1}{2}} - \frac{\alpha}{2} \llbracket \mathbf{w} \rrbracket_{i\pm\frac{1}{2}}, \\ \widetilde{\mathbf{q}}_{i\pm\frac{1}{2}} &= \left(J \frac{\partial \xi}{\partial t} \right)_{i\pm\frac{1}{2}} \llbracket \mathbf{q} \rrbracket_{i\pm\frac{1}{2}} - \frac{\alpha}{2} \llbracket \mathbf{q} \rrbracket_{i\pm\frac{1}{2}}. \end{aligned} \quad (18)$$

The cell averages of \mathbf{U} , \mathbf{w} , and \mathbf{q} in physical domain are then computed by

$$\overline{\mathbf{U}}_i := \frac{\overline{J\mathbf{U}}_i}{\overline{J}_i} = \frac{\int_{I_i} J\mathbf{U}d\xi}{\int_{I_i} Jd\xi}, \quad \overline{\mathbf{w}}_i := \frac{\overline{J\mathbf{w}}_i}{\overline{J}_i} = \frac{\int_{I_i} J\mathbf{w}d\xi}{\int_{I_i} Jd\xi}, \quad \overline{\mathbf{q}}_i := \frac{\overline{J\mathbf{q}}_i}{\overline{J}_i} = \frac{\int_{I_i} J\mathbf{q}d\xi}{\int_{I_i} Jd\xi}.$$

The quadrature rules are used here to approximate the integral, e.g., $\overline{\mathbf{U}}_i = \sum_{\mu=1}^Q \omega_\mu J_{i_\mu} \mathbf{U}_{i_\mu} / \sum_{\mu=1}^Q \omega_\mu J_{i_\mu}$.

3.2. High-order 1D reconstruction

This subsection discusses the 1D WENO reconstruction in the computational domain. It is crucial to obtain high-order accurate approximate values of \mathbf{U} at the quadrature nodes $\{(\xi)_{i_\mu}\}$ when calculating the integral in (13). We utilize the WENO-Z reconstruction technique [3], specifically adapted to accommodate steady-state conditions during mesh movement. In this work, we employ the following reconstruction approach:

Step 1. Starting with the cell average values $\overline{J\mathbf{U}}_i$ and \overline{J}_i , we apply the WENO reconstructions to obtain the high-order approximate values $\{J\mathring{\mathbf{U}}_{i_\mu}\}$ and $\{J_{i_\mu}\}$ of $J\mathbf{U}$ and \mathbf{U} at the quadrature nodes $\{(\xi)_{i_\mu}\}$. Then $\mathring{\mathbf{U}}_{i_\mu} = J\mathring{\mathbf{U}}_{i_\mu}/J_{i_\mu}$ serves as the high-order approximations for \mathbf{U} at the quadrature points. To enforce the cell average of J , we modify $J_{i_\mu} = \mathring{J}_{i_\mu} + \overline{J}_i - \sum_{\mu} \omega_\mu \mathring{J}_{i_\mu}$ to obtain $\sum_{\mu} \omega_\mu J_{i_\mu} = \overline{J}_i$.

Step 2. Calculate the approximate cell average $\tilde{U}_i = \sum_{\mu} \omega_{\mu} \hat{U}_{i_{\mu}}$ over cell I_i within the computational domain. Using these cell averages $\{\tilde{U}_i\}$, employ the WENO reconstruction to ascertain the robust high-order approximate values $\check{U}_{i_{\mu}}$ at the quadrature points $\{(\xi)_{i_{\mu}}\}$. Denote the difference between the cell average \overline{JU}_i and the values $\sum_{\mu} \omega_{\mu} J_{i_{\mu}} \check{U}_{i_{\mu}}$ over cell I_i by $\gamma_i = \overline{JU}_i - (\sum_{\mu} \omega_{\mu} J_{i_{\mu}} \check{U}_{i_{\mu}})$. To maintain the cell average after the reconstruction procedure. The reconstruction values are modified as $U_{i_{\mu}} = \check{U}_{i_{\mu}} + \gamma_i / J_{i_{\mu}}$. Therefore, $\sum_{\mu} \omega_{\mu} J_{i_{\mu}} U_{i_{\mu}} = \overline{JU}_i$.

Remark 1. The modifications in Steps 1 and 2 are essential for the PP analysis in Theorems 3.2 and 3.3 and maintain the accuracy and conservation in the computational domain during the reconstruction procedure. Take the modification in Step 1 as an example. Assume that J is sufficiently smooth. If the fifth-order WENO reconstruction is employed, one has $\hat{J}_{i_{\mu}} = J_{i_{\mu}}^{exact} + O((\Delta\xi)^5)$, where $J_{i_{\mu}}^{exact}$ represents the exact value of J at the quadrature points $(\xi)_{i_{\mu}}$ within I_i . Noting that the exact value $J_{i_{\mu}}^{exact}$ and the numerical cell average \bar{J}_i satisfy the relation $\sum_{\mu} \omega_{\mu} J_{i_{\mu}}^{exact} = \bar{J}_i + O((\Delta\xi)^5)$, one obtains $\sum_{\mu} \omega_{\mu} \hat{J}_{i_{\mu}} = \sum_{\mu} \omega_{\mu} J_{i_{\mu}}^{exact} + O((\Delta\xi)^5) = \bar{J}_i + O((\Delta\xi)^5)$. Therefore, $\bar{J}_i - \sum_{\mu} \omega_{\mu} \hat{J}_{i_{\mu}} = O((\Delta\xi)^5)$. Consequently,

$$J_{i_{\mu}} = \hat{J}_{i_{\mu}} + \bar{J}_i - \sum_{\mu} \omega_{\mu} \hat{J}_{i_{\mu}} = J_{i_{\mu}}^{exact} + O((\Delta\xi)^5) + \bar{J}_i - \sum_{\mu} \omega_{\mu} \hat{J}_{i_{\mu}} = J_{i_{\mu}}^{exact} + O((\Delta\xi)^5),$$

which means this modification does not affect the accuracy. From $J_{i_{\mu}} = \hat{J}_{i_{\mu}} + \bar{J}_i - \sum_{\mu} \omega_{\mu} \hat{J}_{i_{\mu}}$, one obtains $\sum_{\mu} \omega_{\mu} J_{i_{\mu}} = \sum_{\mu} \omega_{\mu} \hat{J}_{i_{\mu}} + \sum_{\mu} \omega_{\mu} \bar{J}_i - \sum_{\mu} \omega_{\mu} \sum_{\bar{\mu}} \omega_{\bar{\mu}} \hat{J}_{i_{\bar{\mu}}}$. Since $\sum_{\mu} \omega_{\mu} = 1$, one has $\sum_{\mu} \omega_{\mu} J_{i_{\mu}} = \sum_{\mu} \omega_{\mu} \hat{J}_{i_{\mu}} + \bar{J}_i - \sum_{\bar{\mu}} \omega_{\bar{\mu}} \hat{J}_{i_{\bar{\mu}}} = \bar{J}_i$, which implies this modification ensures the conservative property of J in the computational domain. Similar to the analysis for J in Step 1, the modification in Step 2 does not affect the accuracy and conservation in the computational domain. Note that $\bar{U}_i = \overline{JU}_i / \bar{J}_i$, $\sum_{\mu} \omega_{\mu} J_{i_{\mu}} U_{i_{\mu}} = \overline{JU}_i$, and $\sum_{\mu} \omega_{\mu} J_{i_{\mu}} = \bar{J}_i$. The modifications do not influence the conservation in the physical domain during the reconstruction procedure, as we merely modify the reconstruction values at the quadrature points.

Remark 2. It seems more straightforward to directly use Step 1 to calculate the reconstruction values $\hat{U}_{i_{\mu}}$ at the quadrature points $(\xi)_{i_{\mu}}$. This strategy also preserves to the free-stream property. However, our numerical experiments indicate that merely performing Step 1 can result in significant overshoots or undershoots near discontinuities, as illustrated in Figure 5. To address this issue, we use the reconstruction approach consisting of Steps 1 and 2.

Remark 3. During mesh movement, it is crucial that the coefficients used for the reconstruction in $J(h^{\circ} + b)_{i_{\mu}}$ and $\hat{J}_{i_{\mu}}$ remain identical. Specifically, if $J(h^{\circ} + b)_{i+\frac{1}{2}}$ is reconstructed as $\sum_{l=-\gamma+1}^{\gamma-1} w_l \overline{J(h+b)_{i+l}}$

to determine the left limit of $J(h+b)$, then $\bar{J}_{i+\frac{1}{2}}^-$ must be similarly reconstructed using the same weights: $\sum_{l=-\gamma+1}^{\gamma-1} w_l \bar{J}_{i+l}$. This consistent treatment ensures that the ratio $\frac{J(h+b)_{i+\frac{1}{2}}^-}{\bar{J}_{i+\frac{1}{2}}^-} = C$, which is crucial under still water equilibrium conditions, where $(v_1)_{i+\frac{1}{2}}^- = 0$. Therefore, the relationships $\bar{U}_{i_\mu} + \bar{w}_{i_\mu} = Cq_{i_\mu}$ and $\bar{U}_{i_\mu} + \bar{w}_{i_\mu} = Cq_{i_\mu}$ are maintained, aligning with the principles of hydrostatic balance. We modify $w_{i_\mu} = \bar{w}_{i_\mu} - \gamma_i/J_{i_\mu}$ to ensure $U_{i_\mu} + w_{i_\mu} = Cq_{i_\mu}$. This is important for the WB property of our scheme under mesh movement.

The condition

$$J_{i_\mu} > 0, \quad h_{i_\mu} \geq 0 \quad \forall i, \forall \mu, \quad (19)$$

is essential for the PP property of our moving mesh finite volume schemes in Theorems 3.2 and 3.3. However, the reconstruction procedure does not always guarantee satisfaction of condition (19). Following [44, 46, 38, 43], a PP limiter should be implemented to enforce this condition.

Remark 4 (1D PP limiter). If $\bar{J}_i > 0$ and $\bar{h}_i \geq 0$, the PP limiter modifies the reconstructed values $\{J_{i_\mu}\}$ and $\{h_{i_\mu}\}$ as

$$\widehat{J}_{i_\mu} = \theta_J (J_{i_\mu} - \bar{J}_i) + \bar{J}_i, \quad \widehat{h}_{i_\mu} = \theta_h (h_{i_\mu} - \bar{h}_i) + \bar{h}_i \quad \forall \mu \quad (20)$$

with

$$\theta_J := \begin{cases} 1, & \text{if } \min_{\mu} \{J_{i_\mu}\} = \bar{J}_i, \\ \min \left\{ \left| \frac{\bar{J}_i - \epsilon_0}{J_{i_\mu} - \min_{\mu} \{J_{i_\mu}\}} \right|, 1 \right\}, & \text{otherwise,} \end{cases} \quad (21)$$

$$\theta_h := \begin{cases} 1, & \text{if } \min_{\mu} \{h_{i_\mu}\} = \bar{h}_i, \\ \min \left\{ \left| \frac{\bar{h}_i}{\bar{h}_i - \min_{\mu} \{h_{i_\mu}\}} \right|, 1 \right\}, & \text{otherwise.} \end{cases} \quad (22)$$

The value ϵ_0 is a small positive number, which represents the desired lower bound of J and can be taken as $\epsilon_0 = \min \{10^{-13}, \bar{J}_i\}$. After applying the PP limiter, the modified values, given by (20), satisfy $\widehat{J}_{i_\mu} > 0$ and $\widehat{h}_{i_\mu} \geq 0$. Notice that, if $h_{i_\mu} \geq 0$, one has $\theta_h = 1$ and $\widehat{h}_{i_\mu} = h_{i_\mu}$. We use \widehat{J}_{i_μ} to replace J_{i_μ} in Step 2 so as to ensure $\sum_{\mu} \omega_{\mu} \widehat{J}_{i_\mu} U_{i_\mu} = \bar{J} \bar{U}_i$.

If $\bar{J}_i > 0$ and $\bar{h}_i \geq 0$, the PP limiter maintains high-order accuracy, as discussed in [44, 38, 43]. However, it may impact the WB property under still water equilibrium conditions. To address this issue, following [41], we update the bottom topography by $\widehat{b}_{i_\mu} = h_{i_\mu} + b_{i_\mu} - \widehat{h}_{i_\mu}$. When a steady state is reached, we have $h_{i_\mu} + b_{i_\mu} \equiv C$, $(v_1)_{i_\mu} = 0$, and then $\widehat{h}_{i_\mu} + \widehat{b}_{i_\mu} \equiv C$. In our computations, we use $\widehat{U}_{i_\mu} = (\widehat{h}_{i_\mu}, (hv_1)_{i_\mu})^\top$, $\widehat{w}_{i_\mu} = (\widehat{b}_{i_\mu}, 0)^\top$ and \widehat{J}_{i_μ} to replace U_{i_μ} , w_{i_μ} and J_{i_μ} respectively. Hence, $\widehat{U}_{i_\mu} + \widehat{w}_{i_\mu} = U_{i_\mu} + w_{i_\mu} = Cq_{i_\mu}$. This modification ensures the maintenance of the WB property while simultaneously preserving the non-negativity of the water depth. The

conservative property is preserved, since the cell averages of the conservative variables \bar{h}_i and $(\overline{h\nu_1})_i$ do not change. Specifically

$$\begin{aligned} \frac{\sum_{\mu} \omega_{\mu} \widehat{J}_{i_{\mu}} \widehat{h}_{i_{\mu}}}{\sum_{\mu} \omega_{\mu} \widehat{J}_{i_{\mu}}} &= \frac{\sum_{\mu} \omega_{\mu} \widehat{J}_{i_{\mu}} (\theta (h_{i_{\mu}} - \bar{h}_i) + \bar{h}_i)}{\sum_{\mu} \omega_{\mu} \widehat{J}_{i_{\mu}}} = \frac{\theta \left(\sum_{\mu} \omega_{\mu} \widehat{J}_{i_{\mu}} h_{i_{\mu}} - \bar{J} \bar{h}_i \right) + \bar{J} \bar{h}_i}{\bar{J}_i} = \bar{h}_i, \\ \frac{\sum_{\mu} \omega_{\mu} \widehat{J}_{i_{\mu}} (h\nu_1)_{i_{\mu}}}{\sum_{\mu} \omega_{\mu} \widehat{J}_{i_{\mu}}} &= \frac{\overline{J(h\nu_1)}_i}{\bar{J}_i} = (\overline{h\nu_1})_i. \end{aligned}$$

Therefore, the conservation is preserved.

3.3. Analysis of WB property

This subsection shows the WB property of the proposed schemes.

Theorem 3.1. Consider the semi-discrete schemes (10), (11), (16), and (17) with the numerical fluxes (12) and (18). These schemes are WB, in the sense that, under the forward Euler or explicit SSP RK discretizations, when a steady state is reached at the n th time level t^n , i.e.,

$$\bar{U}_i^n + \bar{w}_i^n = C \bar{q}_i^n \quad \forall i,$$

the numerical solution at t^{n+1} also satisfies

$$\bar{U}_i^{n+1} + \bar{w}_i^{n+1} = C \bar{q}_i^{n+1} \quad \forall i.$$

Proof. Since an SSP RK method is a convex combination of forward Euler method, we only need to show the conclusion for the forward Euler discretization. When the steady state is reached at time t^n , the condition (15) holds, and the discrete evolution of JU can be expressed as follows:

$$(\overline{JU})_i^{n+1} - (\overline{JU})_i^n = -\frac{\Delta t}{\Delta \xi} \left(\left(J \frac{\partial \xi}{\partial t} \right)_{i+\frac{1}{2}} \llbracket U \rrbracket_{i+\frac{1}{2}} - \frac{\alpha}{2} \llbracket U \rrbracket_{i+\frac{1}{2}} - \left(J \frac{\partial \xi}{\partial t} \right)_{i-\frac{1}{2}} \llbracket U \rrbracket_{i-\frac{1}{2}} + \frac{\alpha}{2} \llbracket U \rrbracket_{i-\frac{1}{2}} \right), \quad (23)$$

where and hereafter the superscript n is omitted for convenience. The fully-discrete schemes of Jw and Jq are given by

$$(\overline{Jw})_i^{n+1} - (\overline{Jw})_i^n = -\frac{\Delta t}{\Delta \xi} \left(\left(J \frac{\partial \xi}{\partial t} \right)_{i+\frac{1}{2}} \llbracket w \rrbracket_{i+\frac{1}{2}} - \frac{\alpha}{2} \llbracket w \rrbracket_{i+\frac{1}{2}} - \left(J \frac{\partial \xi}{\partial t} \right)_{i-\frac{1}{2}} \llbracket w \rrbracket_{i-\frac{1}{2}} + \frac{\alpha}{2} \llbracket w \rrbracket_{i-\frac{1}{2}} \right), \quad (24)$$

$$(\overline{Jq})_i^{n+1} - (\overline{Jq})_i^n = -\frac{\Delta t}{\Delta \xi} \left(\left(J \frac{\partial \xi}{\partial t} \right)_{i+\frac{1}{2}} \llbracket q \rrbracket_{i+\frac{1}{2}} - \frac{\alpha}{2} \llbracket q \rrbracket_{i+\frac{1}{2}} - \left(J \frac{\partial \xi}{\partial t} \right)_{i-\frac{1}{2}} \llbracket q \rrbracket_{i-\frac{1}{2}} + \frac{\alpha}{2} \llbracket q \rrbracket_{i-\frac{1}{2}} \right). \quad (25)$$

Summing (23) and (24) yields

$$\begin{aligned} \left(\overline{J(U + \mathbf{w})}\right)_i^{n+1} - \left(\overline{J(U + \mathbf{w})}\right)_i^n &= -\frac{\Delta t}{\Delta \xi} \left(\left(J \frac{\partial \xi}{\partial t} \right)_{i+\frac{1}{2}} \{\!\!\{ U + \mathbf{w} \}\!\!\}_{i+\frac{1}{2}} - \frac{\alpha}{2} \llbracket U + \mathbf{w} \rrbracket_{i+\frac{1}{2}} \right. \\ &\quad \left. - \left(J \frac{\partial \xi}{\partial t} \right)_{i-\frac{1}{2}} \{\!\!\{ U + \mathbf{w} \}\!\!\}_{i-\frac{1}{2}} + \frac{\alpha}{2} \llbracket U + \mathbf{w} \rrbracket_{i-\frac{1}{2}} \right). \end{aligned}$$

Based on the relation $U_{i_\mu} + \mathbf{w}_{i_\mu} = C\mathbf{q}_{i_\mu}$, one obtains $\{\!\!\{ U + \mathbf{w} \}\!\!\} = C\{\!\!\{ \mathbf{q} \}\!\!\}$ and $\llbracket U + \mathbf{w} \rrbracket = C\llbracket \mathbf{q} \rrbracket$. This implies

$$\begin{aligned} \left(\overline{J(U + \mathbf{w})}\right)_i^{n+1} - \left(\overline{J(C\mathbf{q})}\right)_i^n &= -\frac{\Delta t}{\Delta \xi} \left(\left(J \frac{\partial \xi}{\partial t} \right)_{i+\frac{1}{2}} \{\!\!\{ C\mathbf{q} \}\!\!\}_{i+\frac{1}{2}} - \frac{\alpha}{2} \llbracket C\mathbf{q} \rrbracket_{i+\frac{1}{2}} \right. \\ &\quad \left. - \left(J \frac{\partial \xi}{\partial t} \right)_{i-\frac{1}{2}} \{\!\!\{ C\mathbf{q} \}\!\!\}_{i-\frac{1}{2}} + \frac{\alpha}{2} \llbracket C\mathbf{q} \rrbracket_{i-\frac{1}{2}} \right). \end{aligned}$$

Plugging (25) into the above equations, one obtains

$$\left(\overline{J(U + \mathbf{w})}\right)_i^{n+1} - \left(\overline{J(C\mathbf{q})}\right)_i^{n+1} = 0,$$

which implies

$$\left(\overline{U + \mathbf{w}}\right)_i^{n+1} = C\overline{\mathbf{q}}_i^{n+1}.$$

The proof is completed. □

3.4. Analysis of PP property

The semi-discrete schemes (10) and (11) coupled with the forward Euler time discretization can be expressed as

$$\overline{JU}_i^{\Delta t} = \overline{JU}_i - \Delta t L_i, \quad \overline{J}_i^{\Delta t} = \overline{J}_i - \Delta t L_i,$$

where L_i and L_i denote the right-hand-side terms of (10) and (11), respectively; \overline{JU}_i and \overline{J}_i represent the approximations at the n th time level.

Theorem 3.2. Assume that $\overline{J}_i > 0$ for all i . If $J_{i_\mu} > 0$ for all i, μ , then $\overline{J}_i^{\Delta t} > 0$ holds under the condition

$$\Delta t \leq \frac{\omega_1 \Delta \xi}{\beta_J}. \quad (26)$$

Proof. Consider the discrete evolution equation for J :

$$\begin{aligned}
\bar{J}_i^{\Delta t} - \bar{J}_i &= -\frac{\Delta t}{\Delta \xi} \left[\left(J \frac{\partial \xi}{\partial t} \right)_{i+\frac{1}{2}} - \frac{\beta_J}{2} \llbracket J \rrbracket_{i+\frac{1}{2}} - \left(J \frac{\partial \xi}{\partial t} \right)_{i-\frac{1}{2}} + \frac{\beta_J}{2} \llbracket J \rrbracket_{i-\frac{1}{2}} \right] \\
&= \frac{\Delta t}{2\Delta \xi} \left[\beta_J J_{i+\frac{1}{2}}^+ - \left(J \frac{\partial \xi}{\partial t} \right)_{i+\frac{1}{2}} + \beta_J J_{i+\frac{1}{2}}^- - \left(J \frac{\partial \xi}{\partial t} \right)_{i+\frac{1}{2}} \right] \\
&\quad + \frac{\Delta t}{2\Delta \xi} \left[\beta_J J_{i-\frac{1}{2}}^+ + \left(J \frac{\partial \xi}{\partial t} \right)_{i-\frac{1}{2}} + \beta_J J_{i-\frac{1}{2}}^- + \left(J \frac{\partial \xi}{\partial t} \right)_{i-\frac{1}{2}} \right] \\
&\quad - \frac{\beta_J \Delta t}{\Delta \xi} \left(J_{i+\frac{1}{2}}^- + J_{i-\frac{1}{2}}^+ \right).
\end{aligned} \tag{27}$$

Noting that

$$\beta_J J_{i+\frac{1}{2}}^\pm - \left(J \frac{\partial \xi}{\partial t} \right)_{i+\frac{1}{2}} \geq 0, \quad \beta_J J_{i-\frac{1}{2}}^\pm + \left(J \frac{\partial \xi}{\partial t} \right)_{i-\frac{1}{2}} \geq 0, \quad \bar{J}_i = \sum_{\mu=2}^{Q-1} \omega_\mu J_{i_\mu} + \omega_1 \left(J_{i+\frac{1}{2}}^- + J_{i-\frac{1}{2}}^+ \right),$$

a lower bound of the right-hand-side of (27) is given by

$$\begin{aligned}
\bar{J}_i^{\Delta t} &\geq \sum_{\mu=2}^{Q-1} \omega_\mu J_{i_\mu} + \omega_1 \left(J_{i+\frac{1}{2}}^- + J_{i-\frac{1}{2}}^+ \right) - \frac{\beta_J \Delta t}{\Delta \xi} \left(J_{i+\frac{1}{2}}^- + J_{i-\frac{1}{2}}^+ \right) \\
&= \left(\omega_1 - \frac{\beta_J \Delta t}{\Delta \xi} \right) \left(J_{i+\frac{1}{2}}^- + J_{i-\frac{1}{2}}^+ \right) + \sum_{\mu=2}^{Q-1} \omega_\mu J_{i_\mu}.
\end{aligned}$$

Under the condition $J_{i_\mu} > 0$ and the condition (26), one obtains

$$\bar{J}_i^{\Delta t} > 0.$$

The proof is completed. \square

Remark 5. The mesh should not interleave or overlap during computation, i.e., if $x_{i-\frac{1}{2}} < x_{i+\frac{1}{2}}$ for $i = 0, \dots, N-1$ then for the new mesh $x_{i-\frac{1}{2}}^{\Delta t} < x_{i+\frac{1}{2}}^{\Delta t}$ still holds, otherwise the numerical simulation will fail. The treatment to avoid mesh interleaving or overlapping is illustrated in Section 5.

Theorem 3.3. Assume that $\bar{U}_i \in \mathcal{G}$ and $\bar{J}_i > 0$ for all i . If $\bar{J}_i^{\Delta t} > 0$, and

$$J_{i_\mu} > 0, \quad h_{i_\mu} \geq 0 \quad \forall i, \forall \mu, \tag{28}$$

then the PP property

$$\bar{U}_i^{\Delta t} := \bar{J} \bar{U}_i^{\Delta t} / \bar{J}_i^{\Delta t} \in \mathcal{G},$$

holds under the CFL condition

$$\Delta t \leq \frac{\omega_1 \Delta \xi}{\alpha + \beta} \min_i \left\{ J_{i \pm \frac{1}{2}}^\mp \right\}. \tag{29}$$

Proof. Consider the discrete evolution equation for Jh :

$$\begin{aligned} \overline{Jh}_i^{\Delta t} - \overline{Jh}_i = & -\frac{\Delta t}{\Delta \xi} \left[\left(J \frac{\partial \xi}{\partial t} \right)_{i+\frac{1}{2}} \llbracket h \rrbracket_{i+\frac{1}{2}} - \frac{\alpha}{2} \llbracket h \rrbracket_{i+\frac{1}{2}} - \left(J \frac{\partial \xi}{\partial t} \right)_{i-\frac{1}{2}} \llbracket h \rrbracket_{i-\frac{1}{2}} + \frac{\alpha}{2} \llbracket h \rrbracket_{i-\frac{1}{2}} \right] \\ & - \frac{\Delta t}{\Delta \xi} \left[\frac{1}{2} \left(h_{i+\frac{1}{2}}^{-,*}(v_1)_{i+\frac{1}{2}}^- + h_{i+\frac{1}{2}}^{+,*}(v_1)_{i+\frac{1}{2}}^+ \right) - \frac{\beta}{2} \llbracket h \rrbracket_{i+\frac{1}{2}}^* \right. \\ & \left. - \frac{1}{2} \left(h_{i-\frac{1}{2}}^{-,*}(v_1)_{i-\frac{1}{2}}^- + h_{i-\frac{1}{2}}^{+,*}(v_1)_{i-\frac{1}{2}}^+ \right) + \frac{\beta}{2} \llbracket h \rrbracket_{i-\frac{1}{2}}^* \right], \end{aligned} \quad (30)$$

Based on the relations

$$\begin{aligned} \pm \frac{1}{2} \left(h_{i\pm\frac{1}{2}}^{-,*}(v_1)_{i\pm\frac{1}{2}}^- + h_{i\pm\frac{1}{2}}^{+,*}(v_1)_{i\pm\frac{1}{2}}^+ \right) & \leq \beta \llbracket h \rrbracket_{i\pm\frac{1}{2}}^*, \\ \frac{\alpha}{2} \llbracket h \rrbracket_{i+\frac{1}{2}} - \frac{\alpha}{2} \llbracket h \rrbracket_{i-\frac{1}{2}} & = \alpha \llbracket h \rrbracket_{i+\frac{1}{2}} + \alpha \llbracket h \rrbracket_{i-\frac{1}{2}} - \alpha h_{i+\frac{1}{2}}^- - \alpha h_{i-\frac{1}{2}}^+, \end{aligned}$$

the lower bound of the right-hand side of (30) can be estimated as

$$\overline{Jh}_i^{\Delta t} - \overline{Jh}_i \geq I_1 + I_2 \quad (31)$$

with

$$\begin{aligned} I_1 & = \frac{\Delta t}{\Delta \xi} \left[\left(\alpha - J \frac{\partial \xi}{\partial t} \right)_{i+\frac{1}{2}} \llbracket h \rrbracket_{i+\frac{1}{2}} + \left(\alpha + J \frac{\partial \xi}{\partial t} \right)_{i-\frac{1}{2}} \llbracket h \rrbracket_{i-\frac{1}{2}} \right], \\ I_2 & = -\frac{\Delta t}{\Delta \xi} \left[\beta h_{i+\frac{1}{2}}^{-,*} + \beta h_{i-\frac{1}{2}}^{+,*} + \alpha h_{i+\frac{1}{2}}^- + \alpha h_{i-\frac{1}{2}}^+ \right]. \end{aligned}$$

Noting that $I_1 \geq 0$ and $h_{i\pm\frac{1}{2}}^{\mp,*} \leq h_{i\pm\frac{1}{2}}^{\mp}$, one has

$$\overline{h}_i^{\Delta t} - \frac{\overline{Jh}_i}{\overline{J}_i^{\Delta t}} \geq -\frac{\Delta t}{\overline{J}_i^{\Delta t} \Delta \xi} \left[(\alpha + \beta) h_{i+\frac{1}{2}}^+ + (\alpha + \beta) h_{i-\frac{1}{2}}^+ \right]. \quad (32)$$

Furthermore, by using the fact

$$\overline{Jh}_i = \sum_{\mu=2}^{Q-1} \omega_{\mu} J_{i_{\mu}} h_{i_{\mu}} + \omega_1 \left(J_{i+\frac{1}{2}}^- h_{i+\frac{1}{2}}^- + J_{i-\frac{1}{2}}^+ h_{i-\frac{1}{2}}^+ \right),$$

the inequality (32) can be reformulated as

$$\overline{h}_i^{\Delta t} \geq \frac{1}{\overline{J}_i^{\Delta t}} \left[\left(\omega_1 J_{i+\frac{1}{2}}^- - \frac{\Delta t}{\Delta \xi} (\alpha + \beta) \right) h_{i+\frac{1}{2}}^- + \left(\omega_1 J_{i-\frac{1}{2}}^+ - \frac{\Delta t}{\Delta \xi} (\alpha + \beta) \right) h_{i-\frac{1}{2}}^+ \right] + \frac{1}{\overline{J}_i^{\Delta t}} \sum_{\mu=2}^{Q-1} \omega_{\mu} J_{i_{\mu}} h_{i_{\mu}},$$

where we have used the facts $h_{i-\frac{1}{2}}^+ = h_{i_1}$ and $h_{i+\frac{1}{2}}^- = h_{i_Q}$ for the adopted Gauss–Lobatto quadrature. Under the condition (28) and the CFL condition (29), one obtains

$$\overline{h}_i^{\Delta t} \geq 0,$$

which means $\overline{U}_i^{\Delta t} \in \mathcal{G}$. The proof is completed. \square

4. Structure-preserving schemes for 2D SWEs

This section presents the high-order structure-preserving finite volume schemes for the 2D SWEs in curvilinear coordinates. In the 2D scenario, the SCLs in (6) become nontrivial and must be preserved under appropriate discretization.

4.1. Outline of 2D structure-preserving finite volume schemes on moving meshes

Denote the computational domain by $[0, 1] \times [0, 1]$. Assume a uniform mesh configuration, defined as follows:

$$\begin{aligned} (\xi_1)_i &= i\Delta\xi_1, \quad i = 0, 1, \dots, N_1 - 1, \quad \Delta\xi_1 = 1/(N_1 - 1), \\ (\xi_2)_j &= j\Delta\xi_2, \quad j = 0, 1, \dots, N_2 - 1, \quad \Delta\xi_2 = 1/(N_2 - 1). \end{aligned}$$

Define the cell $I_{i,j} := [(\xi_1)_{i-\frac{1}{2}}, (\xi_1)_{i+\frac{1}{2}}] \times [(\xi_2)_{j-\frac{1}{2}}, (\xi_2)_{j+\frac{1}{2}}]$.

Our semi-discrete finite volume schemes for (8) and the GCLs (6) are given by

$$\begin{aligned} \frac{d(\overline{JU})_{i,j}}{dt} &= -\frac{1}{\Delta\xi_1} \left((\widetilde{\mathcal{F}}_1)_{i+\frac{1}{2},j} - (\widetilde{\mathcal{F}}_1)_{i-\frac{1}{2},j} \right) + \frac{1}{\Delta\xi_1} \sum_{m=1}^2 (\overline{s}_m)_{i,j} \left((\widetilde{\mathcal{R}}_{m1})_{i+\frac{1}{2},j} - (\widetilde{\mathcal{R}}_{m1})_{i-\frac{1}{2},j} \right) \\ &\quad - \frac{1}{\Delta\xi_2} \left((\widetilde{\mathcal{F}}_2)_{i,j+\frac{1}{2}} - (\widetilde{\mathcal{F}}_2)_{i,j-\frac{1}{2}} \right) + \frac{1}{\Delta\xi_2} \sum_{m=1}^2 (\overline{s}_m)_{i,j} \left((\widetilde{\mathcal{R}}_{m2})_{i,j+\frac{1}{2}} - (\widetilde{\mathcal{R}}_{m2})_{i,j-\frac{1}{2}} \right) \\ &\quad + \frac{1}{\Delta\xi_1 \Delta\xi_2} \int_{I_{i,j}} \sum_{m=1}^2 (s_m - (\overline{s}_m)_{i,j}) \nabla_{\xi} \cdot \mathcal{R}_m, \end{aligned} \quad (33)$$

$$\frac{d\overline{J}_{i,j}}{dt} = -\frac{1}{\Delta\xi_1} \left(\left(J \frac{\partial \xi_1}{\partial t} \right)_{i+\frac{1}{2},j} - \left(J \frac{\partial \xi_1}{\partial t} \right)_{i-\frac{1}{2},j} \right) - \frac{1}{\Delta\xi_2} \left(\left(J \frac{\partial \xi_2}{\partial t} \right)_{i,j+\frac{1}{2}} - \left(J \frac{\partial \xi_2}{\partial t} \right)_{i,j-\frac{1}{2}} \right), \quad (34)$$

$$\frac{1}{\Delta\xi_1} \left(\left(J \frac{\partial \xi_1}{\partial x_1} \right)_{i+\frac{1}{2},j} - \left(J \frac{\partial \xi_1}{\partial x_1} \right)_{i-\frac{1}{2},j} \right) + \frac{1}{\Delta\xi_2} \left(\left(J \frac{\partial \xi_2}{\partial x_1} \right)_{i,j+\frac{1}{2}} - \left(J \frac{\partial \xi_2}{\partial x_1} \right)_{i,j-\frac{1}{2}} \right) = 0, \quad (35)$$

$$\frac{1}{\Delta\xi_1} \left(\left(J \frac{\partial \xi_1}{\partial x_2} \right)_{i+\frac{1}{2},j} - \left(J \frac{\partial \xi_1}{\partial x_2} \right)_{i-\frac{1}{2},j} \right) + \frac{1}{\Delta\xi_2} \left(\left(J \frac{\partial \xi_2}{\partial x_2} \right)_{i,j+\frac{1}{2}} - \left(J \frac{\partial \xi_2}{\partial x_2} \right)_{i,j-\frac{1}{2}} \right) = 0, \quad (36)$$

where

$$(\widetilde{\mathcal{F}}_1)_{i\pm\frac{1}{2},j} = \sum_{\mu=1}^Q \omega_{\mu} \left[\left(J \frac{\partial \xi_1}{\partial t} \right)_{i\pm\frac{1}{2},j}^{\mu} \llbracket \mathbf{U} \rrbracket_{i\pm\frac{1}{2},j}^{\mu} - \frac{\alpha_1}{2} \llbracket \mathbf{U} \rrbracket_{i\pm\frac{1}{2},j}^{\mu} + (L_1)_{i\pm\frac{1}{2},j}^{\mu} (\widetilde{\mathbf{F}}_{n_1})_{i\pm\frac{1}{2},j}^{\mu} \right], \quad (37)$$

$$(\widetilde{\mathcal{F}}_2)_{i,j\pm\frac{1}{2}} = \sum_{\mu=1}^Q \omega_{\mu} \left[\left(J \frac{\partial \xi_2}{\partial t} \right)_{i,j\pm\frac{1}{2}}^{\mu} \llbracket \mathbf{U} \rrbracket_{i,j\pm\frac{1}{2}}^{\mu} - \frac{\alpha_2}{2} \llbracket \mathbf{U} \rrbracket_{i,j\pm\frac{1}{2}}^{\mu} + (L_2)_{i,j\pm\frac{1}{2}}^{\mu} (\widetilde{\mathbf{F}}_{n_2})_{i,j\pm\frac{1}{2}}^{\mu} \right], \quad (38)$$

$$\left(J \frac{\partial \xi_1}{\partial t} \right)_{i\pm\frac{1}{2},j}^{\mu} = \left(J \frac{\partial \xi_1}{\partial t} \right)_{i\pm\frac{1}{2},j}^{\mu} - \frac{(\beta_1)_J}{2} \llbracket J \rrbracket_{i\pm\frac{1}{2},j}^{\mu}, \quad \left(J \frac{\partial \xi_2}{\partial t} \right)_{i,j\pm\frac{1}{2}}^{\mu} = \left(J \frac{\partial \xi_2}{\partial t} \right)_{i,j\pm\frac{1}{2}}^{\mu} - \frac{(\beta_2)_J}{2} \llbracket J \rrbracket_{i,j\pm\frac{1}{2}}^{\mu}, \quad (39)$$

$$\left(J \frac{\partial \xi_1}{\partial t} \right)_{i \pm \frac{1}{2}, j} = \sum_{\mu=1}^Q \omega_{\mu} \left(J \frac{\partial \xi_1}{\partial t} \right)_{i \pm \frac{1}{2}, j}^{\mu}, \quad \left(J \frac{\partial \xi_2}{\partial t} \right)_{i, j \pm \frac{1}{2}} = \sum_{\mu=1}^Q \omega_{\mu} \left(J \frac{\partial \xi_2}{\partial t} \right)_{i, j \pm \frac{1}{2}}^{\mu}, \quad (40)$$

$$\left(J \frac{\partial \xi_1}{\partial x_k} \right)_{i \pm \frac{1}{2}, j} = \sum_{\mu=1}^Q \omega_{\mu} \left(J \frac{\partial \xi_1}{\partial x_k} \right)_{i \pm \frac{1}{2}, j}^{\mu}, \quad \left(J \frac{\partial \xi_2}{\partial x_k} \right)_{i, j \pm \frac{1}{2}} = \sum_{\mu=1}^Q \omega_{\mu} \left(J \frac{\partial \xi_2}{\partial x_k} \right)_{i, j \pm \frac{1}{2}}^{\mu}, \quad (41)$$

$$(\tilde{\mathcal{R}}_{m1})_{i \pm \frac{1}{2}, j} = \sum_{\mu=1}^Q \omega_{\mu} \left[(L_1)_{i \pm \frac{1}{2}, j}^{\mu} (\tilde{\mathbf{r}}_m)_{n1}^{\mu} \right], \quad (42)$$

$$(\tilde{\mathcal{R}}_{m2})_{i, j \pm \frac{1}{2}} = \sum_{\mu=1}^Q \omega_{\mu} \left[(L_2)_{i, j \pm \frac{1}{2}}^{\mu} (\tilde{\mathbf{r}}_m)_{n2}^{\mu} \right]. \quad (43)$$

Here, $(\cdot)_{i \pm \frac{1}{2}, j}^{\mu}$ and $(\cdot)_{i, j \pm \frac{1}{2}}^{\mu}$ represent the approximations at the quadrature points $((\xi_1)_{i \pm \frac{1}{2}}, (\xi_2)_{j_{\mu}})$ and $((\xi_1)_{i_{\mu}}, (\xi_2)_{j \pm \frac{1}{2}})$, respectively, with the corresponding quadrature weights denoted as $\{\omega_{\mu}\}_{\mu=1}^Q$. The procedures of obtaining $\mathbf{U}_{i \pm \frac{1}{2}, j}^{\pm, \mu}$ and $\mathbf{U}_{i, j \pm \frac{1}{2}}^{\pm, \mu}$ will be given in Subsections 4.3. The parameters $\alpha_1, \alpha_2, (\beta_1)_J$ and $(\beta_2)_J$ in (37), (38) and (39) are defined as

$$\alpha_1 = \max_{i, j, \mu} \left\{ \left\| \left(J \frac{\partial \xi_1}{\partial t} \right)_{i \pm \frac{1}{2}, j}^{\mu} \right\| \right\}, \quad \alpha_2 = \max_{i, j, \mu} \left\{ \left\| \left(J \frac{\partial \xi_2}{\partial t} \right)_{i, j \pm \frac{1}{2}}^{\mu} \right\| \right\}, \quad (44)$$

$$(\beta_1)_J = \max_{i, j, \mu} \left\{ \left\| \left(J \frac{\partial \xi_1}{\partial t} / J \right)_{i \pm \frac{1}{2}, j}^{\mu} \right\| \right\}, \quad (\beta_2)_J = \max_{i, j, \mu} \left\{ \left\| \left(J \frac{\partial \xi_2}{\partial t} / J \right)_{i, j \pm \frac{1}{2}}^{\mu} \right\| \right\}.$$

The computations of $\left(J \frac{\partial \xi_{\ell}}{\partial t} \right)_{i \pm \frac{1}{2}, j}^{\mu}$, $\left(J \frac{\partial \xi_{\ell}}{\partial t} \right)_{i, j \pm \frac{1}{2}}^{\mu}$, $\left(J \frac{\partial \xi_{\ell}}{\partial x_k} \right)_{i \pm \frac{1}{2}, j}^{\mu}$, and $\left(J \frac{\partial \xi_{\ell}}{\partial x_k} \right)_{i, j \pm \frac{1}{2}}^{\mu}$ will be given in Section 4.2.

The integral term in (33) should be approximated by a proper quadrature rule on $I_{i, j}$:

$$\frac{1}{\Delta \xi_1 \Delta \xi_2} \int_{I_{i, j}} \sum_{m=1}^2 (s_m - (\bar{s}_m)_{i, j}) \nabla_{\xi} \cdot \mathcal{R}_m \approx \sum_{\mu, \nu=1}^Q \omega_{\mu, \nu} \sum_{m=1}^2 ((s_m)_{i_{\mu}, j_{\nu}} - (\bar{s}_m)_{i, j}) [\nabla_{\xi} \cdot \mathcal{R}_m]_{i_{\mu}, j_{\nu}}, \quad (45)$$

where $(\cdot)_{i_{\mu}, j_{\nu}}$ denotes the approximate values at the quadrature point $((\xi_1)_{i_{\mu}}, (\xi_2)_{j_{\nu}})$, and $\{\omega_{\mu, \nu}\}$ denote the corresponding quadrature weights. For the WB consideration, the numerical fluxes $(\tilde{\mathbf{F}}_{n1})_{i \pm \frac{1}{2}, j}^{\mu}$ and $(\tilde{\mathcal{R}}_{m1})_{i \pm \frac{1}{2}, j}$ in equations (38) and (42) can be defined based on the hydrostatic reconstruction [1] as

$$(\tilde{\mathbf{F}}_{n1})_{i \pm \frac{1}{2}, j}^{\mu} = (\tilde{\mathbf{F}}_{n1})_{i \pm \frac{1}{2}, j}^{L, \mu} = \langle (\mathbf{n}_1)_{i \pm \frac{1}{2}, j}^{\mu}, \tilde{\mathbf{F}}_{i \pm \frac{1}{2}, j}^{L, \mu} \rangle - \frac{\beta}{2} (\mathbf{U}_{i \pm \frac{1}{2}, j}^{+, \mu, *} - \mathbf{U}_{i \pm \frac{1}{2}, j}^{-, \mu, *}),$$

$$(\tilde{\mathcal{R}}_{m1})_{i \pm \frac{1}{2}, j} = \sum_{\mu=1}^Q \omega_{\mu} \left[(L_1)_{i \pm \frac{1}{2}, j}^{\mu} (\tilde{\mathbf{r}}_m)_{n1}^{\mu} \right],$$

$$(\tilde{\mathbf{r}}_m)_{n1}^{\mu} = \langle (\mathbf{n}_1)_{i \pm \frac{1}{2}, j}^{\mu}, (\mathbf{r}_m)_{i \pm \frac{1}{2}, j}^{-, \mu} \rangle,$$

with

$$(\widetilde{\mathbf{F}})_{i+\frac{1}{2},j}^{L,\mu} = \left((\widetilde{\mathbf{F}}_1)_{i+\frac{1}{2},j}^{L,\mu}, (\widetilde{\mathbf{F}}_2)_{i+\frac{1}{2},j}^{L,\mu} \right)^\top, \quad \beta = \max_{i,j} \left(|\bar{v}_{i,j}| + \sqrt{g\bar{h}_{i,j}} \right),$$

where

$$\begin{aligned} (\widetilde{\mathbf{F}}_1)_{i+\frac{1}{2},j}^{L,\mu} &= \frac{1}{2} \left(\mathbf{F}_1(\mathbf{U}_{i+\frac{1}{2},j}^{-,\mu,*}) + \mathbf{F}_1(\mathbf{U}_{i+\frac{1}{2},j}^{+,\mu,*}) \right) + \begin{pmatrix} 0 \\ \frac{g}{2} \left(h_{i+\frac{1}{2},j}^{-,\mu} \right)^2 - \frac{g}{2} \left(h_{i+\frac{1}{2},j}^{-,\mu,*} \right)^2 \\ 0 \end{pmatrix}, \\ (\widetilde{\mathbf{F}}_2)_{i+\frac{1}{2},j}^{L,\mu} &= \frac{1}{2} \left(\mathbf{F}_2(\mathbf{U}_{i+\frac{1}{2},j}^{-,\mu,*}) + \mathbf{F}_2(\mathbf{U}_{i+\frac{1}{2},j}^{+,\mu,*}) \right) + \begin{pmatrix} 0 \\ 0 \\ \frac{g}{2} \left(h_{i+\frac{1}{2},j}^{-,\mu} \right)^2 - \frac{g}{2} \left(h_{i+\frac{1}{2},j}^{-,\mu,*} \right)^2 \end{pmatrix}, \\ \mathbf{U}_{i+\frac{1}{2},j}^{\pm,\mu,*} &= \begin{pmatrix} h_{i+\frac{1}{2},j}^{\pm,\mu,*} \\ h_{i+\frac{1}{2},j}^{\pm,\mu,*}(v_1)_{i+\frac{1}{2},j}^{\pm,\mu} \\ h_{i+\frac{1}{2},j}^{\pm,\mu,*}(v_2)_{i+\frac{1}{2},j}^{\pm,\mu} \end{pmatrix}, \quad h_{i+\frac{1}{2},j}^{\pm,\mu,*} = \max \left(0, h_{i+\frac{1}{2},j}^{\pm,\mu} + b_{i+\frac{1}{2},j}^{\pm,\mu} - \max \left(b_{i+\frac{1}{2},j}^{+,\mu}, b_{i+\frac{1}{2},j}^{-,\mu} \right) \right). \end{aligned}$$

The numerical fluxes in (37)-(43) maintain

$$\begin{aligned} (\widetilde{\mathbf{F}}_{n_1})_{i\pm\frac{1}{2},j}^\mu - \sum_{m=1}^2 (\bar{s}_m)_{i,j} (\widetilde{\mathbf{r}}_m)_{i\pm\frac{1}{2},j}^\mu &= \langle (\mathbf{n}_1)_{i\pm\frac{1}{2},j}^\mu, \mathbf{C} \rangle, \\ (\widetilde{\mathbf{F}}_{n_2})_{i,j\pm\frac{1}{2}}^\mu - \sum_{m=1}^2 (\bar{s}_m)_{i,j} (\widetilde{\mathbf{r}}_m)_{i,j\pm\frac{1}{2}}^\mu &= \langle (\mathbf{n}_2)_{i,j\pm\frac{1}{2}}^\mu, \mathbf{C} \rangle, \end{aligned} \tag{46}$$

when a steady state is reached. [Appendix A](#) details the fluxes $(\widetilde{\mathbf{F}}_{n_1})_{i-\frac{1}{2},j}^\mu$, $(\widetilde{\mathbf{R}}_{m1})_{i-\frac{1}{2},j}$, $(\widetilde{\mathbf{F}}_{n_2})_{i,j\pm\frac{1}{2}}^\mu$, $(\widetilde{\mathbf{R}}_{m2})_{i,j\pm\frac{1}{2}}$ and the proof for the condition (46). As discussed in [Section 2.2](#), the governing equations of \mathbf{w} and \mathbf{q} have been expressed as

$$\frac{\partial J\mathbf{w}}{\partial t} + \sum_{\ell=1}^2 \frac{\partial}{\partial \xi_\ell} \left(J \frac{\partial \xi_\ell}{\partial t} \mathbf{w} \right) = 0, \quad \frac{\partial J\mathbf{q}}{\partial t} + \sum_{\ell=1}^2 \frac{\partial}{\partial \xi_\ell} \left(J \frac{\partial \xi_\ell}{\partial t} \mathbf{q} \right) = 0.$$

Our semi-discrete schemes for $J\mathbf{w}$ and $J\mathbf{q}$ are given by

$$\frac{d(\overline{J\mathbf{w}})_{i,j}}{dt} = -\frac{1}{\Delta \xi_1} \left(\widetilde{\mathbf{w}}_{i+\frac{1}{2},j} - \widetilde{\mathbf{w}}_{i-\frac{1}{2},j} \right) - \frac{1}{\Delta \xi_2} \left(\widetilde{\mathbf{w}}_{i,j+\frac{1}{2}} - \widetilde{\mathbf{w}}_{i,j-\frac{1}{2}} \right), \tag{47}$$

$$\frac{d(\overline{J\mathbf{q}})_{i,j}}{dt} = -\frac{1}{\Delta \xi_1} \left(\widetilde{\mathbf{q}}_{i+\frac{1}{2},j} - \widetilde{\mathbf{q}}_{i-\frac{1}{2},j} \right) - \frac{1}{\Delta \xi_2} \left(\widetilde{\mathbf{q}}_{i,j+\frac{1}{2}} - \widetilde{\mathbf{q}}_{i,j-\frac{1}{2}} \right), \tag{48}$$

with

$$\begin{aligned}
\widetilde{w}_{i\pm\frac{1}{2},j} &= \sum_{\mu=1}^Q \omega_{\mu} \left[\left(J \frac{\partial \xi}{\partial t} \right)_{i\pm\frac{1}{2},j}^{\mu} \llbracket \mathbf{w} \rrbracket_{i\pm\frac{1}{2},j}^{\mu} - \frac{\alpha_1}{2} \llbracket \mathbf{w} \rrbracket_{i\pm\frac{1}{2},j}^{\mu} \right], \\
\widetilde{w}_{i,j\pm\frac{1}{2}} &= \sum_{\mu=1}^Q \omega_{\mu} \left[\left(J \frac{\partial \xi}{\partial t} \right)_{i,j\pm\frac{1}{2}}^{\mu} \llbracket \mathbf{w} \rrbracket_{i,j\pm\frac{1}{2}}^{\mu} - \frac{\alpha_2}{2} \llbracket \mathbf{w} \rrbracket_{i,j\pm\frac{1}{2}}^{\mu} \right], \\
\widetilde{q}_{i\pm\frac{1}{2},j} &= \sum_{\mu=1}^Q \omega_{\mu} \left[\left(J \frac{\partial \xi}{\partial t} \right)_{i\pm\frac{1}{2},j}^{\mu} \llbracket \mathbf{q} \rrbracket_{i\pm\frac{1}{2},j}^{\mu} - \frac{\alpha_1}{2} \llbracket \mathbf{q} \rrbracket_{i\pm\frac{1}{2},j}^{\mu} \right], \\
\widetilde{q}_{i,j\pm\frac{1}{2}} &= \sum_{\mu=1}^Q \omega_{\mu} \left[\left(J \frac{\partial \xi}{\partial t} \right)_{i,j\pm\frac{1}{2}}^{\mu} \llbracket \mathbf{q} \rrbracket_{i,j\pm\frac{1}{2}}^{\mu} - \frac{\alpha_2}{2} \llbracket \mathbf{q} \rrbracket_{i,j\pm\frac{1}{2}}^{\mu} \right].
\end{aligned} \tag{49}$$

The cell averages of \mathbf{U} , \mathbf{w} , and \mathbf{q} in the physical domain are then computed by

$$\overline{U}_{i,j} := \frac{\overline{JU}_{i,j}}{\overline{J}_{i,j}} = \frac{\int_{I_{i,j}} JU d\xi}{\int_{I_{i,j}} J d\xi}, \quad \overline{w}_{i,j} := \frac{\overline{Jw}_{i,j}}{\overline{J}_{i,j}} = \frac{\int_{I_{i,j}} Jw d\xi}{\int_{I_{i,j}} J d\xi}, \quad \overline{q}_{i,j} := \frac{\overline{Jq}_{i,j}}{\overline{J}_{i,j}} = \frac{\int_{I_{i,j}} Jq d\xi}{\int_{I_{i,j}} J d\xi}.$$

One can use the numerical quadrature rules to calculate the integral above.

4.2. Discretization of mesh metrics

This subsection first details the computations of $\left\{ \left(J \frac{\partial \xi_{\ell}}{\partial x_k} \right)_{i_{\mu}, j_{\nu}} \right\}$ at the quadrature points $\{((\xi_1)_{i_{\mu}}, (\xi_2)_{j_{\nu}})\}$

for the calculations in (45). We then give the high-order approximations of $\left(J \frac{\partial \xi_{\ell}}{\partial t} \right)_{i\pm\frac{1}{2},j}^{\mu}$, $\left(J \frac{\partial \xi_{\ell}}{\partial t} \right)_{i,j\pm\frac{1}{2}}^{\mu}$, $\left(J \frac{\partial \xi_{\ell}}{\partial x_k} \right)_{i\pm\frac{1}{2},j}^{\mu}$, and $\left(J \frac{\partial \xi_{\ell}}{\partial x_k} \right)_{i,j\pm\frac{1}{2}}^{\mu}$ at the quadrature points $((\xi_1)_{i\pm\frac{1}{2}}, (\xi_2)_{j_{\mu}})$ and $((\xi_1)_{i_{\mu}}, (\xi_2)_{j\pm\frac{1}{2}})$.

The high-order approximation for the mesh metrics satisfying the discrete version of the SCLs can be constructed by using the method proposed in [39]. Note that the mesh metrics satisfy the following relations

$$\begin{aligned}
J \frac{\partial \xi_1}{\partial x_1} &= \frac{\partial x_2}{\partial \xi_2}, & J \frac{\partial \xi_1}{\partial x_2} &= -\frac{\partial x_1}{\partial \xi_2}, \\
J \frac{\partial \xi_2}{\partial x_1} &= -\frac{\partial x_2}{\partial \xi_1}, & J \frac{\partial \xi_2}{\partial x_2} &= \frac{\partial x_1}{\partial \xi_1}.
\end{aligned} \tag{50}$$

The values $\left(J \frac{\partial \xi_{\ell}}{\partial x_k} \right)_{i_{\mu}, j_{\nu}}$ can be obtained by using the polynomial interpolation based on the mesh point \mathbf{x} . Take the fifth-order approximation to $\left(J \frac{\partial \xi_1}{\partial x_1} \right)_{i_{\mu}, j_{\nu}}$ as an example. Notice that the $J \frac{\partial \xi_1}{\partial x_1} = \frac{\partial x_2}{\partial \xi_2}$. If one has a sixth-order approximation $\widehat{x}_2(\xi)$ to $x_2(\xi)$ on the cell $I_{i,j}$, then $\left(J \frac{\partial \xi_1}{\partial x_1} \right)_{i_{\mu}, j_{\nu}}$ can be evaluated by $\frac{\partial \widehat{x}_2}{\partial \xi_2}((\xi_1)_{i_{\mu}}, (\xi_2)_{j_{\nu}})$. To obtain the values $\frac{\partial \widehat{x}_2}{\partial \xi_2}((\xi_1)_{i_{\mu}}, (\xi_2)_{j_{\nu}})$, we use the dimension-by-dimension approach. Let \mathbb{P}^5 denote the space of 1D polynomials of degree up to five. One

can derive the polynomial $\widehat{x}_2(\xi_1)|_{\mathcal{E}_{i,j+\frac{1}{2}}} \in \mathbb{P}^5$ at the edge $\mathcal{E}_{i,j+\frac{1}{2}}$ connecting $\left((x_1)_{i-\frac{1}{2},j+\frac{1}{2}}, (x_2)_{i-\frac{1}{2},j+\frac{1}{2}}\right)$ and $\left((x_1)_{i+\frac{1}{2},j+\frac{1}{2}}, (x_2)_{i+\frac{1}{2},j+\frac{1}{2}}\right)$ by using a 1D polynomial interpolation. This gives the point values $\widehat{x}_2((\xi_1)_{i_\mu,j+\frac{1}{2}})|_{\mathcal{E}_{i,j+\frac{1}{2}}}$ at $(\xi_1)_{i_\mu,j+\frac{1}{2}}$. We interpolate these values $\left\{\widehat{x}_2((\xi_1)_{i_\mu,j+\frac{1}{2}})|_{\mathcal{E}_{i,j+\frac{1}{2}}}\right\}$ to obtain $\widehat{x}_2(\xi_2)|_{\mathcal{E}_{i_\mu,j}} \in \mathbb{P}^5$ at the edge $\mathcal{E}_{i_\mu,j}$ connecting $\left((x_1)_{i_\mu,j-\frac{1}{2}}, (x_2)_{i_\mu,j-\frac{1}{2}}\right)$ and $\left((x_1)_{i_\mu,j+\frac{1}{2}}, (x_2)_{i_\mu,j+\frac{1}{2}}\right)$, which gives the point values $\frac{\partial \widehat{x}_2}{\partial \xi_2}((\xi_2)_{j_r})|_{\mathcal{E}_{i_\mu,j}}$. Specifically, the 1D polynomial $\widehat{x}_2(\xi_1)|_{\mathcal{E}_{i,j+\frac{1}{2}}}$ can be obtained by using the stencil $\left\{(x_2)_{i\pm\frac{r}{2},j+\frac{1}{2}}\right\}_{r=1}^3$. Assume that $\widehat{x}_2(\xi_1)|_{\mathcal{E}_{i,j+\frac{1}{2}}}$ has the following form

$$\begin{aligned} x_2(\xi_1)|_{\mathcal{E}_{i,j+\frac{1}{2}}} &= a_0 \left(\xi_1 - (\xi_1)_{i,j+\frac{1}{2}}\right)^5 + a_1 \left(\xi_1 - (\xi_1)_{i,j+\frac{1}{2}}\right)^4 + a_2 \left(\xi_1 - (\xi_1)_{i,j+\frac{1}{2}}\right)^3 \\ &\quad + a_3 \left(\xi_1 - (\xi_1)_{i,j+\frac{1}{2}}\right)^2 + a_4 \left(\xi_1 - (\xi_1)_{i,j+\frac{1}{2}}\right) + a_5. \end{aligned}$$

Using the interpolation condition $\widehat{x}_2((\xi_1)_{i\pm\frac{r}{2},j+\frac{1}{2}})|_{\mathcal{E}_{i,j+\frac{1}{2}}} = (x_2)_{i\pm\frac{r}{2},j+\frac{1}{2}}$, $r = 1, 2, 3$, and solving the system of the linear equations, we obtain the coefficients

$$\begin{aligned} a_0 &= -(10(x_2)_{i-\frac{1}{2},j+\frac{1}{2}} - 5(x_2)_{i-\frac{3}{2},j+\frac{1}{2}} + (x_2)_{i-\frac{5}{2},j+\frac{1}{2}} - 10(x_2)_{i+\frac{1}{2},j+\frac{1}{2}} + 5(x_2)_{i+\frac{3}{2},j+\frac{1}{2}} \\ &\quad - (x_2)_{i+\frac{5}{2},j+\frac{1}{2}})/(120(\Delta\xi_1)^5), \\ a_1 &= (2(x_2)_{i-\frac{1}{2},j+\frac{1}{2}} - 3(x_2)_{i-\frac{3}{2},j+\frac{1}{2}} + (x_2)_{i-\frac{5}{2},j+\frac{1}{2}} + 2(x_2)_{i+\frac{1}{2},j+\frac{1}{2}} - 3(x_2)_{i+\frac{3}{2},j+\frac{1}{2}} \\ &\quad + (x_2)_{i+\frac{5}{2},j+\frac{1}{2}})/(48(\Delta\xi_1)^4), \\ a_2 &= (34(x_2)_{i-\frac{1}{2},j+\frac{1}{2}} - 13(x_2)_{i-\frac{3}{2},j+\frac{1}{2}} + (x_2)_{i-\frac{5}{2},j+\frac{1}{2}} - 34(x_2)_{i+\frac{1}{2},j+\frac{1}{2}} + 13(x_2)_{i+\frac{3}{2},j+\frac{1}{2}} \\ &\quad - (x_2)_{i+\frac{5}{2},j+\frac{1}{2}})/(48(\Delta\xi_1)^3), \\ a_3 &= -(34(x_2)_{i-\frac{1}{2},j+\frac{1}{2}} - 39(x_2)_{i-\frac{3}{2},j+\frac{1}{2}} + 5(x_2)_{i-\frac{5}{2},j+\frac{1}{2}} + 34(x_2)_{i+\frac{1}{2},j+\frac{1}{2}} - 39(x_2)_{i+\frac{3}{2},j+\frac{1}{2}} \\ &\quad + 5(x_2)_{i+\frac{5}{2},j+\frac{1}{2}})/(96(\Delta\xi_1)^2), \\ a_4 &= -(2250(x_2)_{i-\frac{1}{2},j+\frac{1}{2}} - 125(x_2)_{i-\frac{3}{2},j+\frac{1}{2}} + 9(x_2)_{i-\frac{5}{2},j+\frac{1}{2}} - 2250(x_2)_{i+\frac{1}{2},j+\frac{1}{2}} + 125(x_2)_{i+\frac{3}{2},j+\frac{1}{2}} \\ &\quad - 9(x_2)_{i+\frac{5}{2},j+\frac{1}{2}})/1920(\Delta\xi_1), \\ a_5 &= (75(x_2)_{i-\frac{1}{2},j+\frac{1}{2}})/128 - (25(x_2)_{i-\frac{3}{2},j+\frac{1}{2}})/256 + (3(x_2)_{i-\frac{5}{2},j+\frac{1}{2}})/256 + (75(x_2)_{i+\frac{1}{2},j+\frac{1}{2}})/128 \\ &\quad - (25(x_2)_{i+\frac{3}{2},j+\frac{1}{2}})/256 + (3(x_2)_{i+\frac{5}{2},j+\frac{1}{2}})/256. \end{aligned}$$

It follows that $(x_2)_{i_\mu,j+\frac{1}{2}} = \widehat{x}_2((\xi_1)_{i_\mu,j+\frac{1}{2}})$ at the edge $\mathcal{E}_{i,j+\frac{1}{2}}$. The 1D polynomial $\widehat{x}_2(\xi_2)|_{\mathcal{E}_{i_\mu,j}}$ can be obtained by using the stencil $\left\{(x_2)_{i_\mu,j\pm\frac{r}{2}}\right\}_{r=1}^3$ in a similar way. Assume the polynomials can be represented as

$$\begin{aligned} \widehat{x}_2(\xi_2)|_{\mathcal{E}_{i_\mu,j}} &= \widetilde{a}_0 \left(\xi_2 - (\xi_2)_{i_\mu,j}\right)^5 + \widetilde{a}_1 \left(\xi_2 - (\xi_2)_{i_\mu,j}\right)^4 + \widetilde{a}_2 \left(\xi_2 - (\xi_2)_{i_\mu,j}\right)^3 \\ &\quad + \widetilde{a}_3 \left(\xi_2 - (\xi_2)_{i_\mu,j}\right)^2 + \widetilde{a}_4 \left(\xi_2 - (\xi_2)_{i_\mu,j}\right) + \widetilde{a}_5. \end{aligned}$$

Based on the interpolation conditions $\widehat{x_2}((\xi_2)_{i_\mu, j+\frac{r}{2}})|_{\mathcal{E}_{i_\mu, j}} = (x_2)_{i_\mu, j+\frac{r}{2}}$, the coefficients are computed as

$$\begin{aligned}
\widetilde{a}_0 &= -(10(x_2)_{i_\mu, j-\frac{1}{2}} - 5(x_2)_{i_\mu, j-\frac{3}{2}} + (x_2)_{i_\mu, j-\frac{5}{2}} - 10(x_2)_{i_\mu, j+\frac{1}{2}} + 5(x_2)_{i_\mu, j+\frac{3}{2}} \\
&\quad - (x_2)_{i_\mu, j+\frac{5}{2}})/(120(\Delta\xi_1)^5), \\
\widetilde{a}_1 &= (2(x_2)_{i_\mu, j-\frac{1}{2}} - 3(x_2)_{i_\mu, j-\frac{3}{2}} + (x_2)_{i_\mu, j-\frac{5}{2}} + 2(x_2)_{i_\mu, j+\frac{1}{2}} - 3(x_2)_{i_\mu, j+\frac{3}{2}} \\
&\quad + (x_2)_{i_\mu, j+\frac{5}{2}})/(48(\Delta\xi_1)^4), \\
\widetilde{a}_2 &= (34(x_2)_{i_\mu, j-\frac{1}{2}} - 13(x_2)_{i_\mu, j-\frac{3}{2}} + (x_2)_{i_\mu, j-\frac{5}{2}} - 34(x_2)_{i_\mu, j+\frac{1}{2}} + 13(x_2)_{i_\mu, j+\frac{3}{2}} \\
&\quad - (x_2)_{i_\mu, j+\frac{5}{2}})/(48(\Delta\xi_1)^3), \\
\widetilde{a}_3 &= -(34(x_2)_{i_\mu, j-\frac{1}{2}} - 39(x_2)_{i_\mu, j-\frac{3}{2}} + 5(x_2)_{i_\mu, j-\frac{5}{2}} + 34(x_2)_{i_\mu, j+\frac{1}{2}} - 39(x_2)_{i_\mu, j+\frac{3}{2}} \\
&\quad + 5(x_2)_{i_\mu, j+\frac{5}{2}})/(96(\Delta\xi_1)^2), \\
\widetilde{a}_4 &= -(2250(x_2)_{i_\mu, j-\frac{1}{2}} - 125(x_2)_{i_\mu, j-\frac{3}{2}} + 9(x_2)_{i_\mu, j-\frac{5}{2}} - 2250(x_2)_{i_\mu, j+\frac{1}{2}} + 125(x_2)_{i_\mu, j+\frac{3}{2}} \\
&\quad - 9(x_2)_{i_\mu, j+\frac{5}{2}})/1920(\Delta\xi_1), \\
\widetilde{a}_5 &= (75(x_2)_{i_\mu, j-\frac{1}{2}})/128 - (25(x_2)_{i_\mu, j-\frac{3}{2}})/256 + (3(x_2)_{i_\mu, j-\frac{5}{2}})/256 + (75(x_2)_{i_\mu, j+\frac{1}{2}})/128 \\
&\quad - (25(x_2)_{i_\mu, j+\frac{3}{2}})/256 + (3(x_2)_{i_\mu, j+\frac{5}{2}})/256.
\end{aligned}$$

Using the relations (50) gives $\left(J\frac{\partial\xi_1}{\partial x_1}\right)_{i_\mu, j_\nu} = \frac{\partial\widehat{x_2}}{\partial\xi_2}((\xi_2)_{j_\nu})|_{\mathcal{E}_{i_\mu, j}}$. Similarly, we can obtain the mesh metrics $\left(J\frac{\partial\xi_\ell}{\partial x_k}\right)_{i_\mu, j_\nu}^\mu$ and $\left(J\frac{\partial\xi_\ell}{\partial x_k}\right)_{i_\mu, j_\nu}^\mu$ in (41). As illustrated in [39], such approximations maintain the discrete SCLs.

Based on the relation

$$J\frac{\partial\xi_\ell}{\partial t} = -\sum_{k=1}^2\left(\frac{\partial x_k}{\partial t}\right)\left(J\frac{\partial\xi_\ell}{\partial x_k}\right),$$

the values of the temporal metric at the quadrature points can be evaluated by

$$\left(\widehat{J\frac{\partial\xi_k}{\partial t}}\right)_{i_\mu, j_\nu} = -\sum_{\ell=1}^d\left[\left(\frac{\partial x_\ell}{\partial t}\right)\left(J\frac{\partial\xi_k}{\partial x_\ell}\right)\right]_{i_\mu, j_\nu}, \quad (51)$$

where $\left(\frac{\partial x_\ell}{\partial t}\right)_{i_\mu, j_\nu}$ is the mesh velocity determined by the adaptive moving mesh strategy detailed in Section 5.

4.3. High-order 2D reconstruction

This section discusses the 2D WENO reconstruction in the computational domain. For the computations in (45), the high-order approximate values of \mathbf{U} at $\{(\xi_1)_{i_\mu}, (\xi_2)_{j_\nu}\}$ are required.

These values are obtained by generalizing the 1D reconstruction approach in Subsection 3.2 to the 2D case in a dimension-by-dimension fashion.

Step 1. Starting from the cell average values $\overline{JU}_{i,j}$ and $\overline{J}_{i,j}$, we apply the 1D WENO reconstruction to obtain the edge average values $\{\overline{JU}_{i\mu,j}\}$ and $\{\overline{J}_{i\mu,j}\}$. For example, we perform

$$\{\overline{JU}_{i,j}\} \xrightarrow{\text{WENO}} \{\overline{JU}_{i\mu,j}\} \text{ for fixed } j, \quad \{\overline{J}_{i,j}\} \xrightarrow{\text{WENO}} \{\overline{J}_{i\mu,j}\} \text{ for fixed } j.$$

Step 2. Based on the edge values $\{\overline{JU}_{i\mu,j}\}$ and $\{\overline{J}_{i\mu,j}\}$, we perform the 1D WENO reconstruction along the other direction to get the point values $\mathring{JU}_{i\mu,j\nu}$, and $\mathring{J}_{i\mu,j\nu}$, i.e.,

$$\{\overline{JU}_{i\mu,j}\} \xrightarrow{\text{WENO}} \{\mathring{JU}_{i\mu,j\nu}\}, \quad \{\overline{J}_{i\mu,j}\} \xrightarrow{\text{WENO}} \{\mathring{J}_{i\mu,j\nu}\} \text{ for fixed } i.$$

Then $\mathring{U}_{i\mu,j\nu} = \mathring{JU}_{i\mu,j\nu} / \mathring{J}_{i\mu,j\nu}$. To ensure the cell average of J , we modify $J_{i\mu,j\nu} = \overline{J}_i - \sum_{\mu,\nu} \omega_{\mu,\nu} \mathring{J}_{i\mu,j\nu}$ to obtain $\sum_{\mu,\nu} \omega_{\mu,\nu} J_{i\mu,j\nu} = \overline{J}_{i,j}$.

Step 3. Define the approximate cell average over $I_{i,j}$ in the computational domain by

$$\tilde{U}_{i,j} = \sum_{\mu,\nu=1}^Q \omega_{\mu,\nu} \mathring{U}_{\mu,\nu},$$

where $\omega_{\mu,\nu}$ is the corresponding quadrature weights.

Step 4. Based on the cell averages $\{\tilde{U}_{i,j}\}$, employ the dimension-by-dimension WENO reconstruction to obtain the high-order approximate values $\{\check{U}_{i\mu,j\nu}\}$ at the quadrature points $\{((\xi_1)_{i\mu}, (\xi_2)_{j\nu})\}$. Denote $\gamma_{i,j} = \overline{JU}_{i,j} - \sum_{\mu,\nu} \omega_{\mu,\nu} J_{i\mu,j\nu} \check{U}_{i\mu,j\nu}$. We modify $U_{i\mu,j\nu} = \check{U}_{i\mu,j\nu} + \gamma_{i,j} / J_{i\mu,j\nu}$ to ensure that $\sum_{\mu,\nu} \omega_{\mu,\nu} J_{i\mu,j\nu} U_{i\mu,j\nu} = \overline{JU}_{i,j}$. One can obtain the values $U_{i+\frac{1}{2},j}^{-\mu} = U_{iQ,j\mu}$, $U_{i-\frac{1}{2},j}^{+\mu} = U_{i1,j\mu}$, $U_{i,j+\frac{1}{2}}^{-\mu} = U_{i\mu,jQ}$, and $U_{i,j-\frac{1}{2}}^{+\mu} = U_{i\mu,j1}$. As the 1D discussions in Section 3.1, the coefficients utilized for the reconstructions in $J(h^\circ + b)_{i\mu,j\nu}$ and $\mathring{J}_{i\mu,j\nu}$ need to be the same, so that $U_{i\mu,j\nu} + \mathbf{w}_{i\mu,j\nu} = C\mathbf{q}_{i\mu,j\nu}$.

The condition

$$J_{i\mu,j\nu} > 0, \quad h_{i\mu,j\nu} \geq 0, \quad \forall i, j, \mu, \nu, \quad (52)$$

is important for the PP property of our 2D moving mesh finite volume schemes in Theorems 4.2 and 4.3. However, the WENO reconstruction procedure does not guarantee satisfaction of condition (52). As the 1D case, the following 2D PP limiter is performed to enforce this condition.

Remark 6 (2D PP limiter). If $\overline{J}_{i,j} > 0$ and $\overline{h}_{i,j} \geq 0$, the 2D PP limiter modifies $J_{i\mu,j\nu}$ and $h_{i\mu,j\nu}$ to

$$\widehat{J}_{i\mu,j\nu} = \theta_J (J_{i\mu,j\nu} - \overline{J}_{i,j}) + \overline{J}_{i,j}, \quad \widehat{h}_{i\mu,j\nu} = \theta_h (h_{i\mu,j\nu} - \overline{h}_{i,j}) + \overline{h}_{i,j} \quad \forall \mu, \nu$$

with

$$\theta_J := \begin{cases} 1, & \text{if } \min_{\mu,\nu} \{J_{i\mu,j\nu}\} = \overline{J}_{i,j}, \\ \min \left\{ \left| \frac{\overline{J}_{i,j} - \epsilon_0}{\overline{J}_{i,j} - \min_{\mu,\nu} \{J_{i\mu,j\nu}\}} \right|, 1 \right\}, & \text{otherwise,} \end{cases}$$

$$\theta_h := \begin{cases} 1, & \text{if } \min_{\mu, \nu} \{h_{i_\mu, j_\nu}\} = \bar{h}_{i, j}, \\ \min \left\{ \left| \frac{\bar{h}_{i, j}}{\bar{h}_{i, j} - \min_{\mu, \nu} \{h_{i_\mu, j_\nu}\}} \right|, 1 \right\}, & \text{otherwise.} \end{cases}$$

Here, $\epsilon_0 = \min\{10^{-13}, \bar{J}_{i, j}\}$. The condition (52) is guaranteed after the PP limiter. When $J_{i_\mu, j_\nu} > 0$ and $h_{i_\mu, j_\nu} \geq 0$, one has $\widehat{J}_{i_\mu, j_\nu} = J_{i_\mu, j_\nu}$ and $\widehat{h}_{i_\mu, j_\nu} = h_{i_\mu, j_\nu}$. We use $\widehat{J}_{i_\mu, j_\nu}$ to replace J_{i_μ, j_ν} in Step 4 to ensure $\sum_{\mu, \nu} \omega_{\mu, \nu} \widehat{J}_{i_\mu, j_\nu} \mathbf{U}_{i_\mu, j_\nu} = \overline{J} \mathbf{U}_{i, j}$. To maintain the WB property after performing the PP limiting procedure, the bottom topography is updated by

$$\widehat{b}_{i_\mu, j_\nu} = h_{i_\mu, j_\nu} + b_{i_\mu, j_\nu} - \widehat{h}_{i_\mu, j_\nu}.$$

In the computation, we employ $\widehat{\mathbf{U}}_{i_\mu, j_\nu} = (\widehat{h}_{i_\mu, j_\nu}, (hv_1)_{i_\mu, j_\nu}, (hv_2)_{i_\mu, j_\nu})^\top$, $\widehat{\mathbf{w}}_{i_\mu, j_\nu} = (\widehat{b}_{i_\mu, j_\nu}, 0, 0)^\top$ and J_{i_μ, j_ν} to replace $\mathbf{U}_{i_\mu, j_\nu}$, $\mathbf{w}_{i_\mu, j_\nu}$ and J_{i_μ, j_ν} , respectively. This ensures $\widehat{\mathbf{U}}_{i_\mu, j_\nu} + \widehat{\mathbf{w}}_{i_\mu, j_\nu} = C \mathbf{q}_{i_\mu, j_\nu}$. It also preserves the conservative property.

4.4. Analysis of WB property

The subsection proves the WB property of our 2D schemes.

Theorem 4.1. Consider the semi-discrete schemes (33)–(36), (47)–(48) with the numerical fluxes (37)–(43) and (49). These schemes are WB, in the sense that, under the forward Euler or explicit SSP RK discretizations, when a steady state is reached at the n th time level t^n , i.e.,

$$\overline{\mathbf{U}}_{i, j}^n + \overline{\mathbf{w}}_{i, j}^n = C \overline{\mathbf{q}}_{i, j}^n \quad \forall i, j,$$

the numerical solution at t^{n+1} also satisfies

$$\overline{\mathbf{U}}_{i, j}^{n+1} + \overline{\mathbf{w}}_{i, j}^{n+1} = C \overline{\mathbf{q}}_{i, j}^{n+1} \quad \forall i, j.$$

Proof. Since an SSP RK method is a convex combination of forward Euler method, we only need to show the conclusion for the forward Euler discretization without loss of generality. The discrete SCLs (35) and (36) give

$$\begin{aligned} \sum_{\mu=1}^Q \omega_\mu \left[\frac{1}{\Delta \xi_1} \left(\left(J \frac{\partial \xi_1}{\partial x_1} \right)_{i+\frac{1}{2}, j}^\mu - \left(J \frac{\partial \xi_1}{\partial x_1} \right)_{i-\frac{1}{2}, j}^\mu \right) + \frac{1}{\Delta \xi_2} \left(\left(J \frac{\partial \xi_2}{\partial x_1} \right)_{i, j+\frac{1}{2}}^\mu - \left(J \frac{\partial \xi_2}{\partial x_1} \right)_{i, j-\frac{1}{2}}^\mu \right) \right] &= 0, \\ \sum_{\mu=1}^Q \omega_\mu \left[\frac{1}{\Delta \xi_1} \left(\left(J \frac{\partial \xi_1}{\partial x_2} \right)_{i+\frac{1}{2}, j}^\mu - \left(J \frac{\partial \xi_1}{\partial x_2} \right)_{i-\frac{1}{2}, j}^\mu \right) + \frac{1}{\Delta \xi_2} \left(\left(J \frac{\partial \xi_2}{\partial x_2} \right)_{i, j+\frac{1}{2}}^\mu - \left(J \frac{\partial \xi_2}{\partial x_2} \right)_{i, j-\frac{1}{2}}^\mu \right) \right] &= 0. \end{aligned}$$

Summing the above two equations and using the definitions of L_1 and L_2 in (9), we obtain the following equality

$$\sum_{\mu=1}^Q \omega_\mu \frac{1}{\Delta \xi_1} \left[(L_1)_{i+\frac{1}{2}, j}^\mu \langle (\mathbf{n}_1)_{i+\frac{1}{2}, j}^\mu, \mathbf{C} \rangle - (L_1)_{i-\frac{1}{2}, j}^\mu \langle (\mathbf{n}_1)_{i-\frac{1}{2}, j}^\mu, \mathbf{C} \rangle \right]$$

$$+ \sum_{\mu=1}^Q \omega_{\mu} \frac{1}{\Delta \xi_2} \left[(L_2)_{i,j+\frac{1}{2}}^{\mu} \langle (n_2)_{i,j+\frac{1}{2}}^{\mu}, C \rangle - (L_2)_{i,j-\frac{1}{2}}^{\mu} \langle (n_2)_{i,j-\frac{1}{2}}^{\mu}, C \rangle \right] = 0. \quad (53)$$

When a steady state is reached, the condition (46) holds. Based on the condition (46) and the equality (53), the discrete evolution equations (33) of JU degenerate to

$$(\overline{JU})_{i,j}^{n+1} - (\overline{JU})_{i,j}^n = - \frac{\Delta t}{\Delta \xi_1} \left((\tilde{\mathcal{F}}_1)_{i+\frac{1}{2},j} - (\tilde{\mathcal{F}}_1)_{i-\frac{1}{2},j} \right) - \frac{\Delta t}{\Delta \xi_2} \left((\tilde{\mathcal{F}}_2)_{i,j+\frac{1}{2}} - (\tilde{\mathcal{F}}_2)_{i,j-\frac{1}{2}} \right) \quad (54)$$

with

$$\begin{aligned} (\tilde{\mathcal{F}}_1)_{i+\frac{1}{2},j} &= \sum_{\mu=1}^Q \omega_{\mu} \left[\left(J \frac{\partial \xi_1}{\partial t} \right)_{i+\frac{1}{2},j}^{\mu} \{\mathbf{U}\}_{i+\frac{1}{2},j}^{\mu} - \frac{\alpha_1}{2} \llbracket \mathbf{U} \rrbracket_{i+\frac{1}{2},j}^{\mu} \right], \\ (\tilde{\mathcal{F}}_1)_{i-\frac{1}{2},j} &= \sum_{\mu=1}^Q \omega_{\mu} \left[\left(J \frac{\partial \xi_1}{\partial t} \right)_{i-\frac{1}{2},j}^{\mu} \{\mathbf{U}\}_{i-\frac{1}{2},j}^{\mu} - \frac{\alpha_1}{2} \llbracket \mathbf{U} \rrbracket_{i-\frac{1}{2},j}^{\mu} \right], \\ (\tilde{\mathcal{F}}_2)_{i,j+\frac{1}{2}} &= \sum_{\mu=1}^Q \omega_{\mu} \left[\left(J \frac{\partial \xi_2}{\partial t} \right)_{i,j+\frac{1}{2}}^{\mu} \{\mathbf{U}\}_{i,j+\frac{1}{2}}^{\mu} - \frac{\alpha_2}{2} \llbracket \mathbf{U} \rrbracket_{i,j+\frac{1}{2}}^{\mu} \right], \\ (\tilde{\mathcal{F}}_2)_{i,j-\frac{1}{2}} &= \sum_{\mu=1}^Q \omega_{\mu} \left[\left(J \frac{\partial \xi_2}{\partial t} \right)_{i,j-\frac{1}{2}}^{\mu} \{\mathbf{U}\}_{i,j-\frac{1}{2}}^{\mu} - \frac{\alpha_2}{2} \llbracket \mathbf{U} \rrbracket_{i,j-\frac{1}{2}}^{\mu} \right]. \end{aligned}$$

The discrete evolution equations of $J\mathbf{w}$ and $J\mathbf{q}$ can be expressed as

$$(\overline{J\mathbf{w}})_{i,j}^{n+1} - (\overline{J\mathbf{w}})_{i,j}^n = - \frac{1}{\Delta \xi_1} \left(\tilde{\mathbf{w}}_{i+\frac{1}{2},j} - \tilde{\mathbf{w}}_{i-\frac{1}{2},j} \right) - \frac{1}{\Delta \xi_2} \left(\tilde{\mathbf{w}}_{i,j+\frac{1}{2}} - \tilde{\mathbf{w}}_{i,j-\frac{1}{2}} \right), \quad (55)$$

$$(\overline{J\mathbf{q}})_{i,j}^{n+1} - (\overline{J\mathbf{q}})_{i,j}^n = - \frac{1}{\Delta \xi_1} \left(\tilde{\mathbf{q}}_{i+\frac{1}{2},j} - \tilde{\mathbf{q}}_{i-\frac{1}{2},j} \right) - \frac{1}{\Delta \xi_2} \left(\tilde{\mathbf{q}}_{i,j+\frac{1}{2}} - \tilde{\mathbf{q}}_{i,j-\frac{1}{2}} \right). \quad (56)$$

Combining (54) with (55) gives

$$\begin{aligned} (\overline{J(\mathbf{U} + \mathbf{w})})_{i,j}^{n+1} - (\overline{J(\mathbf{U} + \mathbf{w})})_{i,j}^n &= - \sum_{\mu=1}^Q \omega_{\mu} \frac{\Delta t}{\Delta \xi_1} \left(\left(J \frac{\partial \xi_1}{\partial t} \right)_{i+\frac{1}{2},j}^{\mu} \{\mathbf{U} + \mathbf{w}\}_{i+\frac{1}{2},j}^{\mu} - \frac{\alpha_1}{2} \llbracket \mathbf{U} + \mathbf{w} \rrbracket_{i+\frac{1}{2},j}^{\mu} \right. \\ &\quad \left. - \left(J \frac{\partial \xi_1}{\partial t} \right)_{i-\frac{1}{2},j}^{\mu} \{\mathbf{U} + \mathbf{w}\}_{i-\frac{1}{2},j}^{\mu} + \frac{\alpha_1}{2} \llbracket \mathbf{U} + \mathbf{w} \rrbracket_{i-\frac{1}{2},j}^{\mu} \right) \\ &\quad - \sum_{\mu=1}^Q \omega_{\mu} \frac{\Delta t}{\Delta \xi_2} \left(\left(J \frac{\partial \xi_2}{\partial t} \right)_{i,j+\frac{1}{2}}^{\mu} \{\mathbf{U} + \mathbf{w}\}_{i,j+\frac{1}{2}}^{\mu} - \frac{\alpha_2}{2} \llbracket \mathbf{U} + \mathbf{w} \rrbracket_{i,j+\frac{1}{2}}^{\mu} \right. \\ &\quad \left. - \left(J \frac{\partial \xi_2}{\partial t} \right)_{i,j-\frac{1}{2}}^{\mu} \{\mathbf{U} + \mathbf{w}\}_{i,j-\frac{1}{2}}^{\mu} + \frac{\alpha_2}{2} \llbracket \mathbf{U} + \mathbf{w} \rrbracket_{i,j-\frac{1}{2}}^{\mu} \right). \quad (57) \end{aligned}$$

The reconstruction procedure yields $\mathbf{U}_{i_{\mu},j_{\nu}} + \mathbf{w}_{i_{\mu},j_{\nu}} = C\mathbf{q}_{i_{\mu},j_{\nu}}$. This implies

$$\{\mathbf{U} + \mathbf{w}\} = C\{\mathbf{q}\}, \quad \llbracket \mathbf{U} + \mathbf{w} \rrbracket = C\llbracket \mathbf{q} \rrbracket.$$

Plugging the above relations into (57), one gets

$$\begin{aligned}
(\overline{J(U+w)})_{i,j}^{n+1} - (\overline{JCq})_{i,j}^n = & - \sum_{\mu=1}^Q \omega_{\mu} \frac{\Delta t}{\Delta \xi_1} \left(\left(J \frac{\partial \xi_1}{\partial t} \right)_{i+\frac{1}{2},j}^{\mu} \{Cq\}_{i+\frac{1}{2},j}^{\mu} - \frac{\alpha_1}{2} \llbracket Cq \rrbracket_{i+\frac{1}{2},j}^{\mu} \right. \\
& \left. - \left(J \frac{\partial \xi_1}{\partial t} \right)_{i-\frac{1}{2},j}^{\mu} \{Cq\}_{i-\frac{1}{2},j}^{\mu} + \frac{\alpha_1}{2} \llbracket Cq \rrbracket_{i-\frac{1}{2},j}^{\mu} \right) \\
& - \sum_{\mu=1}^Q \omega_{\mu} \frac{\Delta t}{\Delta \xi_2} \left(\left(J \frac{\partial \xi_2}{\partial t} \right)_{i,j+\frac{1}{2}}^{\mu} \{Cq\}_{i,j+\frac{1}{2}}^{\mu} - \frac{\alpha_2}{2} \llbracket Cq \rrbracket_{i,j+\frac{1}{2}}^{\mu} \right. \\
& \left. - \left(J \frac{\partial \xi_2}{\partial t} \right)_{i,j-\frac{1}{2}}^{\mu} \{Cq\}_{i,j-\frac{1}{2}}^{\mu} + \frac{\alpha_2}{2} \llbracket Cq \rrbracket_{i,j-\frac{1}{2}}^{\mu} \right).
\end{aligned}$$

Substituting (56) into the above equation gives

$$(\overline{J(U+w)})_{i,j}^{n+1} = C \overline{J}_{i,j}^{n+1} \overline{q}_{i,j}^{n+1},$$

which implies

$$\overline{U}_{i,j}^{n+1} + \overline{w}_{i,j}^{n+1} = C \overline{q}_{i,j}^{n+1}.$$

The proof is completed. \square

4.5. Analysis of PP property

The semi-discrete schemes (33) and (34) coupled with the forward Euler time discretization can be represented as

$$\overline{JU}_{i,j}^{\Delta t} = \overline{JU}_{i,j} - \Delta t L_{i,j}, \quad \overline{J}_{i,j}^{\Delta t} = \overline{J}_{i,j} - \Delta t L_{i,j},$$

where $L_{i,j}$ and $L_{i,j}$ denote the right-hand-side terms of (33) and (34), respectively. $\overline{JU}_{i,j}$ and $\overline{J}_{i,j}$ denote the approximations at the n th time level.

Theorem 4.2. Assume that $\overline{J}_{i,j} > 0$ for all i and j . If $J_{i,\mu,j,\nu} > 0$ for all i, j, μ, ν , then $\overline{J}_{i,j}^{\Delta t} > 0$ holds under the condition

$$\Delta t \leq \frac{1}{2} \min \left\{ \frac{\omega_1 \Delta \xi_1}{(\beta_1)_J}, \frac{\omega_1 \Delta \xi_2}{(\beta_2)_J} \right\}. \quad (58)$$

The proof is omitted here, since it is similar to the proof of Theorems 3.2 and 4.3. Indeed, one can let $h = 1, L_1 = 0, L_2 = 0$ in Theorem 4.3, and utilize the similar arguments in Theorems 3.2 and 4.3 to get the conclusion.

Remark 7. As discussed in Remark 5, the mesh should not interleave or overlap during computation, i.e., if the mesh satisfy $(x_1)_{i-\frac{1}{2},j+\frac{1}{2}} < (x_1)_{i+\frac{1}{2},j+\frac{1}{2}}$ for $i = 0, \dots, N_1 - 1$ and $(x_2)_{i+\frac{1}{2},j-\frac{1}{2}} < (x_2)_{i+\frac{1}{2},j+\frac{1}{2}}$ for $j = 0, \dots, N_2 - 1$, then for the new mesh $(x_1)_{i-\frac{1}{2},j+\frac{1}{2}}^{\Delta t} < (x_1)_{i+\frac{1}{2},j+\frac{1}{2}}^{\Delta t}$ and $(x_2)_{i+\frac{1}{2},j-\frac{1}{2}}^{\Delta t} < (x_2)_{i+\frac{1}{2},j+\frac{1}{2}}^{\Delta t}$ still holds. The treatment will be detailed in Section 5.

Theorem 4.3. Assume that $\bar{U}_{i,j} \in \mathcal{G}$ and $\bar{J}_{i,j} > 0$ for all i and j . If $\bar{J}_{i,j}^{\Delta t} > 0$, and

$$J_{i_\mu, j_\nu} > 0, \quad h_{i_\mu, j_\nu} \geq 0, \quad \forall i, j, \mu, \nu, \quad (59)$$

then the PP property

$$\bar{U}_{i,j}^{\Delta t} := \bar{J} \bar{U}_{i,j}^{\Delta t} / \bar{J}_{i,j}^{\Delta t} \in \mathcal{G},$$

holds under the CFL condition

$$\Delta t \leq \frac{1}{2} \min_{i,j,\mu} \left\{ \frac{\omega_1 J_{i\pm\frac{1}{2},j}^{\mp,\mu} \Delta \xi_1}{\alpha_1 + (L_1)_{i\pm\frac{1}{2},j}^\mu \beta}, \frac{\omega_1 J_{i,j\pm\frac{1}{2}}^{\mp,\mu} \Delta \xi_2}{\alpha_2 + (L_2)_{i,j\pm\frac{1}{2}}^\mu \beta} \right\}. \quad (60)$$

Proof. Consider the discrete evolution equation for Jh :

$$\begin{aligned} \bar{J}h_{i,j}^{\Delta t} - \bar{J}h_{i,j} &= -\frac{\Delta t}{\Delta \xi_1} \sum_{\mu=1}^Q \omega_\mu \left[\left(J \frac{\partial \xi_1}{\partial t} \right)_{i+\frac{1}{2},j}^\mu \llbracket h \rrbracket_{i+\frac{1}{2},j}^\mu - \frac{\alpha_1}{2} \llbracket h \rrbracket_{i+\frac{1}{2},j}^\mu - \left(J \frac{\partial \xi_1}{\partial t} \right)_{i-\frac{1}{2},j}^\mu \llbracket h \rrbracket_{i-\frac{1}{2},j}^\mu + \frac{\alpha_1}{2} \llbracket h \rrbracket_{i-\frac{1}{2},j}^\mu \right] \\ &\quad - \frac{\Delta t}{\Delta \xi_1} \sum_{\mu=1}^Q \omega_\mu \left[(L_1)_{i+\frac{1}{2},j}^\mu \langle (n_1)_{i+\frac{1}{2},j}^\mu, (\tilde{F}_{i+\frac{1}{2},j}^\mu)_1 \rangle - (L_1)_{i+\frac{1}{2},j}^\mu \frac{\beta}{2} \llbracket h \rrbracket_{i+\frac{1}{2},j}^{\mu,*} \right. \\ &\quad \left. - (L_1)_{i-\frac{1}{2},j}^\mu \langle (n_1)_{i-\frac{1}{2},j}^\mu, (\tilde{F}_{i-\frac{1}{2},j}^\mu)_1 \rangle + (L_1)_{i-\frac{1}{2},j}^\mu \frac{\beta}{2} \llbracket h \rrbracket_{i-\frac{1}{2},j}^{\mu,*} \right] \\ &\quad - \frac{\Delta t}{\Delta \xi_2} \sum_{\mu=1}^Q \omega_\mu \left[\left(J \frac{\partial \xi_2}{\partial t} \right)_{i,j+\frac{1}{2}}^\mu \llbracket h \rrbracket_{i,j+\frac{1}{2}}^\mu - \frac{\alpha_2}{2} \llbracket h \rrbracket_{i,j+\frac{1}{2}}^\mu - \left(J \frac{\partial \xi_2}{\partial t} \right)_{i,j-\frac{1}{2}}^\mu \llbracket h \rrbracket_{i,j-\frac{1}{2}}^\mu + \frac{\alpha_2}{2} \llbracket h \rrbracket_{i,j-\frac{1}{2}}^\mu \right] \\ &\quad - \frac{\Delta t}{\Delta \xi_2} \sum_{\mu=1}^Q \omega_\mu \left[(L_2)_{i,j+\frac{1}{2}}^\mu \langle (n_2)_{i,j+\frac{1}{2}}^\mu, (\tilde{F}_{i,j+\frac{1}{2}}^\mu)_1 \rangle - (L_2)_{i,j+\frac{1}{2}}^\mu \frac{\beta}{2} \llbracket h \rrbracket_{i,j+\frac{1}{2}}^{\mu,*} \right. \\ &\quad \left. - (L_2)_{i,j-\frac{1}{2}}^\mu \langle (n_2)_{i,j-\frac{1}{2}}^\mu, (\tilde{F}_{i,j-\frac{1}{2}}^\mu)_1 \rangle + (L_2)_{i,j-\frac{1}{2}}^\mu \frac{\beta}{2} \llbracket h \rrbracket_{i,j-\frac{1}{2}}^{\mu,*} \right]. \end{aligned} \quad (61)$$

Based on the relations

$$\begin{aligned} \pm \langle (n_1)_{i\pm\frac{1}{2},j}^\mu, (\tilde{F}_{i\pm\frac{1}{2},j}^\mu)_1 \rangle &\leq \beta \llbracket h \rrbracket_{i\pm\frac{1}{2},j}^{\mu,*}, \quad \pm \langle (n_2)_{i,j\pm\frac{1}{2}}^\mu, (\tilde{F}_{i,j\pm\frac{1}{2}}^\mu)_1 \rangle \leq \beta \llbracket h \rrbracket_{i,j\pm\frac{1}{2}}^{\mu,*}, \\ \frac{\alpha_1}{2} \llbracket h \rrbracket_{i+\frac{1}{2},j}^\mu - \frac{\alpha_1}{2} \llbracket h \rrbracket_{i-\frac{1}{2},j}^\mu &= \alpha_1 \llbracket h \rrbracket_{i+\frac{1}{2},j}^\mu + \alpha_1 \llbracket h \rrbracket_{i-\frac{1}{2},j}^\mu - \alpha_1 h_{i+\frac{1}{2},j}^{-,\mu} - \alpha_1 h_{i-\frac{1}{2},j}^{+,\mu}, \\ \frac{\alpha_2}{2} \llbracket h \rrbracket_{i,j+\frac{1}{2}}^\mu - \frac{\alpha_2}{2} \llbracket h \rrbracket_{i,j-\frac{1}{2}}^\mu &= \alpha_2 \llbracket h \rrbracket_{i,j+\frac{1}{2}}^\mu + \alpha_2 \llbracket h \rrbracket_{i,j-\frac{1}{2}}^\mu - \alpha_2 h_{i,j+\frac{1}{2}}^{-,\mu} - \alpha_2 h_{i,j-\frac{1}{2}}^{+,\mu}, \end{aligned}$$

the lower bound of the right-hand side of (61) can be estimated as

$$\bar{J}h_{i,j}^{\Delta t} - \bar{J}h_{i,j} \geq I_1 + I_2 + I_3 + I_4 \quad (62)$$

with

$$\begin{aligned}
I_1 &= \frac{\Delta t}{\Delta \xi_1} \sum_{\mu=1}^Q \omega_{\mu} \left[\left(\left(\alpha_1 - J \frac{\partial \xi_1}{\partial t} \right)^{\mu}_{i+\frac{1}{2},j} \right) \{h\}_{i+\frac{1}{2},j}^{\mu} + \left(\left(\alpha_1 + J \frac{\partial \xi_1}{\partial t} \right)^{\mu}_{i-\frac{1}{2},j} \right) \{h\}_{i-\frac{1}{2},j}^{\mu} \right], \\
I_2 &= \frac{\Delta t}{\Delta \xi_2} \sum_{\mu=1}^Q \omega_{\mu} \left[\left(\left(\alpha_2 - J \frac{\partial \xi_2}{\partial t} \right)^{\mu}_{i,j+\frac{1}{2}} \right) \{h\}_{i,j+\frac{1}{2}}^{\mu} + \left(\left(\alpha_2 + J \frac{\partial \xi_2}{\partial t} \right)^{\mu}_{i,j-\frac{1}{2}} \right) \{h\}_{i,j-\frac{1}{2}}^{\mu} \right], \\
I_3 &= -\frac{\Delta t}{\Delta \xi_1} \sum_{\mu=1}^Q \omega_{\mu} \left[(L_1)^{\mu}_{i+\frac{1}{2},j} \beta h_{i+\frac{1}{2},j}^{-\mu,*} + (L_1)^{\mu}_{i-\frac{1}{2},j} \beta h_{i-\frac{1}{2},j}^{+\mu,*} \right] \\
&\quad - \frac{\Delta t}{\Delta \xi_2} \sum_{\mu=1}^Q \omega_{\mu} \left[(L_2)^{\mu}_{i,j+\frac{1}{2}} \beta h_{i,j+\frac{1}{2}}^{-\mu,*} + (L_2)^{\mu}_{i,j-\frac{1}{2}} \beta h_{i,j-\frac{1}{2}}^{+\mu,*} \right], \\
I_4 &= -\frac{\Delta t}{\Delta \xi_1} \sum_{\mu=1}^Q \omega_{\mu} \left[\alpha_1 h_{i+\frac{1}{2},j}^{-\mu} + \alpha_1 h_{i-\frac{1}{2},j}^{+\mu} \right] - \frac{\Delta t}{\Delta \xi_2} \sum_{\mu=1}^Q \omega_{\mu} \left[\alpha_2 h_{i,j+\frac{1}{2}}^{-\mu} + \alpha_2 h_{i,j-\frac{1}{2}}^{+\mu} \right].
\end{aligned}$$

The definitions of α_1 and α_2 in (44) ensure $I_1 \geq 0$ and $I_2 \geq 0$. The remaining task is to estimate I_3 and I_4 . Utilizing $h_{i,j\pm\frac{1}{2}}^{\mp,\mu,*} \leq h_{i,j\pm\frac{1}{2}}^{\mp,\mu}$ and $h_{i\pm\frac{1}{2},j}^{\mp,\mu,*} \leq h_{i\pm\frac{1}{2},j}^{\mp,\mu}$ gives

$$\begin{aligned}
I_3 + I_4 &\geq -\frac{\Delta t}{\Delta \xi_1} \sum_{\mu=1}^Q \omega_{\mu} \left[(L_1)^{\mu}_{i+\frac{1}{2},j} \beta h_{i+\frac{1}{2},j}^{-\mu} + (L_1)^{\mu}_{i-\frac{1}{2},j} \beta h_{i-\frac{1}{2},j}^{+\mu} \right] \\
&\quad - \frac{\Delta t}{\Delta \xi_2} \sum_{\mu=1}^Q \omega_{\mu} \left[(L_2)^{\mu}_{i,j+\frac{1}{2}} \beta h_{i,j+\frac{1}{2}}^{-\mu} + (L_2)^{\mu}_{i,j-\frac{1}{2}} \beta h_{i,j-\frac{1}{2}}^{+\mu} \right] \\
&\quad - \frac{\Delta t}{\Delta \xi_1} \sum_{\mu=1}^Q \omega_{\mu} \left[\alpha_1 h_{i+\frac{1}{2},j}^{-\mu} + \alpha_1 h_{i-\frac{1}{2},j}^{+\mu} \right] - \frac{\Delta t}{\Delta \xi_2} \sum_{\mu=1}^Q \omega_{\mu} \left[\alpha_2 h_{i,j+\frac{1}{2}}^{-\mu} + \alpha_2 h_{i,j-\frac{1}{2}}^{+\mu} \right] \\
&= -\frac{\Delta t}{\Delta \xi_1} \sum_{\mu=1}^Q \omega_{\mu} \left[\left(\alpha_1 + (L_1)^{\mu}_{i+\frac{1}{2},j} \beta \right) h_{i+\frac{1}{2},j}^{-\mu} + \left(\alpha_1 + (L_1)^{\mu}_{i-\frac{1}{2},j} \beta \right) h_{i-\frac{1}{2},j}^{+\mu} \right] \\
&\quad - \frac{\Delta t}{\Delta \xi_2} \sum_{\mu=1}^Q \omega_{\mu} \left[\left(\alpha_2 + (L_2)^{\mu}_{i,j+\frac{1}{2}} \beta \right) h_{i,j+\frac{1}{2}}^{-\mu} + \left(\alpha_2 + (L_2)^{\mu}_{i,j-\frac{1}{2}} \beta \right) h_{i,j-\frac{1}{2}}^{+\mu} \right]. \tag{63}
\end{aligned}$$

Plugging $I_1 \geq 0$, $I_2 \geq 0$, and (63) into equation (62), one obtains

$$\begin{aligned}
\bar{h}_{i,j}^{\Delta t} - \frac{\bar{J}h_{i,j}}{\bar{J}_{i,j}^{\Delta t}} &\geq -\frac{\Delta t}{\bar{J}_{i,j}^{\Delta t} \Delta \xi_1} \sum_{\mu=1}^Q \omega_{\mu} \left[\left(\alpha_1 + (L_1)^{\mu}_{i+\frac{1}{2},j} \beta \right) h_{i+\frac{1}{2},j}^{-\mu} + \left(\alpha_1 + (L_1)^{\mu}_{i-\frac{1}{2},j} \beta \right) h_{i-\frac{1}{2},j}^{+\mu} \right] \\
&\quad - \frac{\Delta t}{\bar{J}_{i,j}^{\Delta t} \Delta \xi_2} \sum_{\mu=1}^Q \omega_{\mu} \left[\left(\alpha_2 + (L_2)^{\mu}_{i,j+\frac{1}{2}} \beta \right) h_{i,j+\frac{1}{2}}^{-\mu} + \left(\alpha_2 + (L_2)^{\mu}_{i,j-\frac{1}{2}} \beta \right) h_{i,j-\frac{1}{2}}^{+\mu} \right]. \tag{64}
\end{aligned}$$

Furthermore, by using the fact

$$\bar{h}_{i,j} = \frac{1}{2} \sum_{\mu=1}^Q \sum_{\nu=2}^{Q-1} \omega_{\mu} \omega_{\nu} J_{i_{\mu},j_{\nu}} h_{i_{\mu},j_{\nu}} + \frac{1}{2} \sum_{\mu=2}^{Q-1} \sum_{\nu=1}^Q \omega_{\mu} \omega_{\nu} J_{i_{\mu},j_{\nu}} h_{i_{\mu},j_{\nu}}$$

$$+ \sum_{\mu=1}^Q \frac{\omega_\mu \omega_1}{2} \left[J_{i+\frac{1}{2},j}^{-\mu} h_{i+\frac{1}{2},j}^{-\mu} + J_{i-\frac{1}{2},j}^{+\mu} h_{i-\frac{1}{2},j}^{+\mu} + J_{i,j+\frac{1}{2}}^{-\mu} h_{i,j+\frac{1}{2}}^{-\mu} + J_{i,j-\frac{1}{2}}^{+\mu} h_{i,j-\frac{1}{2}}^{+\mu} \right],$$

the inequality (64) can be reformulated as

$$\begin{aligned} \bar{h}_{i,j}^{\Delta t} \geq & \frac{1}{J_{i,j}^{\Delta t}} \sum_{\mu=1}^Q \omega_\mu \left[\left(\frac{1}{2} \omega_1 J_{i+\frac{1}{2},j}^{-\mu} - \frac{\Delta t}{\Delta \xi_1} \left(\alpha_1 + (L_1)_{i+\frac{1}{2},j}^\mu \beta \right) \right) h_{i+\frac{1}{2},j}^{-\mu} + \left(\frac{1}{2} \omega_1 J_{i-\frac{1}{2},j}^{+\mu} - \frac{\Delta t}{\Delta \xi_1} \left(\alpha_1 + (L_1)_{i-\frac{1}{2},j}^\mu \beta \right) \right) h_{i-\frac{1}{2},j}^{+\mu} \right] \\ & + \frac{1}{J_{i,j}^{\Delta t}} \sum_{\mu=1}^Q \omega_\mu \left[\left(\frac{1}{2} \omega_1 J_{i,j+\frac{1}{2}}^{-\mu} - \frac{\Delta t}{\Delta \xi_2} \left(\alpha_2 + (L_2)_{i,j+\frac{1}{2}}^\mu \beta \right) \right) h_{i,j+\frac{1}{2}}^{-\mu} + \left(\frac{1}{2} \omega_1 J_{i,j-\frac{1}{2}}^{+\mu} - \frac{\Delta t}{\Delta \xi_2} \left(\alpha_2 + (L_2)_{i,j-\frac{1}{2}}^\mu \beta \right) \right) h_{i,j-\frac{1}{2}}^{+\mu} \right] \\ & + \frac{1}{2J_{i,j}^{\Delta t}} \sum_{\mu=1}^Q \sum_{\nu=2}^{Q-1} \omega_\mu \omega_\nu J_{i_\mu,j_\nu} h_{i_\mu,j_\nu} + \frac{1}{2J_{i,j}^{\Delta t}} \sum_{\mu=2}^Q \sum_{\nu=1}^Q \omega_\mu \omega_\nu J_{i_\mu,j_\nu} h_{i_\mu,j_\nu}, \end{aligned}$$

where we have used the facts $h_{i-\frac{1}{2},j}^{+\mu} = h_{i_1,j_\mu}$, $h_{i+\frac{1}{2},j}^{-\mu} = h_{i_Q,j_\mu}$, $h_{i,j-\frac{1}{2}}^{+\mu} = h_{i_\mu,j_1}$, and $h_{i,j+\frac{1}{2}}^{-\mu} = h_{i_\mu,j_Q}$.

Under the condition (59) and the CFL condition (60), one obtains

$$\bar{h}_{i,j}^{\Delta t} \geq 0,$$

which means $\bar{U}_{i,j}^{\Delta t} \in \mathcal{G}$. The proof is completed. \square

5. Adaptive moving mesh

This section presents the adaptive moving mesh strategy that determines the mesh velocities involved in the temporal mesh metrics; see [11, 12, 26] for more details. We will take the 2D case as an example. Define the following mesh adaptation functional

$$\widetilde{E}(\mathbf{x}) = \frac{1}{2} \sum_{\ell=1}^2 \int_{\Omega_c} (\nabla_{\xi} x_{\ell})^{\top} \mathbf{G}_{\ell} (\nabla_{\xi} x_{\ell}) d\xi,$$

whose Euler-Lagrange equations are

$$\nabla_{\xi} \cdot (\mathbf{G}_{\ell} \nabla_{\xi} x_{\ell}) = 0, \quad \xi \in \Omega_c, \quad \ell = 1, 2, \quad (65)$$

where ∇_{ξ} denotes the spatial gradient in the computational domain. Then the new redistributed mesh \mathbf{x} in the physical domain Ω_p can be obtained by solving (65) for a given symmetric positive definite matrix \mathbf{G}_{ℓ} , which controls the mesh concentration. The choice of \mathbf{G}_{ℓ} is one of the most important parts of the adaptive moving mesh method, and usually depends on the solutions of the underlying governing equations or their derivatives. Referring to the variable diffusion method in [30], the simplest choice is the isotropic one as follows

$$\mathbf{G}_{\ell} = \omega I_2, \quad \ell = 1, 2,$$

where the positive scalar ω is called the monitor function. It can be taken as

$$\omega = \left(1 + \sum_{k=1}^K \theta_k \left(\frac{|\nabla_{\xi} \sigma_k|}{\max |\nabla_{\xi} \sigma_k|} \right)^2 \right)^{1/2}. \quad (66)$$

Here $\{\sigma_k\}_{k=1}^K$ are the chosen physical variables, and θ_k is a positive parameter. The monitor function (66) is approximated by using the second-order central difference for the derivatives in the computational domain, and it is further smoothed by performing 5 ~ 10 times via the following low-pass filter

$$\omega_{i+\frac{1}{2}, j+\frac{1}{2}} = \sum_{i_1, j_1=0, \pm 1} \left(\frac{1}{2} \right)^{|i_1|+|j_1|+2} \omega_{i+\frac{1}{2}+i_1, j+\frac{1}{2}+j_1}.$$

Utilizing the second-order central difference scheme to discretize the mesh governing equations (65) and coupling it with the Jacobi iteration method give

$$\begin{aligned} & \left[\left(\omega_{i+\frac{1}{2}, j+\frac{1}{2}} + \omega_{i+\frac{3}{2}, j+\frac{1}{2}} \right) \left(\mathbf{x}_{i+\frac{3}{2}, j+\frac{1}{2}}^{[\nu]} - \mathbf{x}_{i+\frac{1}{2}, j+\frac{1}{2}}^{[\nu+1]} \right) - \left(\omega_{i+\frac{1}{2}, j+\frac{1}{2}} + \omega_{i-\frac{1}{2}, j+\frac{1}{2}} \right) \left(\mathbf{x}_{i+\frac{1}{2}, j+\frac{1}{2}}^{[\nu+1]} - \mathbf{x}_{i-\frac{1}{2}, j+\frac{1}{2}}^{[\nu]} \right) \right] / \Delta \xi_1^2 \\ & \left[\left(\omega_{i+\frac{1}{2}, j+\frac{1}{2}} + \omega_{i+\frac{1}{2}, j+\frac{3}{2}} \right) \left(\mathbf{x}_{i+\frac{1}{2}, j+\frac{3}{2}}^{[\nu]} - \mathbf{x}_{i+\frac{1}{2}, j+\frac{1}{2}}^{[\nu+1]} \right) - \left(\omega_{i+\frac{1}{2}, j+\frac{1}{2}} + \omega_{i+\frac{1}{2}, j-\frac{1}{2}} \right) \left(\mathbf{x}_{i+\frac{1}{2}, j+\frac{1}{2}}^{[\nu+1]} - \mathbf{x}_{i+\frac{1}{2}, j-\frac{1}{2}}^{[\nu]} \right) \right] / \Delta \xi_2^2 \\ & = 0, \quad \nu = 0, 1, \dots, \mu-1, \end{aligned}$$

where the initial mesh in the iterations $\mathbf{x}_{i+\frac{1}{2}, j+\frac{1}{2}}^{[0]} := \mathbf{x}_{i+\frac{1}{2}, j+\frac{1}{2}}^n$ is chosen as the mesh at t^n , and the monitor function ω is computed based on the solution at t^n . Once the grid $\left\{ \mathbf{x}_{i+\frac{1}{2}, j+\frac{1}{2}}^{[\mu]} \right\}$ is obtained, the final adaptive mesh is given by

$$\mathbf{x}_{i+\frac{1}{2}, j+\frac{1}{2}}^{n+1} := \mathbf{x}_{i+\frac{1}{2}, j+\frac{1}{2}}^n + \Delta_{\tau} (\delta_{\tau} \mathbf{x})_{i+\frac{1}{2}, j+\frac{1}{2}}^n, \quad (\delta_{\tau} \mathbf{x})_{i+\frac{1}{2}, j+\frac{1}{2}}^n := \mathbf{x}_{i+\frac{1}{2}, j+\frac{1}{2}}^{[\mu]} - \mathbf{x}_{i+\frac{1}{2}, j+\frac{1}{2}}^n$$

with the parameter Δ_{τ} to control the mesh movement

$$\Delta_{\tau} \leq \begin{cases} -\frac{1}{2(\delta_{\tau} x_1)_{i+\frac{1}{2}, j+\frac{1}{2}}} \left[(x_1)_{i+\frac{1}{2}, j+\frac{1}{2}}^n - (x_1)_{i-\frac{1}{2}, j+\frac{1}{2}}^n \right], & (\delta_{\tau} x_1)_{i+\frac{1}{2}, j+\frac{1}{2}} < 0, \\ +\frac{1}{2(\delta_{\tau} x_1)_{i+\frac{1}{2}, j+\frac{1}{2}}} \left[(x_1)_{i+\frac{3}{2}, j+\frac{1}{2}}^n - (x_1)_{i+\frac{1}{2}, j+\frac{1}{2}}^n \right], & (\delta_{\tau} x_1)_{i+\frac{1}{2}, j+\frac{1}{2}} > 0, \\ -\frac{1}{2(\delta_{\tau} x_2)_{i+\frac{1}{2}, j+\frac{1}{2}}} \left[(x_2)_{i+\frac{1}{2}, j+\frac{1}{2}}^n - (x_2)_{i+\frac{1}{2}, j-\frac{1}{2}}^n \right], & (\delta_{\tau} x_2)_{i+\frac{1}{2}, j+\frac{1}{2}} < 0, \\ +\frac{1}{2(\delta_{\tau} x_2)_{i+\frac{1}{2}, j+\frac{1}{2}}} \left[(x_2)_{i+\frac{1}{2}, j+\frac{3}{2}}^n - (x_2)_{i+\frac{1}{2}, j+\frac{1}{2}}^n \right], & (\delta_{\tau} x_2)_{i+\frac{1}{2}, j+\frac{1}{2}} > 0. \end{cases}$$

Finally, the mesh velocities for the next time step are defined as

$$\dot{\mathbf{x}}_{i+\frac{1}{2}, j+\frac{1}{2}}^n := \Delta_{\tau} (\delta_{\tau} \mathbf{x})_{i+\frac{1}{2}, j+\frac{1}{2}}^n / \Delta t^n,$$

where Δt^n is the time stepsize. One can get the values $\dot{\mathbf{x}}_{i_{\mu}, j_{\nu}}$ by using the similar dimension-by-dimension approach illustrated in Subsection 4.2, so we omit it here.

To get the fully-discrete schemes, we use the explicit SSP RK3 time discretization

$$\begin{aligned}
(JU)^* &= (JU)^n + \Delta t^n L(U^n, \mathbf{x}^n), \quad J^* = J^n + \Delta t^n L(\mathbf{x}^n), \\
\mathbf{x}^* &= \mathbf{x}^n + \Delta t^n \dot{\mathbf{x}}^n, \\
(JU)^{**} &= \frac{3}{4} (JU)^n + \frac{1}{4} ((JU)^* + \Delta t^n L(U^*, \mathbf{x}^*)), \quad J^{**} = \frac{3}{4} J^n + \frac{1}{4} (J^* + \Delta t^n L(\mathbf{x}^*)), \\
\mathbf{x}^{**} &= \frac{3}{4} \mathbf{x}^n + \frac{1}{4} (\mathbf{x}^* + \Delta t^n \dot{\mathbf{x}}^n), \\
(JU)^{n+1} &= \frac{1}{3} (JU)^n + \frac{2}{3} ((JU)^{**} + \Delta t^n L(U^{**}, \mathbf{x}^{**})), \quad J^{n+1} = \frac{1}{3} J^n + \frac{2}{3} (J^{**} + \Delta t^n L(\mathbf{x}^{**})), \\
\mathbf{x}^{n+1} &= \frac{1}{3} \mathbf{x}^n + \frac{2}{3} (\mathbf{x}^{**} + \Delta t^n \dot{\mathbf{x}}^n),
\end{aligned}$$

where $\dot{\mathbf{x}}^n$ is the mesh velocity determined by using the adaptive moving mesh strategy in Section 5, L is the right-hand side of (10) or (33), and L is the right-hand side of the semi-discrete VCL (11) or (34).

6. Numerical tests

This section conducts several numerical experiments to validate the high-order accuracy, high resolution, and WB and PP properties of the proposed moving mesh scheme. For the adaptive mesh redistribution, the total number of iterations for solving the adaptive mesh equation (see [12, 19]) is set as 10, and the monitor function ω will be given in each example. The fifth-order WENO-Z method [3] is employed for spatial reconstruction. The time stepsize Δt^n is chosen according to Theorems 3.2, 3.3, 4.2 and 4.3, except for the accuracy tests in Examples 6.1 and 6.5, where it is taken as $\min\{\Delta t^n, (\Delta \xi)^{5/3}\}$ and $\min\{\Delta t^n, (\min_\ell\{\Delta \xi_\ell\})^{5/3}\}$, respectively, to align the temporal and spatial convergence rates. Our structure-preserving schemes on fixed uniform and moving meshes are denoted as “UM-SP” and “MM-SP”, respectively. To address the effect of round-off error for very shallow water depths, the velocities are computed using the following formula proposed in [15]:

$$(v_\ell) = \begin{cases} (hv_\ell)/(h), & \text{if } h > 10^{-4}, \\ \frac{\sqrt{2}h(hv_\ell)}{\sqrt{h^4 + \max\{h^4, \mathcal{T}\}}}, & \text{otherwise,} \end{cases}$$

where $\mathcal{T} = (\Delta \xi)^4$ in 1D cases and $T = (\Delta \xi_1 \Delta \xi_2)^2$ in 2D cases, respectively.

6.1. 1D tests

Example 6.1 (Accuracy test with manufactured solution). This example [47] is used to validate the convergence rate of the proposed moving mesh scheme by solving the following equations with an additional source term:

$$\frac{\partial U}{\partial t} + \frac{\partial F}{\partial x} = -gh \frac{\partial B}{\partial x} + S,$$

where the gravitational acceleration $g = 1$. The physical domain is set as $[0, 2]$ with periodic boundary conditions. The exact solution is given by

$$h(x, t) = 4 + \cos(\pi x) \cos(\pi t), \quad v_1(x, t) = \frac{\sin(\pi x) \sin(\pi t)}{h}, \quad b(x) = 1.5 + \sin(\pi x),$$

and the additional source term is defined as

$$\begin{aligned} S(x, t) = & (0, 4\pi \cos(\pi x) + \pi \cos(\pi t) \cos^2(\pi x) - 3\pi \cos(\pi t) \sin(\pi x) - \pi \cos^2(\pi t) \cos(\pi x) \sin(\pi x) \\ & + (\pi \cos(\pi t) \sin^2(\pi t) \sin^3(\pi x))/(\cos(\pi t) \cos(\pi x) + 4)^2 \\ & + (2\pi \cos(\pi x) \sin^2(\pi t) \sin(\pi x))/(\cos(\pi t) \cos(\pi x) + 4), 0)^\top. \end{aligned}$$

The numerical simulations are carried out up to $t = 0.1$. The monitor function is chosen as

$$\omega = \left(1 + \theta \left(\frac{|\nabla_\xi(h + b)|}{\max |\nabla_\xi(h + b)|} \right)^2 \right)^{1/2}$$

with $\theta = 3$.

Figure 1 presents the errors and the convergence behavior in the water depth h computed by the MM-SP scheme at $t = 0.1$. The results clearly verify the designed fifth-order accuracy of the proposed scheme.

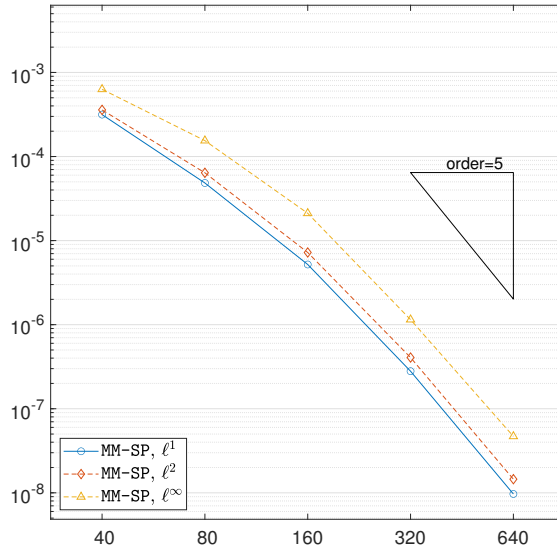


Fig. 1: Example 6.1. The ℓ^1 , ℓ^2 , and ℓ^∞ errors and convergence rate in h obtained by the MM-SP scheme at $t = 0.1$.

Example 6.2 (1D WB test). To demonstrate the WB property of the proposed scheme for the 1D SWEs, two different bottom topographies are considered within the physical domain $[0, 10]$ with outflow boundary conditions. The first topography is a smooth Gaussian profile:

$$b(x) = 5e^{-\frac{2}{5}(x-5)^2}, \quad (67)$$

and the second is a discontinuous square step:

$$b(x) = \begin{cases} 4, & \text{if } x \in [4, 8], \\ 0, & \text{otherwise.} \end{cases} \quad (68)$$

The initial condition is given by $h = 10 - b$ and zero velocity. The gravitational acceleration constant is taken as $g = 1$. The output time is $t = 1$. The monitor function is

$$\omega = \left(1 + 100 \left(\frac{|\nabla_{\xi} h|}{\max |\nabla_{\xi} h|} \right)^2 \right)^{1/2}.$$

Table 1 displays the ℓ^1 and ℓ^{∞} errors in water surface level $h + b$ and velocity v_1 computed with 200 mesh points. The errors are at the level of rounding error in double precision, demonstrating that both the UM-SP and MM-SP schemes are indeed WB. Figure 2 illustrates the water surface level $h + b$, bottom topography b , and the adaptive mesh for the MM-SP scheme. These visualizations show that our moving mesh scheme effectively preserves the lake-at-rest condition and that mesh points are densely concentrated around the sharp transitions in the bottom topography.

Table 1: Example 6.2. Errors in $h + b$ and v_1 obtained by using our schemes with 200 mesh points at $t = 1$, for two different bottom topographies (67) and (68), respectively.

		UM-SP		MM-SP	
		ℓ^1 error	ℓ^{∞} error	ℓ^1 error	ℓ^{∞} error
b in (67)	$h + b$	1.24e-14	4.27e-14	2.13e-14	4.92e-14
	v_1	3.32e-15	1.21e-14	7.04e-15	1.63e-14
b in (68)	$h + b$	1.24e-14	2.79e-14	1.24e-14	3.76e-14
	v_1	3.15e-15	1.23e-14	4.39e-15	1.46e-14

Example 6.3 (1D PP test). This example [13] is used to test the PP property of our schemes for the 1D SWEs with a flat bottom. The physical domain is $[-300, 300]$, and the initial conditions are given by

$$h(x, 0) = \begin{cases} 10, & \text{if } x < -70, \\ 0, & \text{if } -70 \leq x \leq 70, \\ 10, & \text{if } x > 70, \end{cases}$$

with zero velocity. The monitor function is the same as that in Example 6.2.

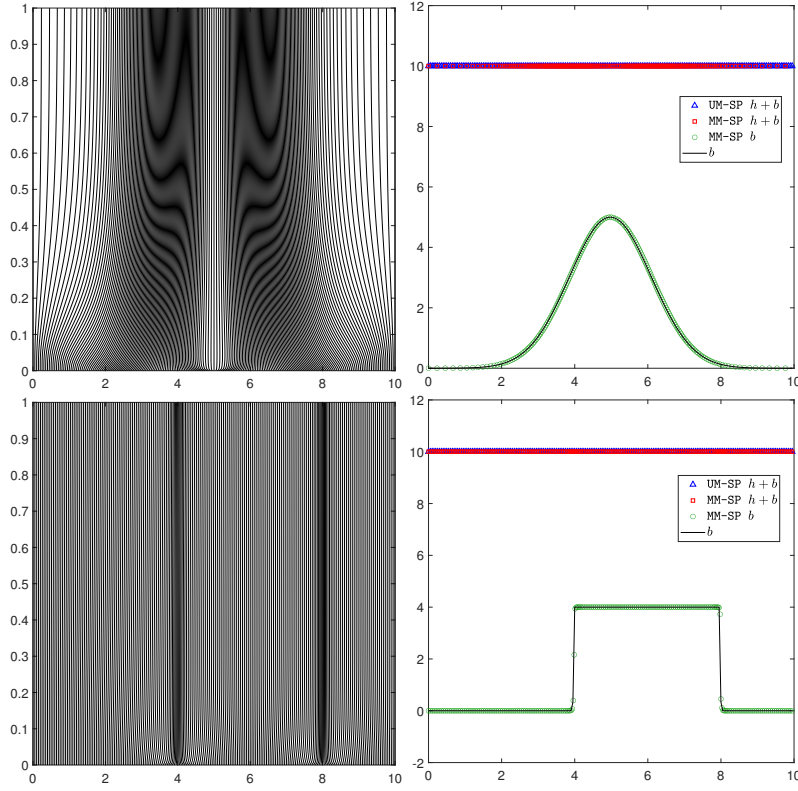


Fig. 2: Example 6.2. Left: the mesh trajectory obtained by the MM-SP scheme, right: the bottom topography b and water surface level $h + b$. Top: with the bottom topography (67), bottom: with the bottom topography (68). The results are obtained with 200 mesh points at $t = 1$.

Figure 3 presents the numerical solution at $t = 1$, showing the comparison between the UM-SP scheme with 200 and 600 cells and the MM-SP scheme with 200 cells. The mesh points for the MM-SP scheme are observed to concentrate around the regions where the water depth h exhibits a large gradient. The numerical experiments confirm that both the UM-SP and MM-SP schemes effectively preserve the non-negativity of h . Notably, without the PP limiter, the code fails at the first time step.

Example 6.4 (Small perturbation test). To demonstrate the capability of the MM-SP scheme in capturing small perturbations of steady-state flow, we consider a bottom topography modeled as a “hump” [16]:

$$b(x) = \begin{cases} 0.25(\cos(10\pi(x - 1.5)) + 1), & \text{if } 1.4 \leq x \leq 1.6, \\ 0, & \text{otherwise.} \end{cases}$$

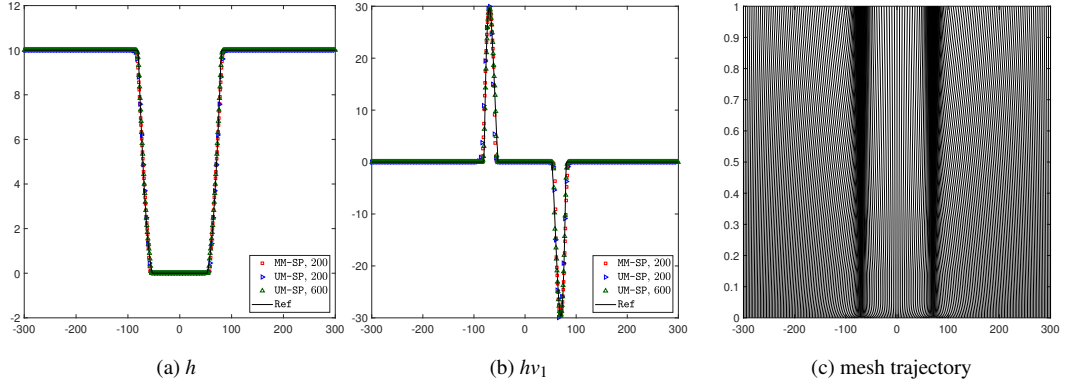


Fig. 3: Example 6.3. The results obtained by using the UM-SP and MM-SP schemes.

The initial conditions for water depth and velocities are defined as

$$h = \begin{cases} 1 - b + \epsilon, & \text{if } 1.1 \leq x \leq 1.2, \\ 1 - b, & \text{otherwise,} \end{cases}, \quad v_1 = v_2 = 0.0,$$

in the physical domain $[0, 2]$ with outflow boundary conditions. The gravitational acceleration constant is set to $g = 9.812$. We test two small perturbations, $\epsilon = 0.2$ and 0.001 , respectively. The monitor function is the same as in Example 6.1, with $\theta = 100$. Figure 4 displays the numerical results at $t = 0.2$ from both the UM-SP and MM-SP schemes using 200 mesh points, along with a reference solution obtained using the UM-SP scheme with 1000 mesh points. The results illustrate that the wave structures are well captured without notable spurious oscillations, and the MM-SP scheme outperforms the UM-SP scheme with an equivalent number of mesh points. Figure 5 shows a comparison of using different reconstructions. It is observed that merely using Step 1 in Section 3.2 (denoted as REC-1) leads to overshoot and undershoot around the sharp wave structures. This observation has motivated our modifications to perform the WENO reconstruction within the computational domain.

To further demonstrate the WB and PP properties of the proposed schemes, we consider the following bottom topography

$$b(x) = \begin{cases} 0.5(\cos(10\pi(x - 1.5)) + 1), & \text{if } 1.4 \leq x \leq 1.6, \\ 0, & \text{otherwise,} \end{cases} \quad (69)$$

which includes a dry region where the water depth $h = 0$ at $x = 1.5$. We introduce a small perturbation with $\epsilon = 0.001$ to evaluate the capability of our schemes in capturing such subtle variations. The monitor function is the same as in Example 6.1, with $\theta = 100$. The numerical results are shown Figure 6, validating that both the UM-SP and MM-SP schemes are able to handle

the small perturbation cases within a dry region. The wave structures captured by the MM-SP scheme with 200 cells closely align with the reference solutions and surpass the performance of the UM-SP scheme with the same cell count. Notably, the numerical simulation fails at $t \approx 0.1$ if the PP limiter is turned off.

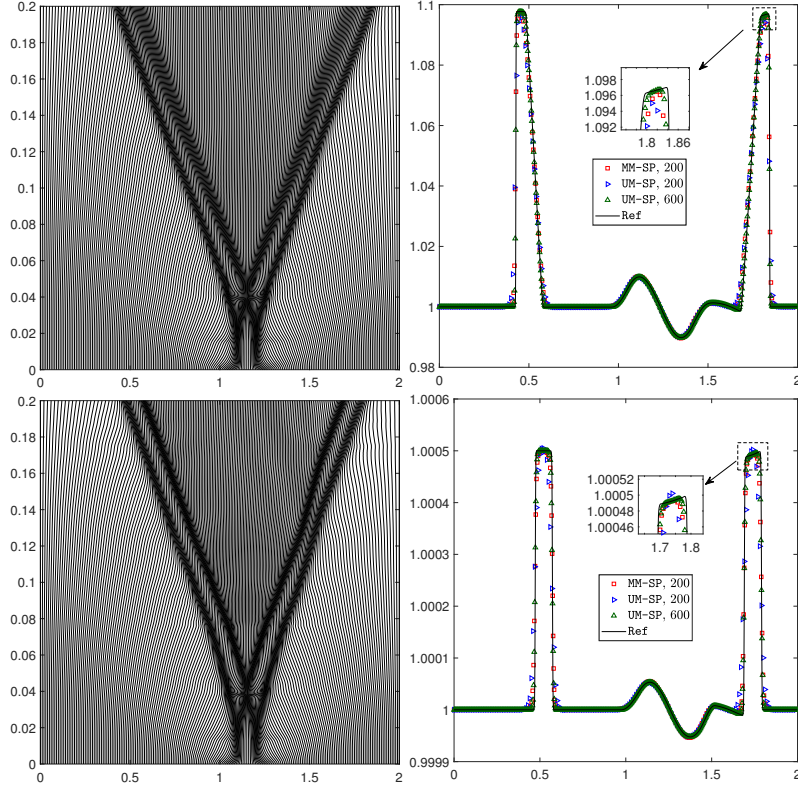


Fig. 4: Example 6.4. The numerical solutions obtained by using the UM-SP and MM-SP schemes at $t = 0.2$. The reference solution is obtained by using the UM-SP scheme with 1000 mesh points. Left: the adaptive mesh obtained by the MM-SP scheme, right: the water surface level $h + b$. Top: the case of $\epsilon = 0.2$, bottom: the case of $\epsilon = 0.001$.

6.2. 2D tests

Example 6.5 (Accuracy test with moving vortex). The 2D vortex problem proposed in [47] is used to verify the accuracy of our schemes with the PP limiter. A steady-state vortex is described by

$$h' = h_{\max} - v_{\max}^2 e^{1-r^2} / (2g),$$

$$(v'_1, v'_2) = v_{\max} e^{0.5(1-r^2)} (-x_2, x_1),$$

where $h_{\max} = 10^{-6} + \frac{v_{\max}^2 e}{2g}$, $v_{\max} = 0.2$, $r = \sqrt{x_1^2 + x_2^2}$, $g = 1$, ensuring the minimum water depth is 10^{-6} so that the PP limiter is necessary for this test. A moving vortex with a constant velocity

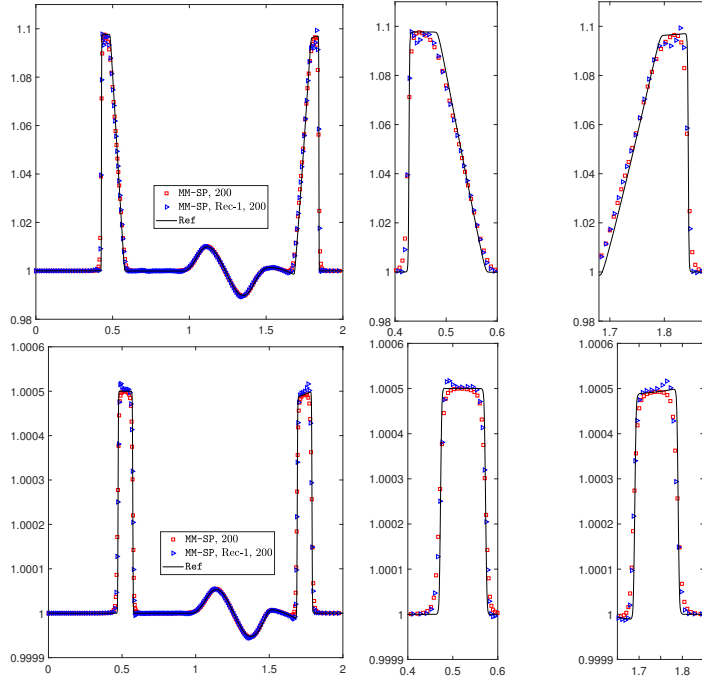


Fig. 5: Example 6.4. The results obtained by using the MM-SP scheme and MM-SP scheme with Rec-1. Left: the water surface level $h + b$, middle: the close view around $x = 0.5$, right: the close view around $x = 1.75$.

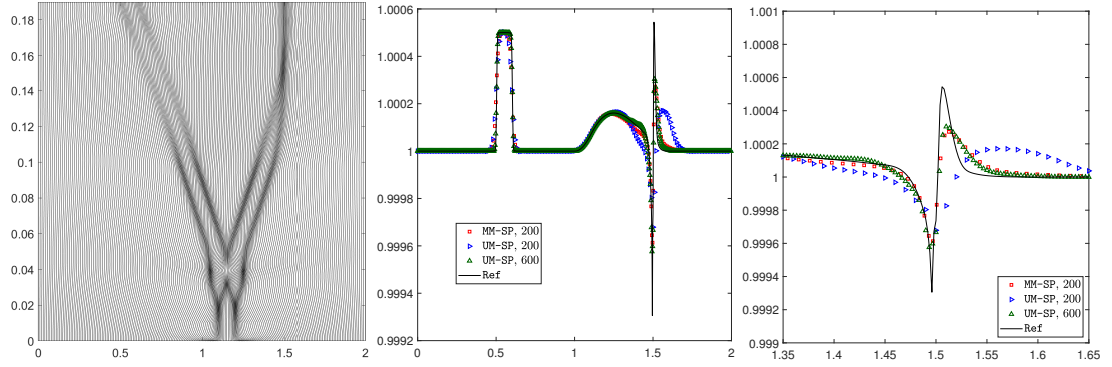


Fig. 6: Example 6.4. The numerical solutions obtained by using the UM-SP and MM-SP schemes at $t = 0.19$. The reference solution is obtained by using the UM-SP scheme with 1000 mesh points. Left: the mesh trajectory obtained by the MM-SP scheme, middle: the water surface level $h + b$, right: the close view around $x \in [1.35, 1.65]$.

of $(1, 1)$ is then obtained by using the Galilean transformation

$$h(x_1, x_2, t) = h'(x_1 - t, x_2 - t, t), \quad (v_1, v_2)(x_1, x_2, t) = (1, 1) + (v'_1, v'_2)(x_1 - t, x_2 - t, t).$$

The simulation runs up to $t = 0.1$ in the physical domain $[-10, 10] \times [-10, 10]$ with periodic boundary conditions. The monitor function used is

$$\omega = \left(1 + 5 \left(\frac{|\nabla_{\xi}(h + b)|}{\max |\nabla_{\xi}(h + b)|} \right)^2 + 5 \left(\frac{|\Delta_{\xi}(h + b)|}{\max |\Delta_{\xi}(h + b)|} \right)^2 \right)^{1/2}.$$

Figure 7 displays the adaptive mesh and ten equally spaced contours of the water surface level $h + b$, computed using the MM-SP scheme with 80×80 cells. The figure also reports the ℓ^1 , ℓ^2 , and ℓ^∞ errors, along with the corresponding convergence behavior of the MM-SP scheme for the water depth h at $t = 0.1$. It can be observed that the mesh points concentrate around the vortex. The MM-SP scheme achieves fifth-order accuracy as expected, and the PP limiter does not compromise this accuracy.

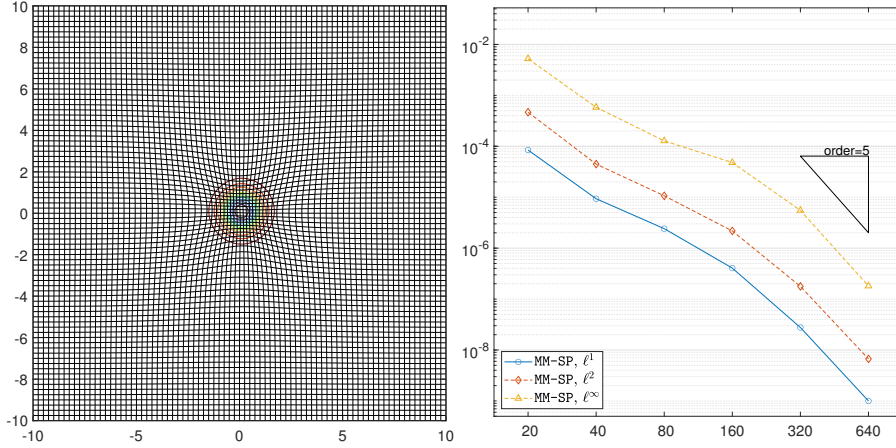


Fig. 7: Example 6.5. The results computed by the MM-SP scheme at $t = 0.1$. Left: the adaptive mesh and 10 equally spaced contours of $h + b$ obtained with 80×80 cells. Right: the ℓ^1 , ℓ^2 , and ℓ^∞ errors and convergence behavior for h .

Example 6.6 (2D PP test). This numerical experiment is performed to verify the PP property of the proposed schemes on fixed and moving meshes [37]. The physical domain is $[-100, 100] \times [-100, 100]$ with outflow boundary conditions. The initial conditions for water depth and velocities are given by

$$h = \begin{cases} 10, & \text{if } \sqrt{(x_1)^2 + (x_2)^2} \leq 60, \\ 0, & \text{otherwise,} \end{cases}$$

$$v_1 = v_2 = 0.$$

The simulation runs until an output time of $t = 0.35$. The gravitational acceleration constant is set to $g = 9.812$. The monitor function is chosen as

$$\omega = \left(1 + \theta \left(\frac{|\nabla_{\xi} \sigma|}{\max |\nabla_{\xi} \sigma|} \right)^2 \right)^{\frac{1}{2}},$$

where $\theta = 50$ and $\sigma = h + b$.

Figure 8 presents the numerical results obtained by using the UM-SP scheme with 100×100 and 300×300 cells, and the MM-SP scheme with 100×100 cells. These results demonstrate that

our schemes, applied to either fixed or moving meshes, work effectively for challenging scenarios where the water depth includes a dry region. Cut lines along $x_2 = 1$ reveal that the numerical results from the MM-SP scheme are superior to those obtained by the UM-SP scheme with the same number of mesh points. Notably, the numerical simulation fails rapidly without the PP limiter, given that the minimum value of water depth h reaches 0.

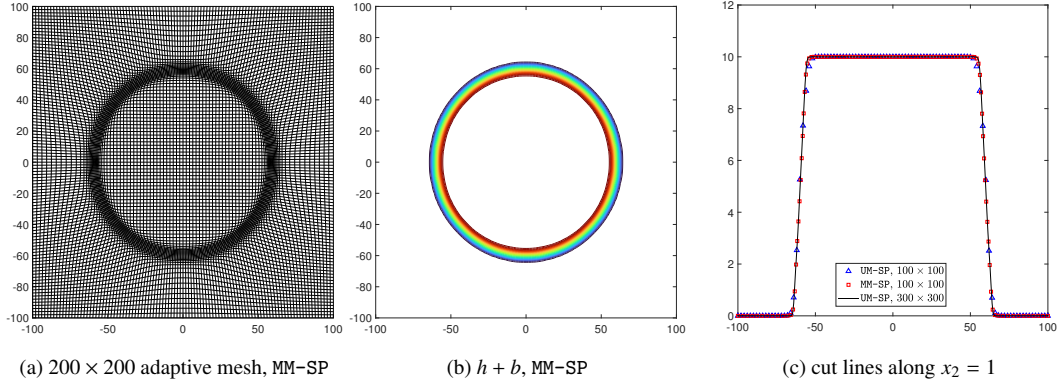


Fig. 8: Example 6.6. The results obtained by using the UM-SP and MM-SP schemes.

Example 6.7 (2D PP test for the bowl). This numerical experiment proposed in [27] is conducted to further validate the PP property of our schemes with non-flat bottom topography on both fixed and moving meshes. The physical domain is $[-4000, 4000] \times [-4000, 4000]$ with outflow boundary conditions. The initial bottom topography is taken as

$$b(x_1, x_2) = \frac{h_0}{a^2}(x_1^2 + x_2^2).$$

The initial velocity are zero, and the initial water depth is given by

$$h = \max \left\{ 0, h_0 \left(\frac{\sqrt{1-A^2}}{1-A} - \frac{x^2 + y^2}{a^2} \frac{1-A^2}{(1-A)^2} \right) \right\},$$

where $A = \frac{a^4 - r_0^4}{a^4 + r_0^4}$, $h_0 = 1$, $r_0 = 2000$, and $a = 2500$. This example has the analytic solution as follows

$$h(x_1, x_2, t) = \max \left\{ 0, h_0 \left(\frac{\sqrt{1-A^2}}{1-A \cos \kappa t} - \frac{x^2 + y^2}{a^2} \frac{1-A^2}{(1-A \cos \kappa t)^2} \right) \right\},$$

$$v_1(x_1, x_2, t) = \frac{\kappa A \sin \kappa t}{2(1-A \cos \kappa t)} x_1, \quad v_2(x_1, x_2, t) = \frac{\kappa A \sin \kappa t}{2(1-A \cos \kappa t)} x_2.$$

The simulations are performed up to two output times $t = 925$ and $t = 2775$. The gravitational acceleration constant is set as $g = 9.812$. The monitor function is the same as in Example 6.6.

Figure 9 presents the numerical results using both the UM-SP and MM-SP schemes, each with 100×100 cells. It includes plots of the adaptive mesh, the water surface level $h + b$, and cross-sectional cut lines along $x_2 = 0$. These results demonstrate that our schemes effectively resolve the shallow water dynamics on non-flat bottom topography and closely match the exact solution. The minimum cell-average value of water depth h reaches 0. Without the PP limiter, the numerical simulation would fail at the first time step.

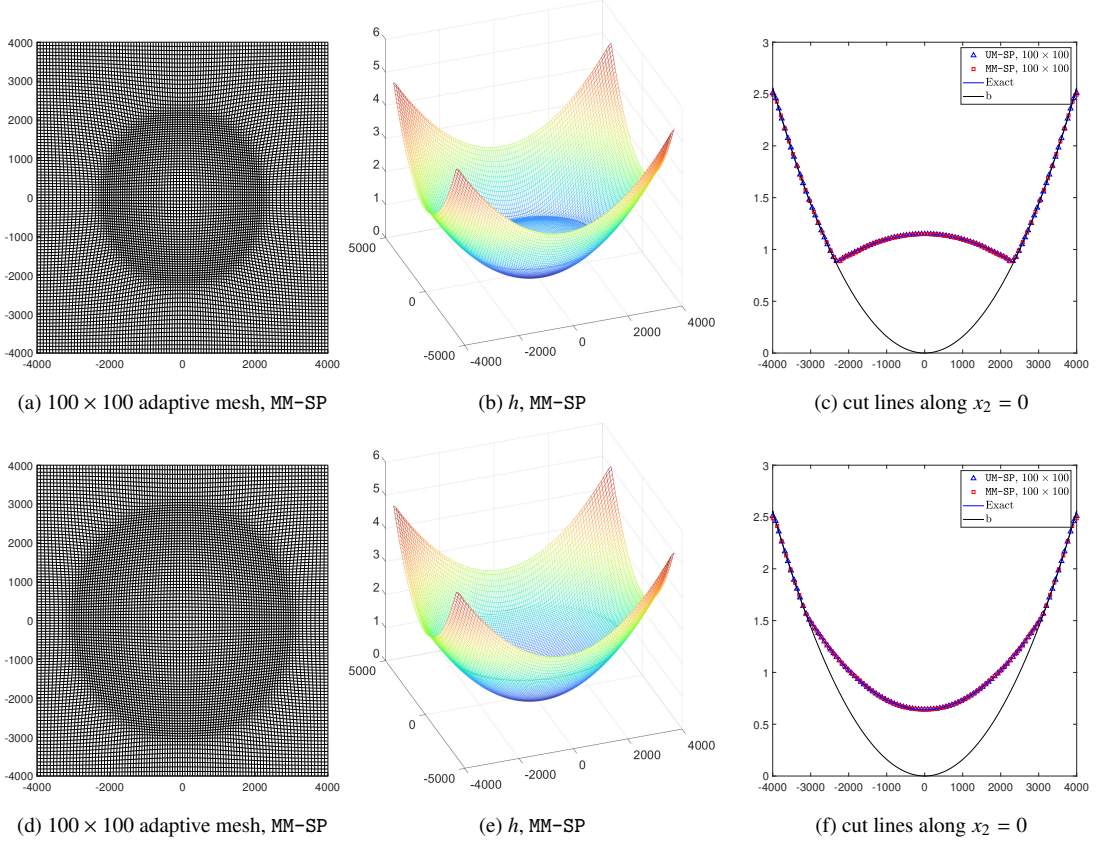


Fig. 9: Example 6.7. The results obtained by using the UM-SP and MM-SP schemes. Top: $t = 925$, bottom: $t = 2775$.

Example 6.8 (2D WB test). This example is designed to test the WB properties of our 2D schemes. The setup is similar to that used in Example 6.2, with two types of bottom topography:

$$b(x_1, x_2) = 0.8 \exp\left(-50\left((x_1 - 0.5)^2 + (x_2 - 0.5)^2\right)\right), \quad (x_1, x_2) \in [0, 1] \times [0, 1], \quad (70)$$

for the smooth topography, and

$$b(x_1, x_2) = \begin{cases} 0.5, & \text{if } (x_1, x_2) \in [0.5, 1.0] \times [0.5, 1.0], \\ 0, & \text{otherwise,} \end{cases} \quad (71)$$

for the discontinuous topography. The initial water depth and velocities are given by

$$h = 1 - b, \quad v_1 = v_2 = 0.$$

The physical domain is $[0, 1] \times [0, 1]$ with outflow boundary conditions, and the gravitational acceleration constant is $g = 1$. To focus the mesh points on the areas with sharp transitions in b , the monitor function is chosen as

$$\omega = \sqrt{1 + \theta \left(\frac{|\nabla_{\xi} \sigma|}{\max |\nabla_{\xi} \sigma|} \right)^2},$$

where σ is the water depth h and $\theta = 100$.

Table 2 lists the ℓ^1 and ℓ^∞ errors in the water surface levels and velocities at $t = 0.1$ computed by using our schemes with 100×100 mesh. These results confirm that the lake-at-rest condition is maintained within the rounding errors of double precision, thus verifying that our schemes are WB on both fixed and adaptive moving meshes. Figure 10 displays the results of the water surface levels $h+b$ and the corresponding bottom topography b , obtained using the MM-SP scheme with a 100×100 mesh. The plots clearly show a concentration of mesh points around areas where b exhibits large gradients.

Table 2: Example 6.8. Errors in $h + b$, v_1 , and v_2 by using our schemes with 100×100 meshes at $t = 0.1$, for the bottom topographies (70) and (71).

		UM-SP		MM-SP	
		ℓ^1 error	ℓ^∞ error	ℓ^1 error	ℓ^∞ error
b in (70)	$h + b$	6.45e-21	1.12e-15	6.85e-21	2.01e-15
	v_1	3.24e-15	2.43e-14	6.84e-16	1.38e-14
	v_2	3.38e-15	2.58e-14	6.92e-16	1.56e-14
b in (71)	$h + b$	5.55e-21	8.33e-16	9.25e-21	1.83e-15
	v_1	3.19e-15	2.51e-14	6.90e-16	1.64e-14
	v_2	3.35e-15	2.60e-14	7.13e-16	1.86e-14

Example 6.9 (The perturbed flow in lake at rest). This example tests the capability of our schemes in capturing small perturbations over a lake at rest within the domain $[0, 2] \times [0, 1]$ with outflow boundary conditions. The bottom topography, described as an “oval hump,” is referenced in [33, 34]. The initial conditions are as follows:

$$h = \begin{cases} 1.01 - b, & \text{if } x_1 \in [0.05, 0.15], \\ 1 - b, & \text{otherwise,} \end{cases}$$

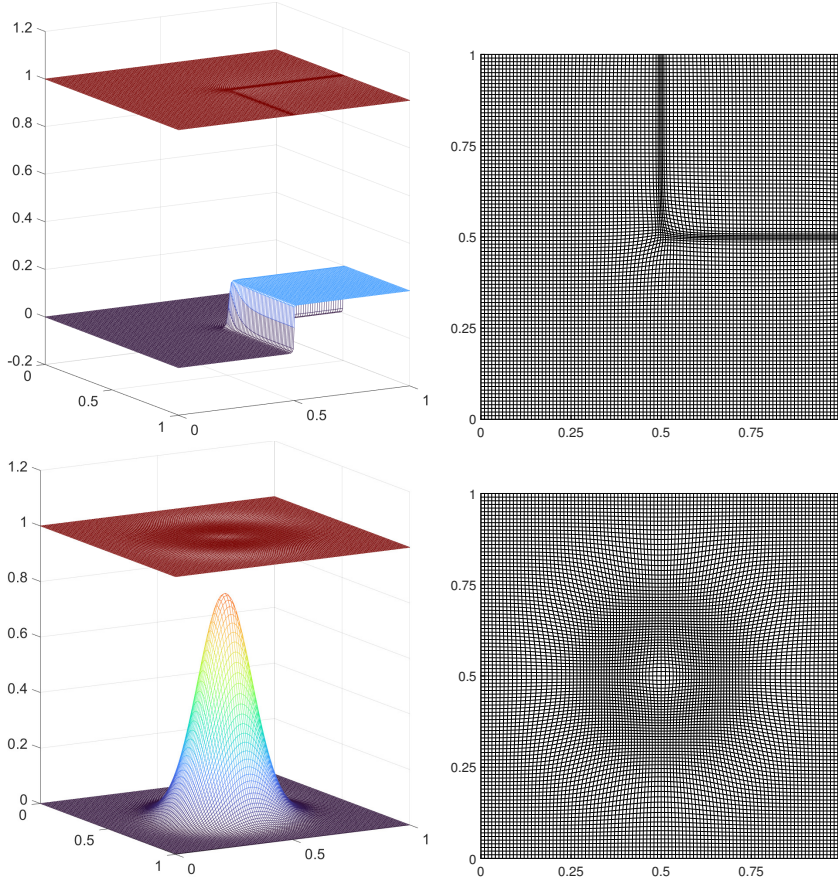


Fig. 10: Example 6.8. The water surface level $h + b$, bottom topography b , and adaptive meshes obtained by using the MM-SP scheme with 100×100 mesh at $t = 0.1$. The figures in the first and second rows correspond to the cases with the bottom topographies (70) and (71), respectively.

$$v_1 = v_2 = 0,$$

$$b = 0.8 \exp(-5(x_1 - 0.9)^2 - 50(x_2 - 0.5)^2).$$

The initial disturbance splits into two waves propagating at speeds of $\pm \sqrt{gh}$, with $g = 9.812$. The monitor function used is identical to that in Example 6.6, but here $\sigma = \log(h + b)$ and $\theta = 250$.

Figure 11 displays the contour plot of the water surface level $h + b$ and the adaptive meshes, with cut lines along $x_2 = 0.5$ at $t = 0.24$ and $t = 0.36$. The results confirm that our schemes accurately capture small features, focusing adaptive mesh points on these areas to enhance resolution. When compared to results obtained by the UM-SP scheme with a finer mesh, the MM-SP scheme achieves comparable outcomes with reduced CPU time, as detailed in Table 3.

Example 6.10 (Water drop problem). This test demonstrates the effectiveness of our moving mesh schemes in capturing complex wave structures by solving the water drop problem over

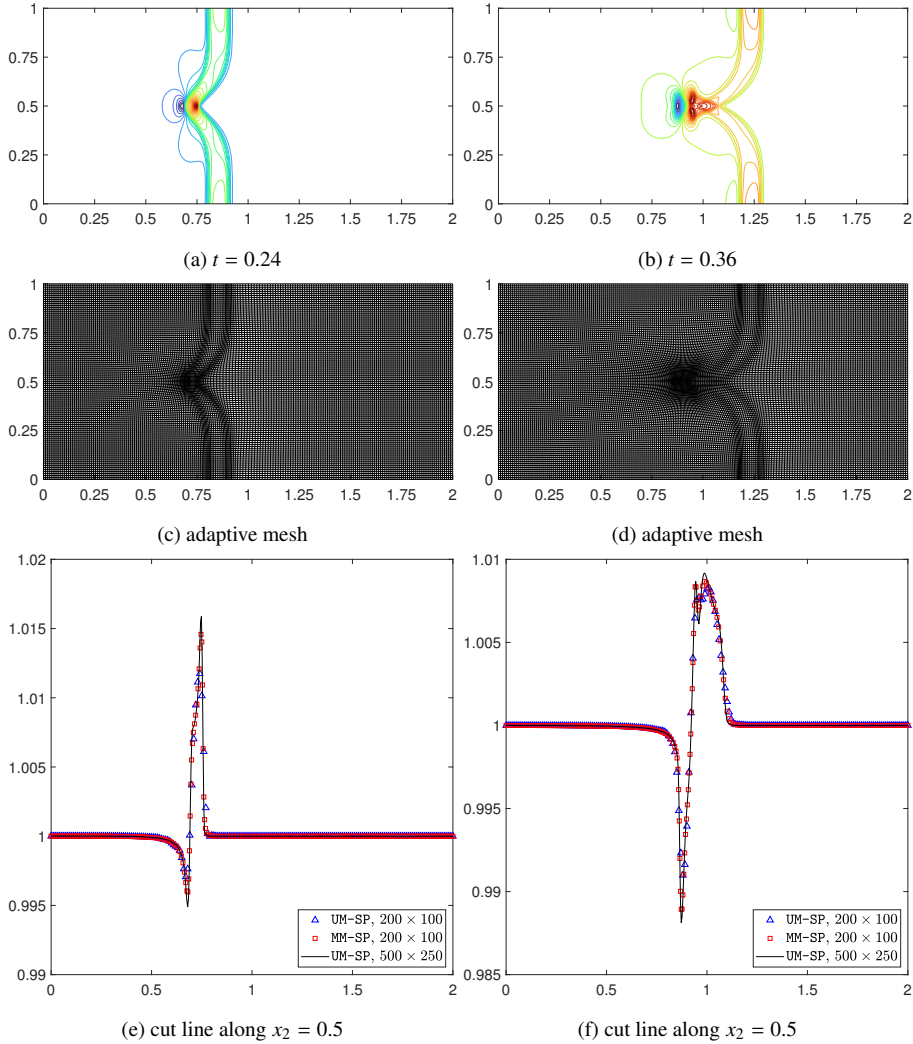


Fig. 11: Example 6.9. The numerical results obtained by the UM-SP and MM-SP scheme. Top: 30 equally spaced contour lines of $h + b$, middle: 200×100 adaptive mesh, bottom: cut line along $x_2 = 0.5$.

a flat bottom. The physical domain is $[0, 2] \times [0, 2]$ with reflective boundary conditions. The Gaussian-shaped peak initial condition is considered:

$$h = 1 + 0.1e^{-1000(x_1-1)^2+(x_2-1)^2},$$

accompanied by zero velocities and a gravitational constant $g = 9.812$. The output times are set as $t = 0.35$ and $t = 0.6$. The monitor function is the same as in Example 6.8, but with $\theta = 50$.

Figure 12 displays the adaptive meshes, water surface level contours, and a cut line across $x_2 = 1$ using our schemes. The adaptive moving mesh scheme accurately captures complex structures and effectively concentrates mesh points in those areas to enhance resolution. Additionally, our schemes maintain excellent symmetry in this numerical experiment. Table 3 illustrates that

the CPU time required for the MM-SP scheme with a 150×150 mesh is approximately 50% less than that required for the UM-SP scheme with a 450×450 mesh.

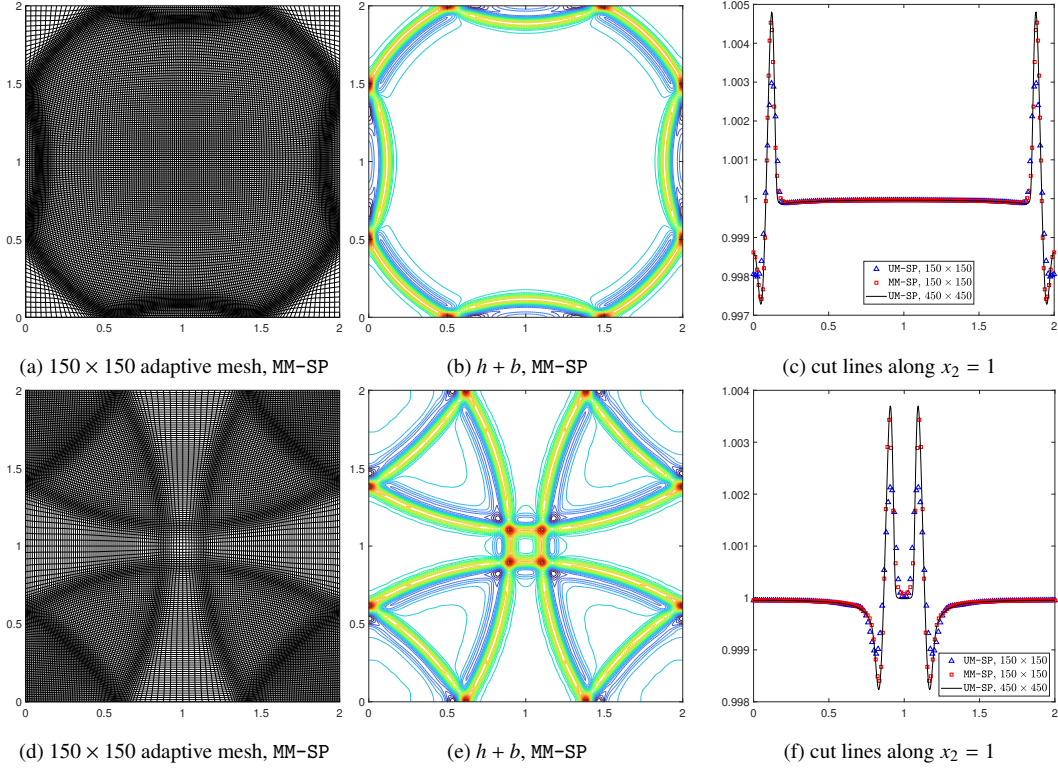


Fig. 12: Example 6.10. The results obtained by using the UM-SP and MM-SP schemes. Top: $t = 0.35$, bottom: $t = 0.6$.

Example 6.11 (Circular dam break on a non-flat river bed). The circular dam break problem [7, 8] for the 2D SWEs is tested here to further illustrate the efficiency of our proposed schemes in the physical domain $[0, 2] \times [0, 2]$ with outflow boundary conditions. The initial conditions for water depth and velocities are

$$h = \begin{cases} 1.1 - b, & \text{if } \sqrt{(x_1 - 1.25)^2 + (x_2 - 1)^2} \leq 0.1, \\ 0.6 - b, & \text{otherwise,} \end{cases}$$

$$v_1 = v_2 = 0.$$

We examine two bottom topographies in our study:

$$b(x_1, x_2) = \begin{cases} \frac{1}{8}(\cos(2\pi(x_1 - 0.5)) + 1)(\cos(2\pi x_2) + 1), & \text{if } \sqrt{(x_1 - 1.5)^2 + (x_2 - 1)^2} \leq 0.5, \\ 0, & \text{otherwise,} \end{cases} \quad (72)$$

and

$$b(x_1, x_2) = \begin{cases} \frac{3}{20}(\cos(2\pi(x_1 - 0.5)) + 1)(\cos(2\pi x_2) + 1), & \text{if } \sqrt{(x_1 - 1.5)^2 + (x_2 - 1)^2} \leq 0.5, \\ 0, & \text{otherwise.} \end{cases} \quad (73)$$

The latter configuration is specifically employed to verify the PP properties of the proposed schemes, because it includes a dry region at $x_1 = 0.5$ and $x_2 = 0$. The gravitational acceleration constant $g = 9.812$. The output times for the configurations (72) and (73) are 0.15 and 0.2, repetitively. The monitor function is the same as that in Example 6.9.

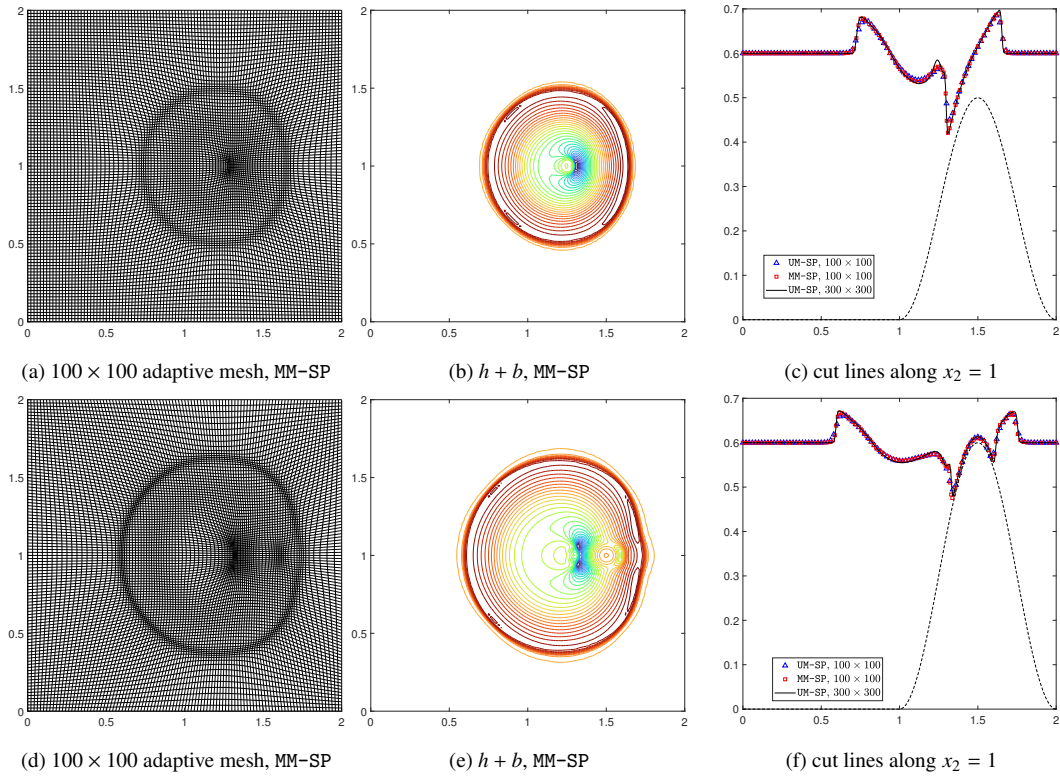


Fig. 13: Example 6.11. The numerical results obtained by using the UM-SP and MM-SP schemes. Top: for bottom topography (72), $t = 0.15$, bottom: for bottom topography (73), $t = 0.2$.

Figure 13 illustrates the 100×100 adaptive mesh, 30 equally spaced contours of the water surface level $h + b$, and a comparison of the cut lines along $x_2 = 1$ obtained by our proposed schemes. The adaptive mesh clearly demonstrates that mesh points concentrate around localized structures. In comparison, the MM-SP scheme produces sharper results near $x_1 \approx 1.26$ than the UM-SP scheme with the same number of mesh points. Without the PP limiter, the numerical simulation results in negative water depths and quickly fails for the bottom topography in (73).

Table 3: CPU times for Examples 6.9–6.11. The measurements are taken on a laptop with an Intel® Core™ i7-8750H CPU @2.20GHz and 24 GB of memory, utilizing 8 OpenMP threads. The code is implemented in C++. Here, “s” denotes seconds, and $N_1 \times N_2$ represents the number of mesh cells.

Examples	UM-PP	UM-PP	MM-PP
Ex. 6.9 ($t = 0 \rightarrow 0.24$)	4.90×10^1 s (200 × 100)	6.89×10^2 s (500 × 250)	3.56×10^2 s (200 × 100)
Ex. 6.9 ($t = 0 \rightarrow 0.36$)	7.30×10^1 s (200 × 100)	1.26×10^3 s (500 × 250)	6.44×10^2 s (200 × 100)
Ex. 6.10 ($t = 0 \rightarrow 0.35$)	3.50×10^1 s (150 × 150)	8.89×10^2 s (450 × 450)	4.48×10^2 s (150 × 150)
Ex. 6.10 ($t = 0 \rightarrow 0.60$)	5.90×10^1 s (150 × 150)	1.52×10^3 s (450 × 450)	6.65×10^2 s (150 × 150)
Ex. 6.11 ($t = 0 \rightarrow 0.15$)	0.60×10^1 s (100 × 100)	1.30×10^2 s (300 × 300)	6.60×10^1 s (100 × 100)
Ex. 6.11 ($t = 0 \rightarrow 0.20$)	6.20×10^1 s (100 × 100)	1.36×10^3 s (300 × 300)	7.44×10^2 s (100 × 100)

The CPU time is detailed in Table 3, highlighting the superior performance of our MM-SP scheme.

7. Conclusion

This paper proposed high-order accurate, well-balanced (WB), and positivity-preserving (PP) finite volume schemes for shallow water equations (SWEs) on adaptive moving structured meshes. The WB property in curvilinear coordinates depends not only on the balance between flux gradients and source terms but also on the dynamics of mesh movement. To manage these complexities, we decomposed the WB property into two main components: flux source balance and mesh movement balance. We achieved flux source balance through the careful decomposition of source terms, the use of numerical fluxes designed via hydrostatic reconstruction, and the suitable discretization of geometric conservation laws (GCLs). These elements combined to ensure the provably WB property in complex curvilinear coordinates. Additionally, we conducted rigorous analyses of the PP property under a sufficient condition enforced by a PP limiter for the proposed moving mesh schemes. Due to the involvement of mesh metrics and movement, these analyses were complicated. The PP property referred to the non-negativity of the water depth and the positivity of the determinant of the coordinate transformation. Mesh adaptation in our method was executed through the iterative solving of Euler–Lagrange equations based on a mesh adaptation functional. The chosen monitor function adeptly concentrated mesh points near significant features, enhancing the efficiency and resolution for discontinuities. Extensive numerical examples were provided, demonstrating the high-order accuracy, high efficiency, and robust WB and PP properties of the schemes.

Appendix A. Proof of condition (46)

This appendix provides the proof of the condition (46). We first prove

$$(\tilde{\mathbf{F}}_{n_1})_{i+\frac{1}{2},j}^{L,\mu} - \sum_{m=1}^2 (\bar{s}_m)_{i,j} (\tilde{\mathbf{r}}_m)_{i+\frac{1}{2},j}^\mu = \langle (\mathbf{n}_1)_{i+\frac{1}{2},j}^\mu, \mathbf{C} \rangle$$

for the numerical fluxes $(\tilde{\mathbf{F}}_{n_1})_{i+\frac{1}{2},j}^\mu$ and $(\tilde{\mathbf{R}}_{m1})_{i+\frac{1}{2},j}$ defined in (37) and (42), respectively. When a steady state is reached, one has

$$\begin{aligned} (\tilde{\mathbf{F}}_{n_1})_{i+\frac{1}{2},j}^{L,\mu} - \sum_{m=1}^2 (\bar{s}_m)_{i,j} (\tilde{\mathbf{r}}_m)_{i+\frac{1}{2},j}^\mu &= \langle (\mathbf{n}_1)_{i+\frac{1}{2},j}^\mu, \tilde{\mathbf{F}}_{i+\frac{1}{2},j}^{L,\mu} \rangle - \sum_{m=1}^2 (\bar{s}_m)_{i,j} \langle (\mathbf{n}_1)_{i+\frac{1}{2},j}^\mu, (\mathbf{r}_m)_{i+\frac{1}{2},j}^{-\mu} \rangle \\ &= \langle (\mathbf{n}_1)_{i+\frac{1}{2},j}^\mu, \tilde{\mathbf{F}}_{i+\frac{1}{2},j}^{L,\mu} - \sum_{m=1}^2 (\bar{s}_m)_{i,j} (\mathbf{r}_m)_{i+\frac{1}{2},j}^{-\mu} \rangle. \end{aligned}$$

Note that

$$\tilde{\mathbf{F}}_{i+\frac{1}{2},j}^{L,\mu} - \sum_{m=1}^2 (\bar{s}_m)_{i,j} (\mathbf{r}_m)_{i+\frac{1}{2},j}^{-\mu} = (L\mathbf{F}_1, L\mathbf{F}_2)^\top$$

with

$$\begin{aligned} L\mathbf{F}_1 &= \begin{pmatrix} 0 \\ \frac{g}{2} \left(h_{i+\frac{1}{2},j}^{-\mu} \right)^2 + g(h+b)_{i,j} b_{i+\frac{1}{2},j}^{-\mu} - \frac{1}{2} g(b^2)_{i+\frac{1}{2},j}^{-\mu} \\ 0 \end{pmatrix}, \\ L\mathbf{F}_2 &= \begin{pmatrix} 0 \\ 0 \\ \frac{g}{2} \left(h_{i+\frac{1}{2},j}^{-\mu} \right)^2 + g(h+b)_{i,j} b_{i+\frac{1}{2},j}^{-\mu} - \frac{1}{2} g(b^2)_{i+\frac{1}{2},j}^{-\mu} \end{pmatrix}. \end{aligned}$$

Using the condition $(h+b)_{i,j} = (h+b)_{i\pm\frac{1}{2},j}^{\mp,\mu} = C$ yields

$$L\mathbf{F}_1 = \begin{pmatrix} 0 \\ \frac{g}{2} C^2 \\ 0 \end{pmatrix}, \quad L\mathbf{F}_2 = \begin{pmatrix} 0 \\ 0 \\ \frac{g}{2} C^2 \end{pmatrix}.$$

Therefore, we obtain

$$(\tilde{\mathbf{F}}_{n_1})_{i+\frac{1}{2},j}^{L,\mu} - \sum_{m=1}^2 (\bar{s}_m)_{i,j} (\tilde{\mathbf{r}}_m)_{i+\frac{1}{2},j}^\mu = \langle (\mathbf{n}_1)_{i+\frac{1}{2},j}^\mu, \mathbf{C} \rangle.$$

The numerical fluxes $(\tilde{\mathbf{F}}_{n_1})_{i-\frac{1}{2},j}^{R,\mu}$ and $(\tilde{\mathcal{R}}_{m1})_{i-\frac{1}{2},j}$ are defined as

$$\begin{aligned} (\tilde{\mathbf{F}}_{n_1})_{i-\frac{1}{2},j}^{R,\mu} &= \langle (\mathbf{n}_1)_{i-\frac{1}{2},j}^\mu, \tilde{\mathbf{F}}_{i-\frac{1}{2},j}^{R,\mu} \rangle - \frac{\beta}{2} (\mathbf{U}_{i-\frac{1}{2},j}^{+,\mu,*} - \mathbf{U}_{i-\frac{1}{2},j}^{-,\mu,*}), \\ (\tilde{\mathcal{R}}_{m1})_{i-\frac{1}{2},j} &= \sum_{\mu=1}^Q \omega_\mu \left[(L_1)_{i-\frac{1}{2},j}^\mu (\tilde{\mathbf{r}}_m)_{n_1}^\mu \right], \\ (\tilde{\mathbf{r}}_m)_{n_1}^\mu &= \langle (\mathbf{n}_1)_{i-\frac{1}{2},j}^\mu, (\mathbf{r}_m)_{i-\frac{1}{2},j}^{+,\mu} \rangle \end{aligned}$$

with

$$(\tilde{\mathbf{F}})_{i-\frac{1}{2},j}^{R,\mu} = \left((\tilde{\mathbf{F}}_1)_{i-\frac{1}{2},j}^{R,\mu}, (\tilde{\mathbf{F}}_2)_{i-\frac{1}{2},j}^{R,\mu} \right)^\top,$$

where

$$\begin{aligned} (\tilde{\mathbf{F}}_1)_{i-\frac{1}{2},j}^{R,\mu} &= \frac{1}{2} \left(\mathbf{F}_1(\mathbf{U}_{i-\frac{1}{2},j}^{-,\mu,*}) + \mathbf{F}_1(\mathbf{U}_{i-\frac{1}{2},j}^{+,\mu,*}) \right) + \begin{pmatrix} 0 \\ \frac{g}{2} (h_{i-\frac{1}{2},j}^{+,\mu})^2 - \frac{g}{2} (h_{i-\frac{1}{2},j}^{-,\mu,*})^2 \\ 0 \end{pmatrix}, \\ (\tilde{\mathbf{F}}_2)_{i-\frac{1}{2},j}^{R,\mu} &= \frac{1}{2} \left(\mathbf{F}_2(\mathbf{U}_{i-\frac{1}{2},j}^{-,\mu,*}) + \mathbf{F}_2(\mathbf{U}_{i-\frac{1}{2},j}^{+,\mu,*}) \right) + \begin{pmatrix} 0 \\ 0 \\ \frac{g}{2} (h_{i-\frac{1}{2},j}^{+,\mu})^2 - \frac{g}{2} (h_{i-\frac{1}{2},j}^{-,\mu,*})^2 \end{pmatrix}. \end{aligned}$$

Similarly, the numerical fluxes $(\tilde{\mathbf{F}}_{n_2})_{i,j+\frac{1}{2}}^{L,\mu}$, $(\tilde{\mathbf{F}}_{n_2})_{i,j-\frac{1}{2}}^{R,\mu}$ and $(\tilde{\mathcal{R}}_{m1})_{i,j\pm\frac{1}{2}}$ are defined as

$$\begin{aligned} (\tilde{\mathbf{F}}_{n_2})_{i,j+\frac{1}{2}}^{L,\mu} &= \langle (\mathbf{n}_2)_{i,j+\frac{1}{2}}^\mu, \tilde{\mathbf{F}}_{i,j+\frac{1}{2}}^{L,\mu} \rangle - \frac{\beta}{2} (\mathbf{U}_{i,j+\frac{1}{2}}^{+,\mu,*} - \mathbf{U}_{i,j+\frac{1}{2}}^{-,\mu,*}), \\ (\tilde{\mathbf{F}}_{n_2})_{i,j-\frac{1}{2}}^{R,\mu} &= \langle (\mathbf{n}_2)_{i,j-\frac{1}{2}}^\mu, \tilde{\mathbf{F}}_{i,j-\frac{1}{2}}^{R,\mu} \rangle - \frac{\beta}{2} (\mathbf{U}_{i,j-\frac{1}{2}}^{+,\mu,*} - \mathbf{U}_{i,j-\frac{1}{2}}^{-,\mu,*}), \\ (\tilde{\mathcal{R}}_{m2})_{i,j\pm\frac{1}{2}} &= \sum_{\mu=1}^Q \omega_\mu \left[(L_2)_{i,j\pm\frac{1}{2}}^\mu (\tilde{\mathbf{r}}_m)_{n_2}^\mu \right], \\ (\tilde{\mathbf{r}}_m)_{n_2}^\mu &= \langle (\mathbf{n}_2)_{i,j\pm\frac{1}{2}}^\mu, (\mathbf{r}_m)_{i,j\pm\frac{1}{2}}^{+,\mu} \rangle \end{aligned}$$

with

$$(\tilde{\mathbf{F}})_{i,j+\frac{1}{2}}^{L,\mu} = \left((\tilde{\mathbf{F}}_1)_{i,j+\frac{1}{2}}^{L,\mu}, (\tilde{\mathbf{F}}_2)_{i,j+\frac{1}{2}}^{L,\mu} \right)^\top, \quad (\tilde{\mathbf{F}})_{i,j-\frac{1}{2}}^{R,\mu} = \left((\tilde{\mathbf{F}}_1)_{i,j-\frac{1}{2}}^{R,\mu}, (\tilde{\mathbf{F}}_2)_{i,j-\frac{1}{2}}^{R,\mu} \right)^\top,$$

where

$$\begin{aligned} (\tilde{\mathbf{F}}_1)_{i,j+\frac{1}{2}}^{L,\mu} &= \frac{1}{2} \left(\mathbf{F}_1(\mathbf{U}_{i,j+\frac{1}{2}}^{-,\mu,*}) + \mathbf{F}_1(\mathbf{U}_{i,j+\frac{1}{2}}^{+,\mu,*}) \right) + \begin{pmatrix} 0 \\ \frac{g}{2} (h_{i,j+\frac{1}{2}}^{-,\mu})^2 - \frac{g}{2} (h_{i,j+\frac{1}{2}}^{+,\mu,*})^2 \\ 0 \end{pmatrix}, \\ (\tilde{\mathbf{F}}_2)_{i,j+\frac{1}{2}}^{L,\mu} &= \frac{1}{2} \left(\mathbf{F}_2(\mathbf{U}_{i,j+\frac{1}{2}}^{-,\mu,*}) + \mathbf{F}_2(\mathbf{U}_{i,j+\frac{1}{2}}^{+,\mu,*}) \right) + \begin{pmatrix} 0 \\ 0 \\ \frac{g}{2} (h_{i,j+\frac{1}{2}}^{-,\mu})^2 - \frac{g}{2} (h_{i,j+\frac{1}{2}}^{+,\mu,*})^2 \end{pmatrix}, \end{aligned}$$

$$\begin{aligned}
(\widetilde{F}_1)_{i,j-\frac{1}{2}}^{R,\mu} &= \frac{1}{2} \left(F_1(U_{i,j-\frac{1}{2}}^{-,\mu,*}) + F_1(U_{i,j-\frac{1}{2}}^{+,\mu,*}) \right) + \begin{pmatrix} 0 \\ \frac{g}{2} \left(h_{i-\frac{1}{2},j}^{+,\mu} \right)^2 - \frac{g}{2} \left(h_{i,j-\frac{1}{2}}^{+,\mu,*} \right)^2 \\ 0 \end{pmatrix}, \\
(\widetilde{F}_2)_{i,j-\frac{1}{2}}^{R,\mu} &= \frac{1}{2} \left(F_1(U_{i,j-\frac{1}{2}}^{-,\mu,*}) + F_1(U_{i,j-\frac{1}{2}}^{+,\mu,*}) \right) + \begin{pmatrix} 0 \\ 0 \\ \frac{g}{2} \left(h_{i-\frac{1}{2},j}^{+,\mu} \right)^2 - \frac{g}{2} \left(h_{i,j-\frac{1}{2}}^{+,\mu,*} \right)^2 \end{pmatrix}.
\end{aligned}$$

Similar arguments show that these numerical fluxes also satisfy the condition (46).

Acknowledgment

The works of Z. Zhang and H.Z. Tang were partially supported by the National Key R&D Program of China (Project Numbers 2020YFA0712000 & 2020YFE0204200), and the National Natural Science Foundation of China (Nos. 12171227, 12326314, & 12288101). The work of K. Wu was partially supported by Shenzhen Science and Technology Program (No. RCJC20221008092757098) and National Natural Science Foundation of China (No. 12171227).

References

- [1] E. AUDUSSE, F. BOUCHUT, M.-O. BRISTEAU, R. KLEIN, AND B. PERTHAME, *A fast and stable well-balanced scheme with hydrostatic reconstruction for shallow water flows*, SIAM J. Sci. Comput., 25 (2004), pp. 2050–2065.
- [2] A. BERMUDEZ AND M. E. VAZQUEZ, *Upwind methods for hyperbolic conservation laws with source terms*, Comput. & Fluids, 23 (1994), pp. 1049–1071.
- [3] R. BORGES, M. CARMONA, B. COSTA, AND W. S. DON, *An improved weighted essentially non-oscillatory scheme for hyperbolic conservation laws*, J. Comput. Phys., 227 (2008), pp. 3191–3211.
- [4] J. U. BRACKBILL, *An adaptive grid with directional control*, J. Comput. Phys., 108 (1993), pp. 38–50.
- [5] J. U. BRACKBILL AND J. S. SALTZMAN, *Adaptive zoning for singular problems in two dimensions*, J. Comput. Phys., 46 (1982), pp. 342–368.
- [6] W. CAO, W. HUANG, AND R. D. RUSSELL, *An r-adaptive finite element method based upon moving mesh PDEs*, J. Comput. Phys., 149 (1999), pp. 221–244.
- [7] M. T. CAPILLA AND A. BALAGUER-BESER, *A new well-balanced non-oscillatory central scheme for the shallow water equations on rectangular meshes*, J. Comput. Appl. Math., 252 (2013), pp. 62–74.
- [8] M. J. CASTRO, E. D. FERNÁNDEZ-NIETO, A. M. FERREIRO, J. A. GARCÍA-RODRÍGUEZ, AND C. PARÉS, *High order extensions of Roe schemes for two-dimensional nonconservative hyperbolic systems*, J. Sci. Comput., 39 (2009), pp. 67–114.
- [9] H. D. CENICEROS AND T. Y. HOU, *An efficient dynamically adaptive mesh for potentially singular solutions*, J. Comput. Phys., 172 (2001), pp. 609–639.
- [10] S. F. DAVIS AND J. E. FLAHERTY, *An adaptive finite element method for initial-boundary value problems for partial differential equations*, SIAM J. Sci. Stat. Comput., 3 (1982), pp. 6–27.

- [11] J. DUAN AND H. Z. TANG, *Entropy stable adaptive moving mesh schemes for 2D and 3D special relativistic hydrodynamics*, J. Comput. Phys., 426 (2021), p. 109949.
- [12] J. DUAN AND H. Z. TANG, *High-order accurate entropy stable adaptive moving mesh finite difference schemes for special relativistic (magneto)hydrodynamics*, J. Comput. Phys., 456 (2022), p. 111038.
- [13] H. HOLDEN AND N. H. RISEBRO, *Front Tracking for Hyperbolic Conservation Laws*, Springer, 2015.
- [14] A. KURGANOV, *Finite-volume schemes for shallow-water equations*, Acta Numer., 27 (2018), pp. 289–351.
- [15] A. KURGANOV AND G. PETROVA, *A Second-Order Well-Balanced Positivity Preserving Central-Upwind Scheme for the Saint-Venant System*, Commun. Math. Sci., 5 (2007), pp. 133–160.
- [16] R. J. LEVEQUE, *Balancing source terms and flux gradients in high-resolution Godunov methods: the quasi-steady wave-propagation algorithm*, J. Comput. Phys., 146 (1998), pp. 346–365.
- [17] G. LI, C. LU, AND J. QIU, *Hybrid well-balanced WENO schemes with different indicators for shallow water equations*, J. Sci. Comput., 51 (2012), pp. 527–559.
- [18] P. LI, W. S. DON, AND Z. GAO, *High order well-balanced finite difference WENO interpolation-based schemes for shallow water equations*, Comput. & Fluids, 201 (2020), p. 104476.
- [19] S. LI, J. DUAN, AND H. Z. TANG, *High-order accurate entropy stable adaptive moving mesh finite difference schemes for (multi-component) compressible Euler equations with the stiffened equation of state*, Comput. Methods Appl. Mech. Engrg., 399 (2022), p. 115311.
- [20] K. MILLER, *Moving finite elements. II*, SIAM J. Numer. Anal., 18 (1981), pp. 1033–1057.
- [21] S. NOELLE, N. PANKRATZ, G. PUPPO, AND J. R. NATVIG, *Well-balanced finite volume schemes of arbitrary order of accuracy for shallow water flows*, J. Comput. Phys., 213 (2006), pp. 474–499.
- [22] S. NOELLE, Y. XING, AND C.-W. SHU, *High-order well-balanced finite volume WENO schemes for shallow water equation with moving water*, J. Comput. Phys., 226 (2007), pp. 29–58.
- [23] W. REN AND X. WANG, *An iterative grid redistribution method for singular problems in multiple dimensions*, J. Comput. Phys., 159 (2000), pp. 246–273.
- [24] J. M. STOCKIE, J. A. MACKENZIE, AND R. D. RUSSELL, *A moving mesh method for one-dimensional hyperbolic conservation laws*, SIAM J. Sci. Comput., 22 (2001), pp. 1791–1813.
- [25] H. Z. TANG, *Solution of the shallow-water equations using an adaptive moving mesh method*, Int. J. Numer. Meth. Fluids, 44 (2004), pp. 789–810.
- [26] H. Z. TANG AND T. TANG, *Adaptive mesh methods for one- and two-dimensional hyperbolic conservation laws*, SIAM J. Numer. Anal., 41 (2003), pp. 487–515.
- [27] S. VATER, N. BEISIEGEL, AND J. BEHRENS, *A limiter-based well-balanced discontinuous Galerkin method for shallow-water flows with wetting and drying: Triangular grids*, Int. J. Numer. Meth. Fluids, 91 (2019), pp. 395–418.
- [28] S. VUKOVIC AND L. SOPTA, *ENO and WENO schemes with the exact conservation property for one-dimensional shallow water equations*, J. Comput. Phys., 179 (2002), pp. 593–621.
- [29] D. WANG AND X. WANG, *A three-dimensional adaptive method based on the iterative grid redistribution*, J. Comput. Phys., 199 (2004), pp. 423–436.
- [30] A. M. WINSLOW, *Numerical solution of the quasilinear Poisson equation in a nonuniform triangle mesh*, J. Comput. Phys., 1 (1967), pp. 149–172.
- [31] K. WU AND C.-W. SHU, *Geometric quasilinearization framework for analysis and design of bound-preserving schemes*, SIAM Rev., 65 (2023), pp. 1031–1073.

- [32] Y. XING, *Exactly well-balanced discontinuous Galerkin methods for the shallow water equations with moving water equilibrium*, J. Comput. Phys., 257 (2014), pp. 536–553.
- [33] Y. XING, *Numerical methods for the nonlinear shallow water equations*, in Handbook of numerical methods for hyperbolic problems, vol. 18 of Handb. Numer. Anal., Elsevier/North-Holland, Amsterdam, 2017, pp. 361–384.
- [34] Y. XING AND C.-W. SHU, *High order finite difference WENO schemes with the exact conservation property for the shallow water equations*, J. Comput. Phys., 208 (2005), pp. 206–227.
- [35] Y. XING AND C.-W. SHU, *High order well-balanced finite volume WENO schemes and discontinuous Galerkin methods for a class of hyperbolic systems with source terms*, J. Comput. Phys., 214 (2006), pp. 567–598.
- [36] Y. XING AND C.-W. SHU, *High-order finite volume WENO schemes for the shallow water equations with dry states*, Adv. Water Resour., 34 (2011), pp. 1026–1038.
- [37] Y. XING AND X. ZHANG, *Positivity-preserving well-balanced discontinuous Galerkin methods for the shallow water equations on unstructured triangular meshes*, J. Sci. Comput., 57 (2013), pp. 19–41.
- [38] Y. XING, X. ZHANG, AND C.-W. SHU, *Positivity-preserving high order well-balanced discontinuous Galerkin methods for the shallow water equations*, Adv. Water Resour., 33 (2010), pp. 1476–1493.
- [39] D. XU, X. DENG, Y. CHEN, Y. DONG, AND G. WANG, *On the freestream preservation of finite volume method in curvilinear coordinates*, Comput. & Fluids, 129 (2016), pp. 20–32.
- [40] J. ZHANG, Y. XIA, AND Y. XU, *Structure-preserving finite volume arbitrary Lagrangian-Eulerian WENO schemes for the shallow water equations*, J. Comput. Phys., 473 (2023), p. 111758.
- [41] M. ZHANG, W. HUANG, AND J. QIU, *A high-order well-balanced positivity-preserving moving mesh DG method for the shallow water equations with non-flat bottom topography*, J. Sci. Comput., 87 (2021), pp. 1–43.
- [42] M. ZHANG, W. HUANG, AND J. QIU, *A well-balanced positivity-preserving quasi-Lagrange moving mesh DG method for the shallow water equations*, Commun. Comput. Phys., 31 (2022), pp. 94–130.
- [43] X. ZHANG, *On positivity-preserving high order discontinuous Galerkin schemes for compressible Navier–Stokes equations*, J. Comput. Phys., 328 (2017), pp. 301–343.
- [44] X. ZHANG AND C.-W. SHU, *On maximum-principle-satisfying high order schemes for scalar conservation laws*, J. Comput. Phys., 229 (2010), pp. 3091–3120.
- [45] X. ZHANG AND C.-W. SHU, *On positivity-preserving high order discontinuous Galerkin schemes for compressible Euler equations on rectangular meshes*, J. Comput. Phys., 229 (2010), pp. 8918–8934.
- [46] X. ZHANG AND C.-W. SHU, *Maximum-principle-satisfying and positivity-preserving high-order schemes for conservation laws: survey and new developments*, Proc. R. Soc. A, 467 (2011), pp. 2752–2776.
- [47] Z. ZHANG, J. DUAN, AND H. Z. TANG, *High-order accurate well-balanced energy stable adaptive moving mesh finite difference schemes for the shallow water equations with non-flat bottom topography*, J. Comput. Phys., 492 (2023), p. 112451.
- [48] Z. ZHANG, H. Z. TANG, AND J. DUAN, *High-order accurate well-balanced energy stable finite difference schemes for multi-layer shallow water equations on fixed and adaptive moving meshes*, arXiv: 2311.08124, (2023).
- [49] Z. ZHAO AND M. ZHANG, *Well-balanced fifth-order finite difference Hermite WENO scheme for the shallow water equations*, J. Comput. Phys., 475 (2023), p. 111860.